Year : 2016

Multi-modal imaging in Ophthalmology: image processing methods for improving intra-ocular tumor treatment via MRI and Fundus image photography

Ciller Carlos

Ciller Carlos, 2016, Multi-modal imaging in Ophthalmology: image processing methods for improving intra-ocular tumor treatment via MRI and Fundus image photography

Originally published at : Thesis, University of Lausanne

Posted at the University of Lausanne Open Archive http://serval.unil.ch
Document URN : urn:nbn:ch:serval-BIB_80886790D53E8

UNIL | Université de Lausanne
Faculté de biologie
et de médecine

Centre d'Imagerie BioMédicale,
Département de radiodiagnostic et radiologie interventionnelle, CHUV

Multi-modal imaging in Ophthalmology: image processing methods for improving intra-ocular tumor treatment via MRI and Fundus image photography

Thèse de doctorat en sciences de la vie (PhD)

présentée à la

Faculté de biologie et de médecine
de l'Université de Lausanne

par

Carlos Ciller

Ingénieur en Telecommunications diplômé
de l'Université Polytechnique de Catalogne (UPC)

Jury:

Prof. Micah Murray, président
Prof. Jean-Philippe Thiran, directeur de thèse
Dr. Meritxell Bach Cuadra, co-directrice de thèse
Dr. Jens H. Kowal, co-directeur de thèse
Prof. Benoit Macq, expert
Prof. Francine Behar-Cohen, experte
Prof. Philippe Cattin, expert

Lausanne, 2016

UNIL | Université de Lausanne
Faculté de biologie
et de médecine

Ecole Doctorale
Doctorat ès sciences de la vie

Imprimatur

Vu le rapport présenté par le jury d'examen, composé de

Président · e	Madame Prof. Stephanie **Clarke**
Directeur · rice de thèse	Monsieur Prof. Jean-Philippe **Thiran**
Co-directeur · rice	Madame Dre Meritxell **Bach Cuadra**
	Monsieur Dr Jens **Koval**
Experts · es	Madame Prof. Francine **Behar-Cohen**
	Monsieur Prof. Benoit **Macq**
	Monsieur Prof. Philippe **Cattin**

le Conseil de Faculté autorise l'impression de la thèse de

Monsieur Carlos Ciller Ruiz

Master in Electrical Engineering, Universidad Politecnica de Cataluna, Espagne

intitulée

Multi-modal imaging in Ophtalmology:
image processing methods for improving intra-ocular tumor treatment via MR1 and Fundus image photography

Lausanne, le 9 décembre 2016

pour le Doyen
de la Faculté de biologie et de médecine

Prof. Stephanie Clarke

Life is and will ever remain an equation incapable of solution,
but it contains certain known factors.
— Nikola Tesla

And we finally come to an end. This is it!
After 4 years of research, working with people across countries, cities and nationalities we are finally coming to a closure. All the time I spent together with my colleagues and collaborators will remain in us, and everything we worked together on will remain for you, and become the *known factors* for the generations to come.
In this ecosystem that is research, I have to thank many individuals. I would like to start by thanking Jean-Philippe Thiran and Meritxell Bach Cuadra, for giving me the opportunity of doing a PhD in Switzerland, and for giving me their support from the beginning. Also, Jens Kowal and specially Raphael Sznitman, who joined my group of advisors and became my mentors later on were important for the success of this journey. Their support and guidance has made me the researcher I am today, and sparked the curiosity I will bring with me in my future research.
I would like to thank the Medical Image Analysis (MIAL) group from the University of Lausanne, the group at CIBM at CHUV and the LTS5 at EPFL for the enjoyable times we spent together. The trips, the conferences and every coffee-break brought me a little closer to this point. Thank you Elena, Elsa, Mario Joao, Roberto, Paul, Athina, Antonia, Simone, Gabriele, Constantin, Xavier, Jessica, Alessandra and Seb for your friendship and laughs all along. Also, at EPFL, Vijay, Marina, Gabriel, Murat, Didrik, Ricardo, Sasan, Christina, Elda, Alia, Gorthi, Virginia, Alessandro and the rest, thank you very much for these moments we shared during these 4 years.
In Bern, the ARTORG Center became my home. At the core of the Ophthalmic Technologies Laboratory I discovered not only really good friends, but also exceptional collaborators and colleagues. I am very thankful to the whole *C* floor, specially to Sandro and Stefanos, for being there whenever MARVIN was putting me down, whenever a paper got rejected and whenever we needed to recompile. Thank you for *Taipo*, for the endless discussions and for

the opportunities we will generate in the future. Also, Tom, Serife, Tatiana, Laurent, Patrick, Michael, Pascal, Toby, Willy and everybody I'm forgetting to mention: Thank you for your time, the most precious asset among all.
The time I spent in the BiomedIA group at Imperial College became one of the best periods during these years. I am very thankful to Daniel Rueckert for giving me the opportunity to learn from him and from his group. It changed the way I face challenges ever since. Also, a special thanks to Jose and Ozan for adopting me from the first weekend in London, both fraternally and research-wise, and to Giacomo and Jorge. You guys made London amusing and sunnier, it would not have been the same without the dogs! Thank you Ira, Sarah, Gregor, Amir, Kostas, Martin, Ricardo, Emma, Lisa, Christian, Ghislain, Jonathan and Matthew for your company and joy. It has been a great period and I am deeply happy for having been part of it and for bringing these friendships with me around Europe and the world.
I would like to thank my *family* in the city of Lausanne. We are not connected by blood, but sometimes it is pretty much the same. Nuria, Alba, Sonia, Guillem, Mireia, Liber and now, Roger. Thank you very much for making me feel like home abroad! Also, the extended family: Miguel, Fernando, Vlado, Cristina, Marco, Aurelia, Cristobal, Marie, Magda, Marc and Simona. Thank you very much for these years!
In the city of Barcelona I left my friends several years ago, however, some connections remain forever. They are responsible for having successfully finished this thesis as well. I would like to thank specially to Ramon, Munsi, Sergio, Manolo, Marta, David, Yuri and Raul. This one is for you, guys.
Laura, I thank you for many things... but today is about this thesis and about your invisible contribution to making it a reality. Thank you. Life moves faster by your side. All your support, smiles and company is imprinted in each of the pages of this thesis and you should be proud, because this is also the result of your work, I am grateful for everything you have given me.
Last but not least, my family. My mom, my sister and my dad and my grandparents, for their blind support and for all the sacrifices they've done. Your care and education has made me the PhD I am today. Thank you, I owe you everything. ...

Abstract

The most common ocular tumors in the eye are retinoblastoma and uveal melanoma, affecting children and adults respectively, and spreading throughout the body if left untreated. To date, detection and treatment of such tumors rely mainly on two imaging modalities: Fundus Image Photography (Fundus) and Ultrasound (US), however, other image modalities such as Magnetic Resonance Imaging (MRI) and Computed Tomography (CT) are key to confirm a possible tumor spread outside the eye cavity. Current procedures to select the best treatment and follow-up are based on manual multimodal measures taken by clinicians. These tasks often require the manual annotation and delineation of eye structures and tumors, a rather tedious and time consuming endeavour, to be performed in multiple medical sequences simultaneously.

This work presents a new set of image processing methods for improving multimodal evaluation of intra-ocular tumors in 3D MRI and 2D Fundus. We first introduce a novel technique for the automatic delineation of ocular structures and tumors in the 3D MRI. To this end, we present an Active Shape Model (ASM) built out of a dataset of healthy patients to demonstrate that the segmentation of ocular structures (*e.g. the lens, the vitreous humor, the cornea and the sclera*) can be performed in an accurate and robust manner. To validate these findings, we introduce a set of experiments to test the model performance on eyes with presence of endophytic retinoblastoma, and discover that the segmentation of healthy eye structures is possible, regardless of the presence of the tumor inside the eyes. Moreover, we propose a specific set of *Eye Patient-specific eye features* that can be extracted from the segmentation of the eye in the 3D MRI, providing rich shape and intensity information of pathological tissue while embedded in the healthy eye structures. This information is later used to train a set of classifiers (Convolutional Neural Networks (CNN), Random Forest, ...) that enable the automatic segmentation of ocular tumors inside the eye.

To conclude, we present a new method for the evaluation of multiple image sequences simultaneously, providing clinicians with a tool to observe the malignancy extent concurrently in Fundus and MRI. To do so, we combine the automatic eye segmentation for MRI presented above with a manual segmentation of ocular tumors in Fundus. Then, we register these two

image modalities with a novel landmark-based registration scheme and fuse the two imaging modalities. We apply this new method to (i) improve the quality of the delineation in the MRI and to (ii) use the *back-projection* scheme to transport rich volumetric measures from the MRI to the Fundus, creating a new 3D shape representation of the 2D Fundus in a method that we named *Topographic Fundus Mapping*. For all experiments and contribution, we validate the results with a dataset of healthy and pathological eye MRIs and a dataset of pathological Fundus images of retinoblastoma.

Keywords: Segmentation, Registre, Model specifique pour pacient, Machine Learning, Convolutional Neural Networks, Statistical Shape Modeling, Pattern recognition, classification, Radiation Oncology, Pediatrics, Magnetic Resonance Imaging, Ophthalmolgy, Fundus Image Photography

Résumé

Le rétinoblastome et le mélanome uvéal sont les types de cancer oculaire les plus communs, touchant les enfants et adultes respectivement, et peuvent se répandre à travers l'organisme s'ils ne sont pas traités. Actuellement, le traitement pour la détection du rétinoblastome se base essentiellement à partir de deux modalites d'imagerie fond d'œil (Fundus) et l'ultrason (US). Cependant, d'autres modalités d'imagerie comme l'Imagerie par Résonance magnétique (IRM) et la Tomodensitométrie (TDM) sont clé pour confirmer la possible expansion du cancer en dehors de la cavité oculaire. Les techniques utilisées pour déterminer la tumeur oculaire, ainsi que le choix du traitement, se basent sur des mesures multimodales réalisées de manière manuelle par des médecins. Cette méthodologie manuelle est appliquée quotidiennement et continuellement pendant toute la durée de la maladie. Ce processus nécessite souvent la délinéation manuelle des structures oculaires et de la tumeur, un mécanisme laborieux et long, effectuée dans des multiples séquences médicales simultanées (par exemple : T1-weighted et T2-weighted IRM ...) qui augmentent la difficulté pour évaluer la maladie.

Le présent travail présente une nouvelle série de techniques permettant d'améliorer l´évaluation multimodale de tumeurs oculaires en IRM et Fundus. Dans un premier temps, nous introduisons une méthode qui assure la délinéation automatique de la structure oculaire et de la tumeur dans un IRM 3D. Pour cela, nous présentons un Active Shape Model (ASM) construite à partir d'un ensemble de données de patients en bonne santé pour prouver que la segmentation automatique de la structure oculaire (par exemple : le cristallin, l´humeur aqueuse, la cornée et la sclère) peut être réalisée de manière précise et robuste. Afin de valider ces résultats, nous introduisons un ensemble d'essais pour tester la performance du modèle par rapport à des yeux de patients affectés pathologiquement par un rétinoblastome, et démontrons que la segmentation de la structure oculaire d'un œil sain est possible, indépendamment de la présence d'une tumeur à l'intérieur des yeux. De plus, nous proposons une caractérisation spécifique du patient-specific eye features qui peuvent être utile pour la segmentation de l'œil dans l'IRM 3D, fournissant des formes riches et une information importante concernant le tissu pathologique noyé dans la structure oculaire de l'œil sain. Cette information est ultérieurement utilisée pour entrainer un ensemble de classificateurs (Convolutional Neural Network

(CNN), Random Forest, ...) qui réalise la segmentation automatique de tumeurs oculaires à l'intérieur de l'œil.
En outre, nous explorons une nouvelle méthode pour évaluer des multitudes de séquences d'images de manière simultanée, fournissant aux médecins un outil pour observer l'extension de la tumeur dans le fond d'œil et l'IRM. Pour cela, nous combinons la segmentation automatique de l'œil de l'IRM selon la description ci-dessus et nous proposons une delineation manuelle de tumeurs oculaires dans le fond d'œil. Ensuite, nous recalons ces deux modalités d'imagerie avec une nouvelle base de points de repère et nous réalisons la fusion des deux modalités. Nous utilisons cette nouvelle méthode pour (i) améliorer la qualité de la délinéation dans l'IRM et pour (ii) utiliser la projection arrière de la tumeur pour transporter de riches mesures volumétriques de l'IRM vers le fond d'œil, en créant une nouvelle forme 3D représentant le fond d'œil 2D dans une méthode que nous appelons Topographic Fundus Mapping. Pour tous les tests et contributions, nous validons les résultats avec une base de données d'IRM et une base de données d'images pathologiques du fond d'œil de rétinoblastome.

Mots-clefs : Delineation d'image, Recalage, Patient-specific model, Machine Learning, Convolutional Neural Networks, Model statistique de surface, Reconnaisance des Patrons, Classification, Oncologie, Pediatrie, Imagerie Resonance Magnetique, Ophthalmolgie, Fond d'œil

Contents

List of Figures

List of Tables

— Introduction

Ever since the beginning of egyptian civilization, one of the oldest known cultures dating back circa 3.000 years before Christ (B.C.), society has venerated the Eye as the most important sensorial organ – a symbol of omniscience and clairvoyance connecting the outside world with the human psyche. Knowledge and interest for the eye has continuously evolved througout thousands of years, shaping religion, culture and research to this day. For the biggest part of this period, religion and cultural beliefs were drivers of common wisdom about vision, yet research on the eye from an evolutive and clinical perspective remained minimal.

It was not until the second half ot 19^{th} century that technical advances led to a breakthrough in eye research. The official introduction of the ophthalmoscope, first reported in 1851 by Hermann von Helmholtz [4], followed by other important creations such as the first prototypes of the Fundus camera, developed in parallel by Henry Noyes and Abner Mulholland Rosebrugh in the 1860s, became the first building blocks of modern medical eye imaging. These inventions were not meant to be used in a clinical setup at that time (low quality images and difficul image acquisitions without damaging the retina), however, thanks to these, J.D. Webster invented the first human Fundus camera in 1886. Iterations followed over the idea with Gerloff [5] until Gullstrand developed the first functional Fundus camera, a conceptual model whose schematics are still used for imaging the interior of the eye [6]. The versatility and cost-effectiveness of the Fundus ophthalmoscope has proven its hegemony as the modality of reference for imaging pathologies in the eye. Simultaneously, eye disease study changed tremendously after the first retinal cameras appeared in 1926 [7]. The advances allowed pathologies like ocular tumors, diabetic retinopathy, age-related macular degeneration and others to be imaged for the first time. The development of such diseases could now be observed via Fundus images as they mostly affect the posterior part of the eye, the so called region of the *retina*, a densely populated multi-layer wall of photosensitive cells that captures

light and transmits its representation of the environment to the brain. Furthermore, it is also a highly vascularized region with a broad set of vessels providing continuous blood flow to the cells located at the back of the eye. In ophthalmology, imaging of these vessels and layers on a continuous basis with Fundus cameras remains the key diagnosis strategy for detecting a large spectrum of ocular diseases.

During the same period that Fundus imaging was living its golden age, other techniques in medical imaging were being developed (*e.g. Ultrasound (US), MRI and Computed Tomography (CT)*). However, in spite of these new approaches becoming crucial for imaging pathologies and deformations all over the body, their applicability in the eye remained far less significant. The most important reasons for this were the aquoeus nature of the vitreous humor tissue, conforming the biggest part of the eye ball, and also the small size of the organ to image, directly affected by the limitations in image resolution and acquisition times. In addition, the cost of these medical devices as compared to the simpler cost-effecive Fundus cameras prevented any strong push towards changing the paradigm of eye screening procedures. Technological advances have shifted this trend in the last 40 years, as methods and techniques to speed-up acquisition time and improve image quality at 3-dimensional level have opened the door to more complete diagnosis and capabilities, far beyond the 2D information of Fundus. For example, 2D/3D US is a technique that has helped evaluating eye diseases such as tumors and orbital conditions for the last 40 years. It came to light in the early 1920-30s as a new method for therapy, however, it was not until 1940 when it was first used as a diagnostic tool, and Karl Theodore Dussik the first *official* user of US in medical diagnosis [8]. Again, systematic evolutions of the technology followed and it became a key imaging modality in structural ophthalmology in the 70´s [9, 10]. Today, US is used to image vitreoretinal interface disease and the anterior and posterior segments, allowing for a quick and easy exploration of the VH cavity and pathologies that may be located therein [11]. For the specific case of intra-ocular tumors, US is used for intra-operative screening and follow-up, being today one of the medical imaging pillars for ocular diseases.

Recently, MRI and CT have also been used for imaging specific conditions in the eye, mostly for screening ocular tumors. CT, developed in the late 60´s and introduced in the 70´s in clinical setups, had been championed for structural image analysis of patient´s organs [12], however, in the last period the use of CT for imaging eye tumors has been less and less recommended [13]. The reasons for this shift are twofold. On the one side, MRI scans can now have an image resolution similar to that offered by CT, while providing a more rich representation of different tissues. Second, medicine is slowly evolving towards non-ionizing techniques for patient screening [14]. In this context, any method that offers similar results to CT without affecting the patient´s health would be considered as an attractive path to follow. On the other side, the negative effects of using CT on infants are far more agressive than in adults and, thus, it is no longer recomended as a modality of reference for such diagnosis [15]. Alternatively, there is MRI, a technology that has evolved intensively in the last 30 years and that has consistently become more accessible for hospitals around the world. Today's techniques have improved traditional caveats such as the acquisition time and resolution, and these specific image

modalities are now becoming the new standard for imaging ocular pathologies. In this thesis we will dedicate some time to explore the principles of MRI and its potential for the future of ocular tumors image analysis.

Finally, the last image modality to join medical imaging of the eye is OCT. The technology, developed in the 90´s, became the first way to image in-vivo nanoscale tissue and has since reshaped diagnosis and pathology detection for the leading causes of blindness worldwide. OCT is a non-invasive light-sourced technique used to image materials by means of low-coherence interferometry [1], reaching an unforeseen resolution of 10^{-10} meters. OCT and all its wide variations has become the modality of reference for very early screening of AMD and Diabetic Retinopathy Edema (DRE) [16–19], as well as a key for the research developed in other fields (*i.e.* skin imaging, material science, ...). In the context of this thesis, OCT will be briefly presented as the next *frontier* towards multi-modal patient specific eye modeling of ocular tumors.

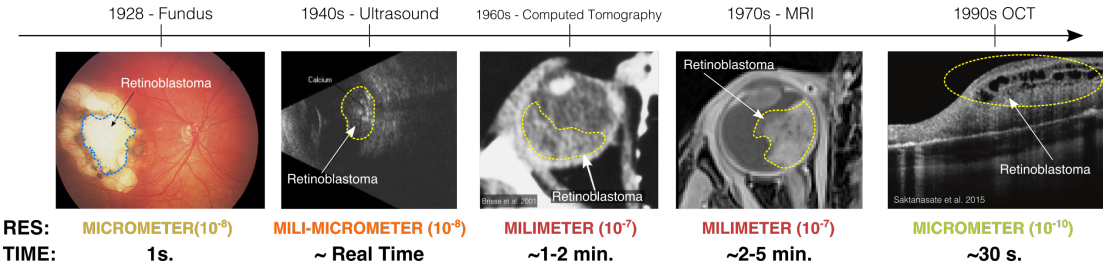

Figure 1 – **Evolution of multimodal imaging in ophthalmology** : From left to right, Fundus image, Ultrasound, Computed Tomography, MRI (3T Scanner) and OCT scan. Past and present of ophthalmology for retinoblastoma. The year on top corresponds to the year that the image modality was first used to image the disease.

In summary, the last century has brought a bountiful set of imaging modalities to science, reshaping clinicians work and decision making process before treatment and during follow-up (see Fig. 1 for more information). The birth of modern imaging in the late 19^{th} century has resulted in several science fields being created. One of these is *medical imaging*, covering not only the research related to the representation of organs and tissue, but also devoted to comprehend and leveraging information accross sources, all towards improving healthcare. In this context, medical imaging analysis tries to answer questions and to find solutions to challenges in subfields such as the registration, the segmentation, the reconstruction, the super-resolution and the statistical modeling of images or volumes. Some of these topics are very present in ophthalmology for the analysis and detection of the most common eye diseases. However, while these techniques are used for specific eye pathology screening independently, there are particular contexts in which both medical imaging at the macro and the micro-scale need to be combined together. The context of ocular tumors is such a case. Unfortunately to date, the topic of ocular tumor medical imaging has not been widely covered in the literature from a technological point of view, both for *retinoblastoma* and *uveal melanoma*, two important types of ocular tumors. In the clinical context, however, radiologist

have provided a multitude of essays with extensive reviews for assessing the evaluation of treatment strategies and the outcome of such experiments, focusing more on the clinical contributions than on the development of new techniques for treating eye malignancies. The reason for this is that ocular tumors are an uncommon disease, and even when they have been imaged consistently via Fundus and 2D US for the last decades, there are still plenty of challenges and unknowns which lend themselves for scientific investigation.

To this end, this thesis will explore how to overcome some of the most important medical imaging challenges in ocular tumors in MRI, such as the time consuming tasks of delineation and detection of pathologies, and how to leverage current medical imaging techniques to propose tools to standardize clinician´s support, improving the treatment strategies for eye cancers. Furthermore, we will propose new methods to extract contextual information from the already available image modalities based on medical image analysis techniques (*e.g.* MRI and Fundus), supporting clinicians with accurate patient-specific information and helping them whenever repetitive and tedious tasks arise.

Thesis Statement

Multi-modal fusion using segmentation of the eye structures and pathologies support clinicians, ophthalmologist and radiologist to better characterize ocular tumors simultaneously, and provides the basis required for precision medicine during ocular follow-up and before treatment.

Thesis Outline and contributions

This work introduces a first attempt to combine and characterize multiple image modalities required for proper treatment and diagnosis of ocular tumors, with a particular emphasys on the automatization, precision and accuracy in the image processing techniques to achieve these goals.

Thesis Outline

- **Chapter 1** introduces the necessary background to understand the contributions of this work. We present a brief description of the eye anatomy and specifically, develop on eye diseases and ocular tumors. We explore current eye imaging techniques and provide an overview of the procedures we utilize for performing the automatic detection and delineation of ocular organs and tumors in multiple image modalities. To conclude we study the methods that allow multi-modal fusion of different images modalities.

- **Chapter 2** focuses on the automatic segmentation of eye structures in 3D MRI, towards improving retinoblastoma diagnosis and treatment. Here, we utilize ASMs for modeling a set of anatomical shapes in healthy eyes, defining a Healthy Model (HM) for the strucures of the lens, the sclera, the cornea and the vitreous humor. This work introduces

the first automatic segmentation framework to automatically delineate the eye in 24 healthy children eyes.

- **Chapter 3** continues the previous work and studies a new method for the automatic delineation of ocular tumors and structures in multi-sequence MRI (*e.g.* T1w VIBE and T2w). We will refer to this model as Pathological Eye Model (PEM). We also introduce a set of *Eye Patient-specific Features* that support the segmentation procedure with rich voxel-level spatial and intensity information, improving the segmentation results consistently.

- **Chapter 4** directs the attention towards the segmentation of retinoblastoma in Fundus and introduces the multi-modal fusion of MRI and Fundus. This section covers a set of techniques for achieving landmark-based registration from 2D Fundus to 3D MRI.

- **Chapter 5** introduces two different applications for the multi-modal fusion of MRI and Fundus. The first one is improving the automatic segmentation of ocular tumors in the 3D MRI via Fundus imaging, the second contribution is the introduction of *Topographic Fundus Mapping*, a new method for the evaluation of Fundus images based on rich 3D MRI information.

- **Chapter 6** draws the general conclusions and provides an overview of the work developed during this PhD, introducing future development lines.

- **Annex A** expands the methods developed in chapter 2, towards achieving automatic segmentation of eye structures in the MRI.

- **Annex B** introduces the *Eye Modeler* software, a medical image analysis tool written in C++ and developed for supporting clinicians during the evaluating of medical images of the in eye (Fundus, MRI, CT, ...).

Thesis Contributions

The contributions of this work can be summarized as :

- A new framework for the fully automatic segmentation of the eye in MRI by means of an ASM for the regions of the sclera, the cornea, the vitreous humor and the lens in T1w VIBE. This ASM will is referred to as HM. We furthermore create a PEM of the eye, built out of 32 pathological patient eyes, and compare the results with the HM presented in [2]. Prior to this, a preliminary work was presented in the *American Research in Vision and Ophthalmology* 2014 conference (ARVO), Orlando, United States [20].

- We introduce the *Eye Patient-specific Features (EPSF)* , derived from our segmentation with the pathological ASM, which helps characterize pathological tissue by providing rich local and global information, even when only small amounts of training data is available. We use these EPSF to build a novel automatic segmentation framework

tailored to ocular tumors. This framework uses of a Markov Random Field (MRF) to represent the presence of healthy and pathological tissue. We encode prior information of the tumors by means of an ASM, as an alternative to the use of typical brain atlas priors or existing ASMs of healthy eyes. This work is currently under review in the *Plos One* journal [21].

- We propose a new method for the automatic fusion of Fundus and MRI by registering common anatomical landmarks present in both image modalities. We furthermore test our approach on two different applications: a) We use the multi-modal 2D to 3D *Fundus Prior* in order to improve the quality of the segmentation in MRI and b) We use the multi-modal fusion in order to transfer rich 3D volumetric information into the 2D Fundus image, in a process that we called *Topographic Fundus Mapping (TFM)*. This work is currently under preparation to be submitted to the *IEEE Transactions on Medical Imaging* journal [22].

- To conclude, we present a new software tool called Eye Modeler that allows the user to load imaging data (MRI, Fundus, ...), annotate information relevant to the patient, build ASMs out of manual delineations of patient eye structures and to do the automatic segmentation of the eye in 3D MRI. The goal of this tool is to support clinicians before treatment and for follow-up of ocular tumors.

1

Background

Human Eye Anatomy

The eye is a key organ in constant evolution and is often regarded as the miracle of nature design [23]. Evolving from single cells to become one of the most valuable animals senses during the *Cambrian evolution* ≈ 540 million years ago, the cells that now form the eyes followed a transition that started with the task of measuring light sensitivity to today´s focus on locomotion and navigation by vision.

Leaving aside the particularities that created this masterpiece, this section will explore the anatomy of the human eye and certain functionalities related to it. We start by providing an overview of the different parts that comprise the eye ball and their relevance in vision, and continue with a specific explanation of common ocular pathologies and ocular tumors, the latter being the central topic of analysis in this thesis.

Anterior Eye Segment

The human eye can be divided into two sections, the posterior and the anterior segment (see Fig. 1.1). The Anterior Segment (AS) comprises the structures in front of the eye: the cornea, the iris, the ciliary body and the crystalline lens. It is itself divided into two additional chambers, called anterior and posterior chamber. The Anterior Chamber (AC) is a cavity filled with the aqueous humor (a transparent fluid inside the eye), and between the iris and the cornea that allows vision. It is also a key mechanical part of the eye, and it is responsible for focusing the light that will later go to the ocular chamber. From a pathology point of view, the AC is linked to pathologies such as glaucoma, that we will introduce briefly later on in

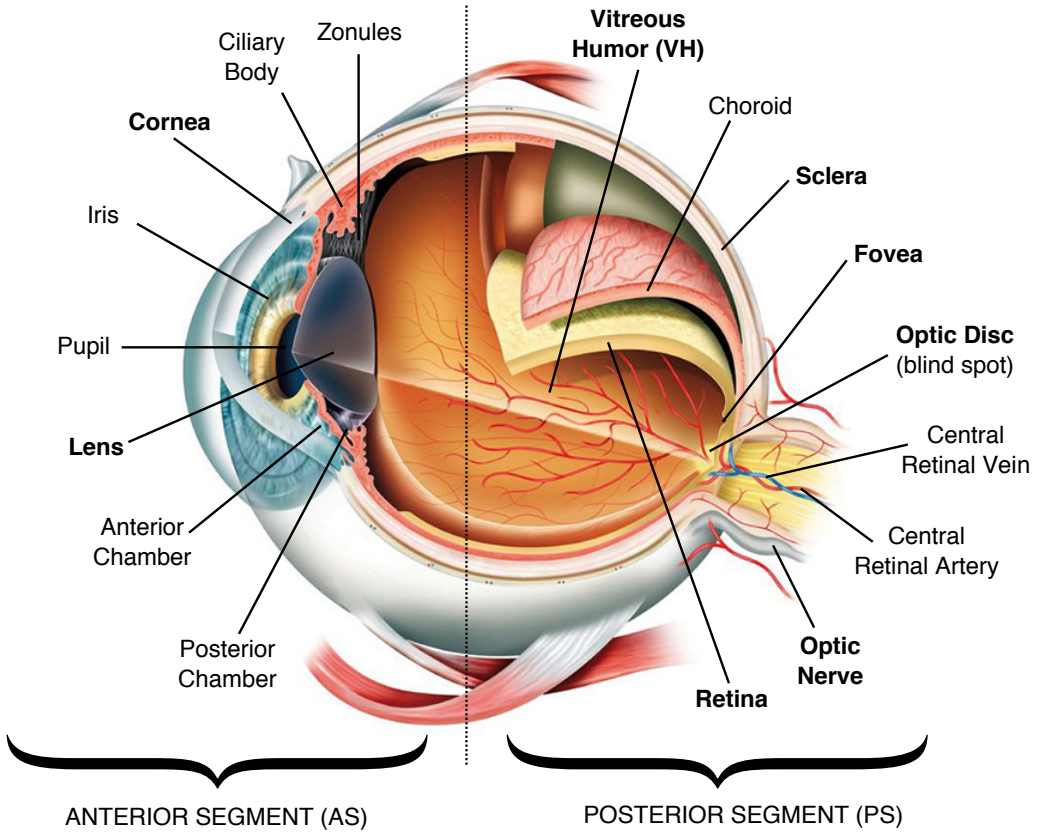

Figure 1.1 – **Eye Diagram** : Representation of the human eye indicating the anterior and posterior segment. The regions of the cornea, the lens, the vitreous humor, the sclera, the fovea, the optic disc, the optic nerve and the retina are highlighted. *Source: Shutterstock - Alexilusmedical ©.*

section 1. For completion, the Posterior Chamber (PC) is located on the surroundings of the iris, just in front of the ligaments (zonules) that control the lens concavity and the VH.

The AS is as well in charge of linking the external world and the visual processing system in the Posterior Segment (PS), whilst protecting the whole outside with a thin transparent layer of collagen fibers known as the cornea. The remaining of the anterior segment in formed by a series of mussels and fibers (ciliary body, ciliary muscles and zonules) that support a central opening systems known as pupil, controlling the amount of light that goes into the retina. A more detailed representation of the eye can be seen in Fig. 1.1.

Posterior Eye Segment

The PS contains the region of the eyes in charge of capturing visual information using photosensitive cells. It starts with the anterior hyaloid membrane and continues with the VH, the retina, the choroid and the optic nerve (see Fig.1.1). Within the PS, we identify a region connecting the AS and the PS called *uvea*, comprising the choroid, the ciliary body and the

iris. This particular region is where *uveal melanoma* takes root [24].

One of the most critical parts of the ocular system is that formed by the different retinal layers, a set of multiple thin coating covers that perform the task of transforming light from the early layers into signals transmitted via the optic nerver towards the brain. An interesting representation of the process transforming the light into impulses cell after cell is that of the Spanish researcher and Nobel Laureate Santiago Ramon y Cajal back in 1911 Fig. 1.2-A).

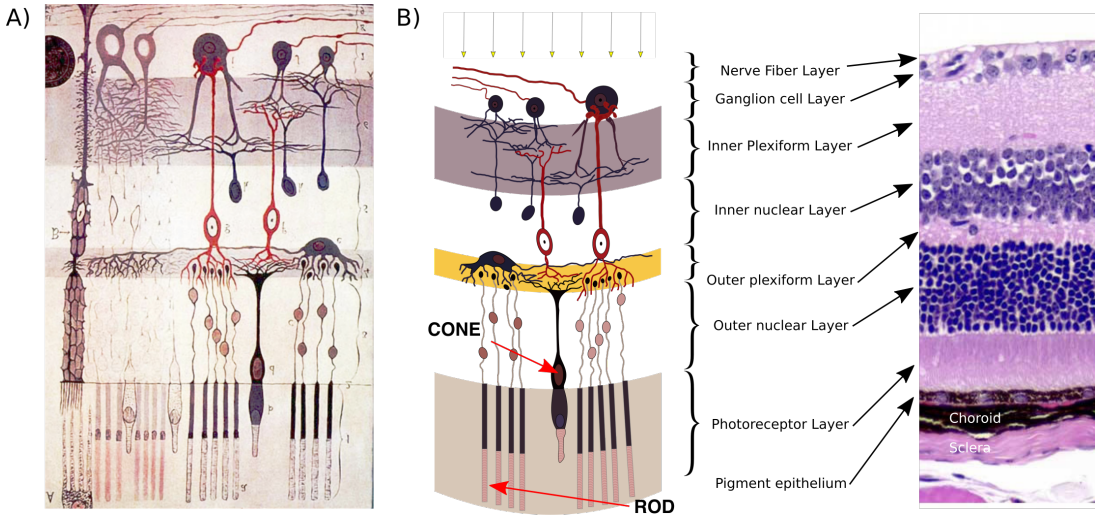

Figure 1.2 – **Diagram of human retina** : A) Retinal layers as drawn by Ramon y Cajal in 1911. Despite not having a high resolution microscope, the Spanish researcher was able to create a very accurate representation of the various eye cells. B) Diagram of the human retina connected to and histopathological section of the retinal wall.

Also relevant to this work is to provide a brief explanation of the shape and growing pattern of the human eye, ranging from an initial size of 16-17 mm diameter when humans are born, and reaching 22-25 mm at the adult age. Moreover, contrary to what it is often assumed, it is not a complete spherical structure, but rather an oval-like organ.

Retina

The retina is the most complex region of the eyes and is composed of different types of cells that work together to guarantee vision. From a functional point of view, the region focuses on generating images by interpretation of signals from the light-excited rod and cone cells (Fig. 1.2-B). The division between these two different types of cells is most significant when considering the distribution of work. The rods, in the order of $\approx 100-150$ millions cells, are very sensitive cells able to capture minor variations in light. Conversely, there are ≈ 7 million cone cells which provide sharp clear vision. Humans, together with many other mammals, have a vascularized retina composed by a mosaic of vessels to nurture the eye regions continuously. Despite the millions of years of evolution, this system has some flaws in

its design. The most significant might be the existence of the OD, a ≈ 2mm radius disc that serves as the connection of the retina to the blood flow and to the brain. This specific location lacks photosentive cells and is considered as the visual *blind spot*. In practice, however, mammals are not affected by this minor error in design, and the 3D stereo reconstruction performed in the brain compensates for the missing blind spot information.

If we explore the eye a bit further in detail, humans have a location in the retina where most of the cone cells are located. This region is know as the *macula* and provides humans with acute vision. Also, the region comprised by the fovea coincides with the point of maximal distance from the cornea tip, passing through the center of the lens and forming a direction vector called Optical Axis (OA). Whenever humans with healthy vision focus their sight on an object, the reflected light from that object is directed specifically to the center of the macular region, to provide the best image definition. An example of the human retina with all the aforementioned parts can be seen in Figure 1.3-A). If we take a step back to analyze the whole retinal surface we will observe that sharp vision comprises a conic field of view of 60°, and is centered in the macula, whilst the rest of the perimetral vision (comprising 200° for healthy eyes) is distributed all over the rest of the eye. From a pathological point of view, the retina is where most of ocular diseases take root (thus, the ever growing relevance in further studying it). Retinal disorders such as AMD, diabetic eye diseases, retinal vein occlusion and retinal detachments [17, 19] are all located in this region.

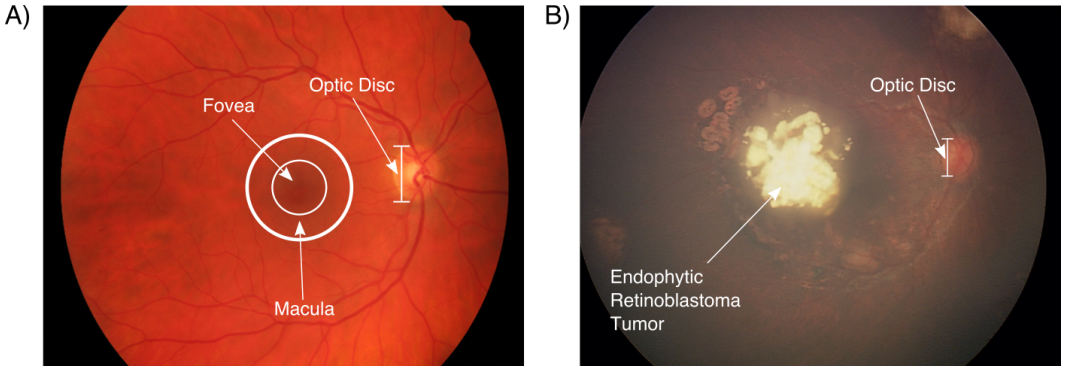

Figure 1.3 – **Fundus image of the retina** : A) Fundus of human retina, indicating the regions of the macula, the fovea and the optic disc. B) Fundus of patient with an endophytic retinoblastoma tumor over the region of the macula.

In addition to all these pathologies with different prognosis and treatment strategies, the retina is the area where ocular tumors are most frequently located (e.g. retinoblastoma in children, Fig. 1.3-B). In the presented work we will base most of our contributions on applications for better treatment of retinoblastoma.

Eye Pathologies

The eyes are home to an extense range of vision diseases, varying in severity and origin. In this section we will provide a short overview about the most common ocular pathologies in the region of the retina (AMD, DR) and glaucoma), and an extensive overview about ocular tumors, more specifically, retinoblastoma.

Age-related Macular Degeneration (AMD) and Diabetic Retinopathy (DR)

The leading cause for vision loss among elderly people over 50 y.o. worldwide is AMD[19]. AMD causes a gradual degeneration of the macular region of the retina (that is, the area surrounding the fovea, see Fig. 1.4). The malignancy typically evolves slowly at the early stage and can often pass unnoticed due to early symptoms being mild. As the disease progresses, there is a gradual loss of central vision, complicating every day activities. Unfortunately, to date there is no cure yet and only certain sources of medication can help slowing down the evolution (*e.g.* anti-Vascular Endotelial Groth Factor (VEGF) drugs, laser coagulation treatment or photodynamic theraphy). Regarding the risk factor and diagnosis, AMD mostly affect elderly people and individuals with a family history related to the disease, however, individuals factors like smoking, hypertension, artherosclerosis or obesity have proven to increase the chances of suffering from AMD and vision loss. Today diagnosis is mostly performed by exploring the interior of the eye with a) Fundus cameras, which work very well in the detection of *dry* macular degeneration by detecting drusen in the retinal wall [25], b) fluorescein angiography, to detect leakage in the vascularization behind the macula, known as *wet* macular degeneration, one of the few conditions that allows for treatment of the disease, and c) OCT, used mostly for the confirmation of the pathology and for patient follow-up [16].

DR, on the contrary, is a disease affecting the vascularization of the retina in diabetic patients. Even if the disease eventually leads to the blindness, there is a good opportunity for it to remain under control, mainly when proper monitoring is conducted. One of the biggest problems linked with DR are the lack of symptoms, thus, it is difficult to detect at the early stage. Current methods for the detection of the disease consist on the early evaluation of diabetic patients via Fundus imaging, toward detecting Non-Proliferative Diabetic Retinopathy (NPDR) of later stages of DR or the use of OCT for accurate pathology detection [26]. Among the different risk factors, we highlight the time the patients has suffered from diabetes disease and the type. Type I and > 60% of Type II diabetes will experience some level of DR in their lifetime. One of the most relevant factors to consider about DR is that early detection allows for proper treatment and a major part of patient's vision can be preserved (*e.g.* Laser photocoagulation, anti-VEGF drugs and more).

An example of the effects caused by both AMD and DR in vision can be observed in Fig. 1.4-B-C).

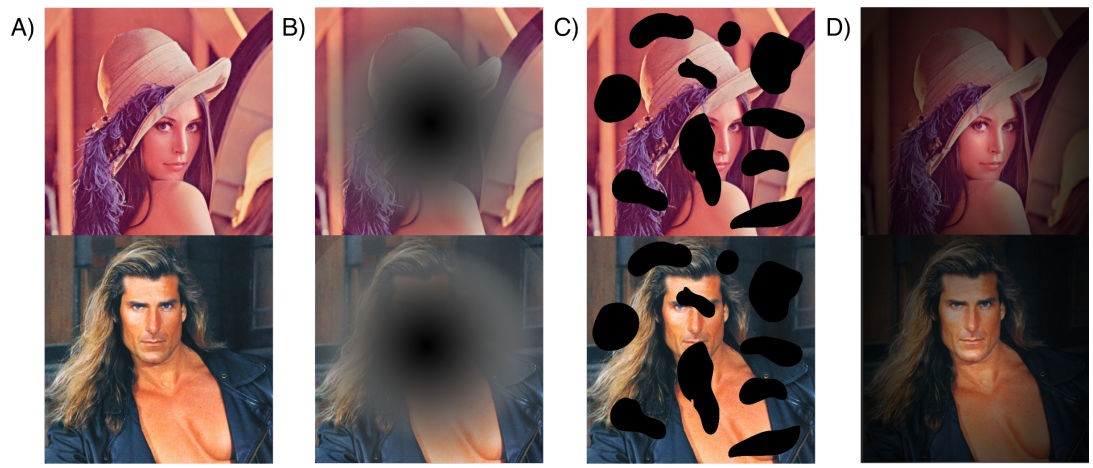

Figure 1.4 – **Effects of AMD, DR and Glaucoma in vision** : These pictures show the results of suffering from B) Age-related Macular Degeneration (AMD) and C) Diabetic Retinopathy (DR) and D) Glaucoma. If left untreated all three diseases will outcome in the complete loss of vision for the patient. In image A) we can observe the original image without vision distortion. Ocular tumors, such as retinoblastoma, show similar image distortion conditions depending on the location of the tumor and its size.

Glaucoma

Glaucoma is a disease that covers a broad set of pathologies affecting vision and the optic nerve. The malignancy normally starts with a reduction of the peripheral vision and continues to affect the central vision (macular region) gradually [27]. Different symptoms consider eye pain, eye redness or blurred vision, eventually leading to blindness if the patient is not properly treated. Among the most common risk factors for the development of the disease we find high eye pressure, obesity and a family history of glaucoma [28]. Current methods for detecting glaucoma consider the evaluation via Fundus and OCT, as well a visual test examination for assessing vision quality. Indicators such as the cup-to-disc ratio also provide information about possible damage due to the appearance of glaucoma [29]. One of the good news about glaucoma disease is that laser treatments, medication and surgery can reduce the eye pressure and possibly stop or reduce the evolution of the disease [30]. An example of the effects in vision caused by Glaucoma can be seen in Fig. 1.4-D).

Ocular tumors

Retinoblastoma and uveal melanoma are the most common eye tumors in children and adults [31, 32]. In this thesis we will focus our efforts in the former, though most of the techniques and contributions we introduced could be easily translated to adults.

Retinoblastoma

Retinoblastoma is a fast spreading eye tumor appearing in children before the age of five [31, 33, 34]. It normally takes root in the posterior part of the eye and develops towards the rest of the body if left untreated [35]. The disease is related to high levels of mortality and morbidity, thus, early detection is key for maximizing chances of proper treatment and recovery. Clinicians often suggest that children´s life is out of danger if the tumor is kept inside the ocular cavity [36], however, the risk is strongly linked to the size of the tumor and its growing pattern. Research studies have shown that retinoblastoma is very often an hereditary mutation ($\approx 50\%$), affecting the RB-1 gene, localized in the chromosome 13q14 [37]. For the rest of cases, the origin of the pathology is a congenital mutation in the same gene. One of the particularities of these malignancies is that they can affect one or both eyes (uni- or bilateral retinoblastoma), depending on inheritance factors, however, the occurence of bilateral retinoblastoma is mostly found in patients which have a family history related to the disease. Furthermore, this last subset is prone to be affected by a more aggresive form of cancers, such as pineoblastomas and Primitive Neuroectodermal Tumors (PNET), these rare cancer forms may appear in combination with retinoblastoma in a more aggressive mutation known as trilateral retinoblastoma. Unfortunately, the chances of survival for patients with such form of retinoblastoma are low [38].

Among the risk factors for metastasis and tumor recurrence, the spread of the tumor via the eye wall (sclera and choroid) into the orbit, or the spread of the disease via the optic nerve are unwanted and often jeopardize patient survival [39]. Furthermore, patients have shown a higher risk for developing secondary malignancies throughout time after treatment with ionizing techniques [40], therefore, it is highly recommended to keep their exposure to radiation levels low and, even during treatment, to keep a good balance between risks and benefits of imaging and treatment strategies. A clear example is that of CT, a modality whose controversial use in imaging these patients has shown a theoretical increased risk of developing secondary malignancies due to the RB-1 gene mutation.

Despite retinoblastoma being a very aggressive tumor, low indicidence rates in the order of 1 every 17.000 newborns [37] suggest that no mandatory revision is required in babies, unless there exist a given family record. Early eye examinations are though recommended, including red reflex and Hirschberg tests for detecting early retinoblastomas in children, and the appearance of leukocoria [41] is a strong indicator of the presence of abnormal tissue inside the eye.

Concerning the tumor growth pattern and behavior, retinoblastoma is divided in four different groups: endophytics, exophytic, a combination of endo- and exophytic and, in very rare cases, diffuse infiltrating tumors [39]. The difference between endophytics and exophytics relies on whether they develop in the intraretinal layers or outside them. For the rare cases of diffuse infiltrating tumors, the situation appears when multiple patches appear in different locations in the retina, without a clear cancer mass.

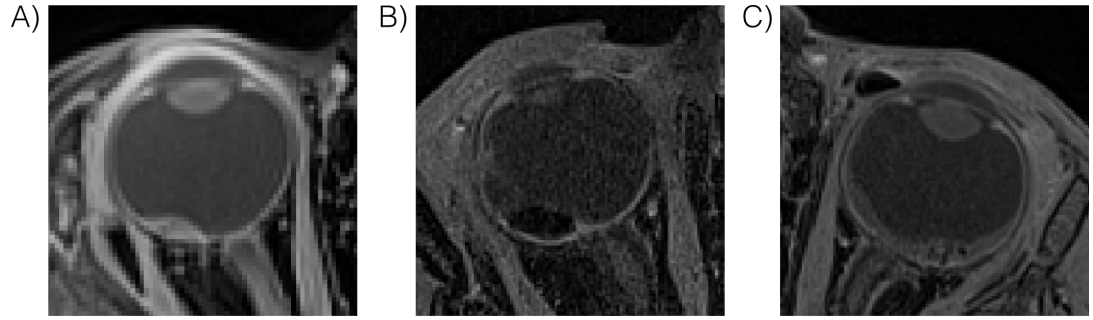

Figure 1.5 – **Different types of retinoblastoma tumor in MRI** : These pictures show an A) Endophytic retinoblastoma, B) Exophytic retinoblastoma and a C) patient with a combination of Endo- and Exophytic retinoblastoma (as well as a partial retinal detachment due to the tumor presence).

Table 1.1 – **International classification of retinoblastoma (ICRB)** : Reference guide based on specific tumor features to support treatment strategies and follow up [3].

Group	**Quick Reference**	**Specific Features**
A	Small Tumor	Rb <3 mm in size
B	Large Tumor	Rb >3 mm in size or
		macular Rb location [$< 3mm$ to foveola]
		juxtapapillary Rb location [$\leq 1.5mm$ to disc]
		clear subretinal fluid $\leq 3mm$ from margin
C	Focal Seeds	Rb with
		subretinal seeds $\leq 3mm$ from Rb
		vitreous seeds $\leq 3mm$ from Rb
		both subretinal and vitreous seeds $\leq 3mm$ from Rb
D	Diffuse seeds	Rb with
		subretinal seeds $> 3mm$ from Rb
		vitreous seeds $> 3mm$ from Rb
		both subretinal and vitreous seeds $> 3mm$ from Rb
E	Extensive Rb	Extensive Rb occupying > 50% globe or
		Neovascular glaucoma
		Opaque media from hemorrhage in anterior chamber, vitreous or subretinal space
		Invasion of postlaminar optic nerve, choroid ($> 2mm$), sclera, orbit, anterior chamber

Treatment of ocular tumors

Treatment of ocular tumors depends mostly on the size, location and spread of the disease. For the case of adult uveal melanoma patients, treatment follows a pathway where repetitive invasive surgeries and ionizing radiation are regularly considered [42]. For the specific case of retinoblastoma, the aim is always to explore less invasive treatment strategies and to proceed to more radical techniques only if the pathology does not evolve positively. In this context, and in order to support the process of decision making, an International Classification of retinoblastoma (ICBR) table was introduced to standardize the evaluation process based on features of interest [3] (Table 1.1).

From a treatment point of view, retinoblastoma is a disease that brings together clinicians from several backgrounds (i.e ophthalmologists, radiologists, pathologists, ...) who play a

role in the treatment, recovery and psychological support of the infant [3]. Keeping this in perspective, the number of variables to consider are extensive and vary for every patient. In here we provide a short description of the most common treatment strategies, including a few words on the indicated tumor characterization for every case:

- **Thermotheraphy** suggests using infrared light to increase the tumor temperature to 45 < °C. Very small tumors < $3mm$ may respond favorably to this treatment [31].
- **Laser photocoagulation** uses an argon or diode laser or a xenon arc in order to coagulate all the blood supply to the tumor [43]. A few side effects include retinal detachments, and retinal vascular occlusion.
- **Cryotherapy** induces the fast freezing of the tumor, with the side effect of damaging the vascularization of the area of action. This therapy is generally very effective and arises few complications[43], it is also recommended for tumors < $3mm$.
- **Brachytheraphy** consist on placing a radioactive implant (plaque) attached to the outside of the eye ball. The idea behind is to irradiate the tumoral region with a dose calculated based on the apex of the tumor inside the eye via transcleral diffusion. This treatment is limited to tumors < $6mm$ [31].
- **Intra-venous and intra-arterial Chemotherapy** consists on infusing the patient with a chemical agent directed to the tumor, towards shrinking its size. Chemotherapy alone does not provide final results but allows for other less invasive therapies to be applied [31, 36].
- **Chemothermotheraphy** is similar to the above, but including heat sessions (thermotherapy) directly inside the eye during a period of a month [44].
- **Proton Therapy** considers using a proton beam for treating patients with retinoblastoma. Protons cause smaller damage than x-rays, used in External Beam Radiotherapy (EBRT), while providing the same level of radiation to the tumoral mass.
- **EBRT** is recommended for patients where chemotherapy did not provide positive results. It consists on the irradiation of the tumoral area with a radiation beam. The chances of causing second recurrent malignancies or cancers increases with this treatment are relatively high [33].
- **Enucleation** is the last resort for critical stage retinoblastoma patients, consisting in the removal of the eye. This solution is reserved for an advanced disease that does not respond to chemotherapy or any other of the previous techniques [43].

In Fig. 1.6 we show an overview of the different treatments strategies applied to the different tumor sizes. As stated before, treatment of retinoblastoma evolves towards more aggressive strategies if the cancer does not evolve positively.

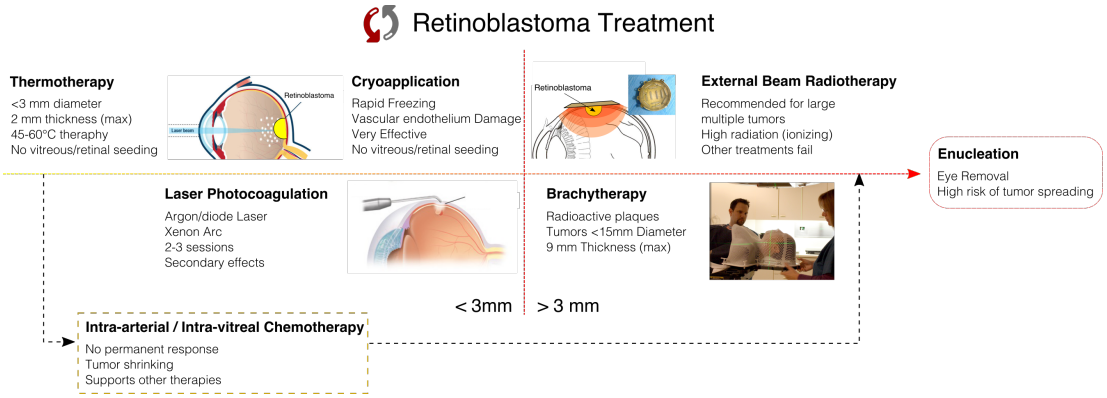

Figure 1.6 – **Treatments strategies for retinoblastomas** : Treatment strategies vary depending on the size of the tumor, the location and the evolution. For most cases, Intra-arterial / Intra-vitreal chemotherapy is applied in combination with other treatments to reduce the tumor size. In this diagram, treatment evolves from left (mild treatment) to right (aggressive treatment).

Uveal Melanoma

Uveal melanoma is a disease that takes root in the region of the *uvea*, composed by the choroid, the iris and the ciliary body [45]. The cancer arises from the pigment cells giving color to the eyes (melanocytes) and affects mostly to the adult population over the age of 60 years. Uveal melanoma is divided into different types of tumors depending on the location, being the AS a more favorable location than the PS for patient recovery. That is, tumors located in the region of the choroid will experience a least favorable prognosis as compared to the tumors located in the region of the iris, being the latter far less common and difficult to detect [46].

As regards to the symptoms, uveal melanomas are not easy to discover in early stages of the disease. They generally become visible once the tumor enlarges, either because they distort the pupil (in the case of iris melanoma), due to a blurred vision (ciliary body) or due to a loss in the visual acuity, as a result of potential retinal detachments. To date, US evaluation by clinicians remains the main method to detect the malignancy, however, other techniques such as CT and more recently OCT are being used to take decisions for future treatment and for therapy planning. The risk factors for developing this type of tumors considers the iris color, the skin color and the ability to tan, specially for the caucasic Europeans, as the most relevant factors for the appearance of the disease [47].

In a similar fashion to retinoblastoma, there are a complete set of options to consider in order to prevent the tumor spread. For small tumors, treatments such as thermotheraphy, photocoagulation and photodynamic therapy are utilized, however, there is a certain controversy as to their effectivity [48]. For bigger tumors though, the roadmap is a bit more agressive than that of retinoblastoma patients, with a transition between brachytherapy and external beam radiotherapy happening in the last 10 years. Latest advances in medical imaging have pushed the use of MRI and CT for 3D tumor planning before therapy, with medical image analysis

tools such as *OCTOPUS* [49] being used prior to the procedure with favorable results. Today, patients with uveal melanoma with a size over $> 3mm$ will most likely undergo treatment considering EBRT, opting for enucleation if the treatment is not effective.

In this thesis we will focus our efforts in the evaluation of techniques and methods for improving intra-ocular tumor treatment planning of retinoblastoma. Most of the techniques applied here could be easily ported to *uveal melanoma* treatment in adults. For more information about uveal melanoma, we would like to direct the reader to the following literature [24, 32, 46].

Eye Imaging Techniques

Diagnosis of eye pathologies is generally established on the basis of Fundus and 2D US evaluation. Ophthalmologist have traditionally scanned the eye with rather simple, yet useful, imaging techniques that allow for the screening of the most critical parts of the eye. For more advanced pathology screening where structural information is required, the use of CT and MRI, for adults and children respectively, is common. Nevertheless, due to the high cost related to these image modalities and because of their use, mostly related to imaging ocular tumors, it is rarely necessary. In the last years, though, OCT is gaining more and more traction in the field of retinal pathology observation. This situation is mainly driven by the constant improvements in the hardware technology behind OCT and also thanks to medical image processing techniques, that allow the visualization of micrometric tissue structures.

For the remainder of this section we will focus on the image modalities that are used in this thesis, 3D MRI and Fundus, and briefly explain why CT is no longer recommended, following a short introduction about the future of retinoblastoma imaging in OCT. The motivations that supported the focus on these two techniques are related both to (i) the protocol for imaging eye cancers, which is more and more reducing CT for treatment planning of ocular tumors in children (retinoblastoma [14]) and (ii) the data acquisition constraints. For the pathologies studied here, US-acquired images were not providing the 3-dimensional information required to evaluate the tumor extent, thus MRI was necessary to look for calcifications and possible invasions of the optic nerve.

Fundus Imaging

Fundus imaging is the process whereby 2D representation of the 3D retinal tissues are acquired. To capture those, doctors may project light inside the eye by means of a Fundus camera and acquire the reflecting light from the eye again through the eye lens [50]. There are a few different imaging techniques that fall within the cathegory of *Fundus imaging*: simple Fundus Photography (also called red-free photography), Color Fundus Photography, Stereo Fundus photography, Hyperspectral Eye photography, Scanning Laser ophtahlmoscopy (SLO) and adaptative optics SLO and Angiography [50].

Overall, Fundus cameras aim to obtain a 2D representation of the retina, including the regions of the macula and the OD. In a nutshell, they could be represented as a small form of microscope (with an attached flashing camera at the tip) to acquire images of the eye. A more detailed representation of the working principles of Fundus can be found in Fig. 1.7. Clinicians typically place the patient sitting in front of the device, with the chin resting on a holder and the forehead laying against the device (see Fig. 1.8-A). The ophthalmologist then proceeds to focus the image and take a picture. For the specific case of children with retinoblastoma, the process often includes a mobile Fundus camera, specific for pediatric imaging, as seen in Fig. 1.8-B).

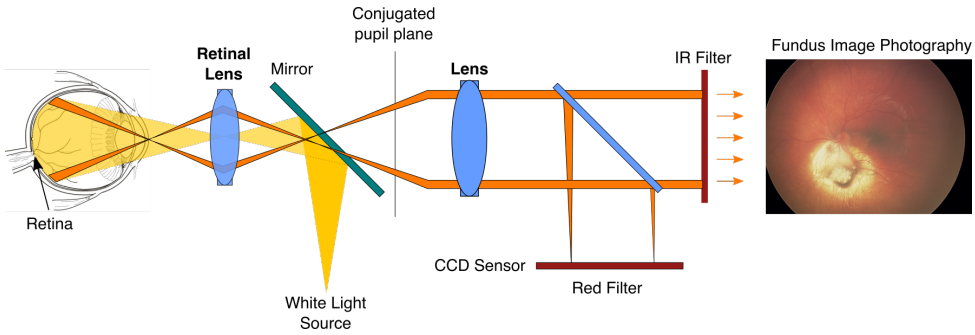

Figure 1.7 – **Fundus camera working principle** : Fundus camera working principles. The light source enters the eye from a lateral source illuminating the retina. A combination of lens allows the acquisition of the projected light into into the photosensitive sensor.

In the context of pathology screening, it is mainly used for observing AMD, DR and glaucoma. In Fig. 1.9-B-C) we can observe a few examples of the pathologies and the Fundus representations connected to these specific disease.

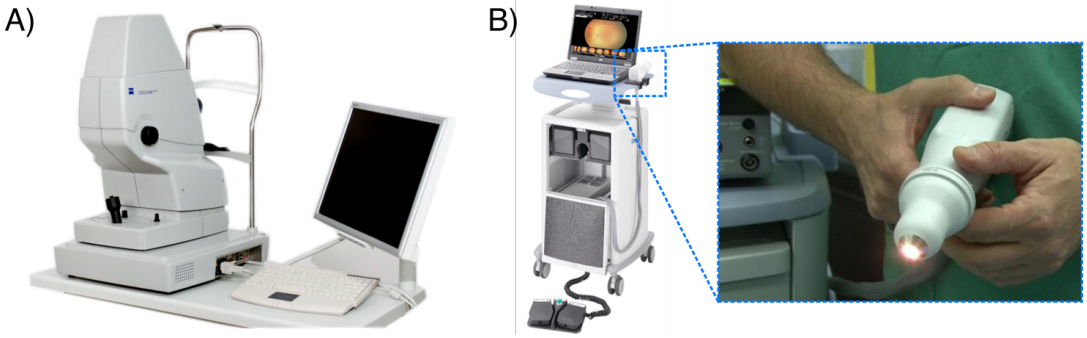

Figure 1.8 – **Fundus cameras** : A) Zeiss Fundus camera with a holder for resting the chin. B) Detail of Pediatric RetCam. A set of interchangeable lens simplifies the procedure by the clinician.

Also, Fundus is the key image modality for the follow-up and early diagnosis of retinoblastoma and uveal melanoma [33, 36, 37]. Despite Fundus having the key role in the evaluation of the disease, still it requires confirmation from completementary image modalities, such as US or MRI. In Fig. 1.9-D) we can see a few example of Fundus images of retinoblastoma patients.

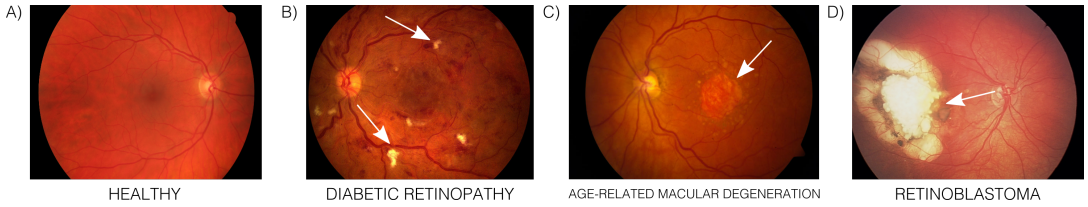

Figure 1.9 – **Fundus images for different pathologies :** A) shows the picture of a healthy Fundus, B) Diabetic Retinopathy, C) Age-related Macular degeneration and D) retinoblastoma.

Limitations

While these 150 years of development have served very well to improve the current Fundus imaging systems, there are still a few challenges to overcome. Among the major limitations that affect Fundus we may highlight the difficulties to generate a proper 3D representation of the retinal wall [50], the difficulties related to observing pathological volumetric information in the retina (e.g. tumors) and the skills that ophthalmologists require in order to acquire proper Fundus images. Also, minor limitations such as the light that the delicate retina can whitstand and the optics system building the eye (lens, acqueous regions ...) are important factors affecting the image quality.

At a more pathology specific perspective, there exist a number of limitations affecting Fundus imaging of ocular tumors. As observed in Fig. 1.9, big tumors in the interior of the eye do not allow for a proper imaging of the disease and alternative image modalities are required. It is also true that whenever such tumors are encountered, the disease is certainly in an advanced stage and very few possible treatment solutions are available (*EBRT or enucleation*).

To conclude, limitations such as the cost of the device may be crucial in countries where access to medicine is not trivial. In this direction, latest technological advances such as the one proposed in the last years to integrate Fundus acquisitions on mobile phones are opening the door to a widespread use of Fundus screening by populations at risk.

Ocular Magnetic Resonance Imaging (MRI)

MRI acquisition has been one of the pillars of medical imaging ever since its conception in 1973 and is today an indispensable tool for structural medical diagnosis. It is also a non-invasive non-ionizing image modality which provides similar structural information as compared to CT, and goes beyond this image modality by providing tissue information, key to the evalution of certain pathologies. The working principle of MRI is a complex combinations of equations and tecnology developed throughout more than 40 years [51].

It all starts with a directional magnetic field which traverses the body and alters the hydrogen proton nuclei (an element present in water and body fat in high amounts). The spinning hydrogen proton has a north and south pole distribution, which is affected by the action of

the magnetic field, inducing those protons to *align* with the magnetic vector created inside the scanner. Now, an additional electromagnetic Radio-Frequency (RaFr) pulse (known as the Lamor frequency) is added to the magnetic field, creating a deflection that will cause certain hydrogen proton nuclei to resonate and to modify their spin with a strength proportional to the magnetic field inside the scanner. This procedure is known as *excitation*. The strength of the magnetic field can be altered locally at different possitions inside the scanner, thus making it possible to acquire different slices of the body therein.

Once this process is finished, the RaFr wave stops and the protons return to their original resting states, emitting a RaFr pulse during the process. This signal is recorded by the MRI scanner thanks to a set of receiver coils and has the shape of an exponential curve. Sampling of this curve generates the so called *k-space*, which is nothing more than the representation of the image in the frequential domain (Fourier). 2D/3D scans are the cumulative mapping of specific locations in the volume with a varying time and excitation, representing this specific tissue in space. The reconstruction of image is achieved by computing the inverse fourier transform of the k-space volume, as seen in Fig. 1.10

MRI for imaging Ocular Tumors

MRI has a very diverse set of acquisition techniques which show different non-complementary sources of information about the patient. Among the most relevant sequences for imaging ocular cancers we find 2D/3D T1w-VIBE and 2D/3D T2w [37], all of them used in order to explore the appearance of trilateral retinoblastoma, invasion of the optic nerve and extraocular tumor spread [39]. For the specific application presented in this thesis we focused on the evaluation of 3D T1w-VIBE and 3D T2w.

T1w-VIBE is a Gradient Echo (GE) sequence whose data acquisition process can be easily reformatted to provide volumes in different orientations, a procedure often called multiplanar reconstruction [52]. Furthermore, it is often the case that patients are injected with an intravenous contrast enhancer, a solution to improve the imaging conditions of the tumoral region during the scan. These image modalities are typically part of the routine imaging protocol in our institution and facilitate the visualization of the tumor extent. An important insight about the T1w VIBE used in this work is that they are fat-suppressed sequences, that is, tissue with a higher concentration of fat will be represented with darker areas, as can be seen in Fig. 1.14.

Moreover, we also use 3D T2w. This specific sequence is commonly represented in conjunction with T1w sequences and provides rich information about the presence of fluid in the imaged area, resulting in higher signal intensities. Alternatively, low presence of fluid in the region of interest is depicted with a lower intensity. Radiologist evaluate all these image modalities concurrently for better diagnosis and treatment plan of the disease, independently of the pathology.

As regards to the tumor presentation in the MRI, retinoblastoma often appears occupying an

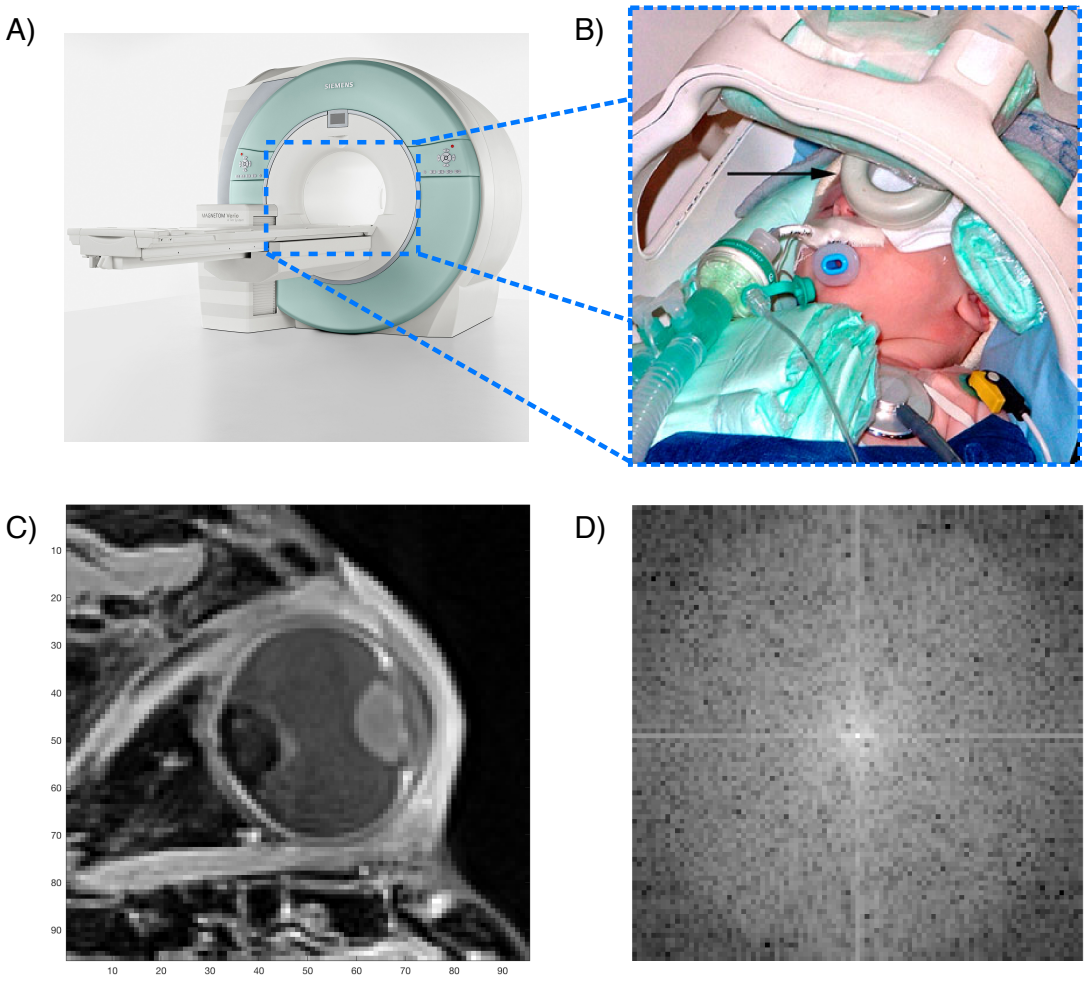

Figure 1.10 – **Details of MRI setup for children and example of MRI image in K-space** : A-B) General setup for patients with retinoblastoma. C-D) Detail of a T1w VIBE MRI and it k-space representation.

area with a moderate high signal intensity on T1w and low signal intensity on T2w compared to the VH [39]. Calcifications are also critical during MRI evaluations, and are spotted as areas where intensity on T2w is low. All these sources of information are critical for decision making and confirmation of tumor extent. A few examples of retinoblastoma tumors inside the eye cavity can be seen in Fig. 1.14.

Limitations

Albeit the benefits of using MRI as a complementary source of information, or even an alternative to other image modalities such as CT, there are a few limitations to overcome. One of the most important is the economic factors that are connected to these devices, making it a really expensive tool for developing countries [53].

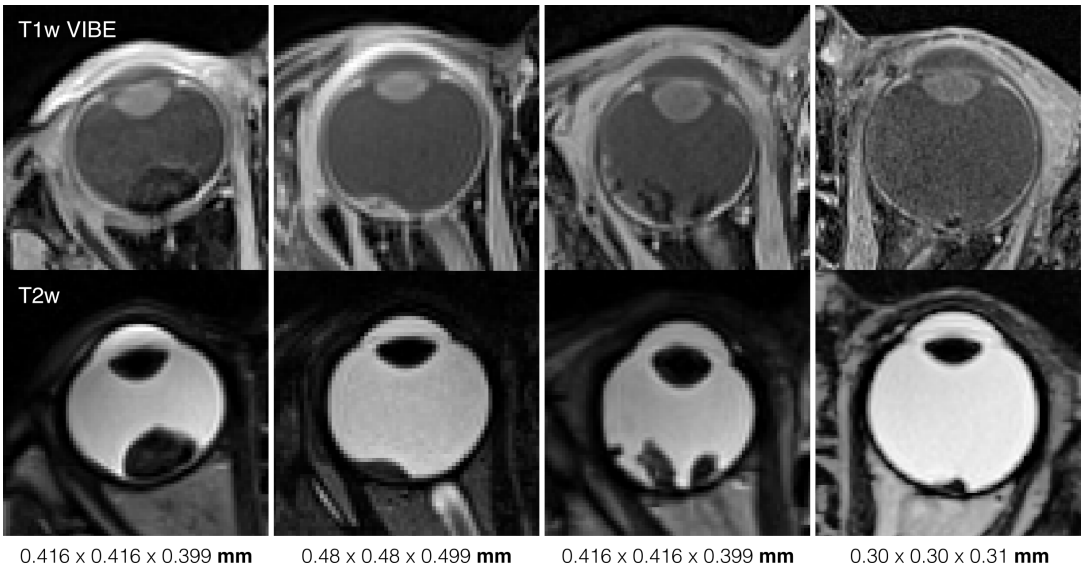

Figure 1.11 – **Retinoblastoma in MRI** : Four examples of patients with retinoblastoma inside the eye cavity. The size of the tumor and the spreading pattern may vary depending on location and treatment.

In addition to the economic factors, MRI remains an structural image modality, and resolution and acquisition time are an issue. Some of the pathologies that affect the ocular region are not easily detected when evaluated solely on MRI. Additional evaluations with more established image modalities, such as Fundus and US, are always required [31, 33, 37]. In-plane resolution is also a limitation for detecting retinal detachments. Such cases can pass unnoticed due to the resolution of the image, thus, screening the eye with non-isotropic sequences and in different planes is a common protocol during acquisition.

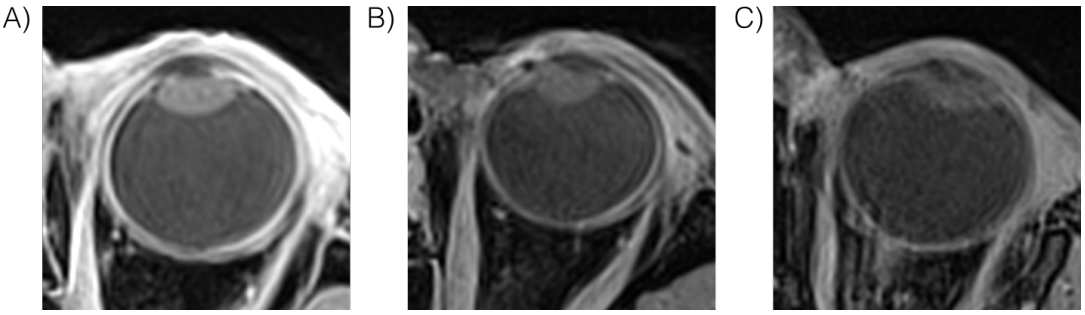

Figure 1.12 – **Limiting factors of MRI** : A-C) Three MRI scans from different adult patients. The region of the eyes is blurred due to the eye movement and saccades. Patients often need to remain immobile during 3-5 minutes.

Computed Tomography

CT is an image modality which combines x-ray scans taken from different angles in order to produce a cross-sectional image of the body in 2D and 3D. The working principle of the machine consists on the aggregation of these x-rays traversing the object of analysis and a group of sensors capturing the attenuation caused by the living tissue absorption. CT is an invasive medical image modality and is widely considered as an accepted alternative to the costly MRI exploration for adults [15].

In the context of eye imaging, CT is mostly used for confirmation of tumor extent in patients with uveal melanoma and prior to treatment planning [42, 54]. For the specific case of retinoblastoma, and due to the second malignancies related to imaging of newborns [13, 14, 33, 55], it is no longer recommended as image modality of use for theraphy planning. Literature recognized CT as the first modality of choice to detect optic nerve invasion and for detecting the tumor extent [56, 57], however, these conclusions appeared to be based on conflicting outdated experiments, without thorough evidence by radiologic-pathologic correlation studies, as stated in [37]. In this thesis we will focus exclusively on the study of 3D MRI and Fundus, not only because of the data limitations, but also to follow the latest research focusing on the use of these combined image modalities for evaluating ocular tumors [39, 55].

Optical Coherence Tomography (OCT)

OCT is a widespread non-invasive image modality for screening ocular pathologies starting at micrometric resolution. The technology, which was first publish barely 20 years, ago has evolved rapidly since its conception and now allows for a fairly easy screening of the layers that conform the retina and the anterior segment. For the avid reader, an extended review about OCT can be found in [1, 58].

The core working principle of OCT relies on low-coherence interferometry [1], using light sources that generate extremely short pulses, such as superluminiscent diodes or femtosecond lasers. This light in then divided into two beams, one containing the information that we want to acquire and the other is used as reference beam. The combination of the scattering light reflected from the sample and from the mirror that have traveled the same optical distance provide an interference pattern specific to that given point in space. By performing this action repeatedly accross the sample profile we can generate a vertical intensity profile called *A-scan*, which can be agregatted in a cross-section of profiles called *B-scans* and combined in 3D to generate the so called *C-scan*, as shown in Fig. 1.13. One of the particularities of OCT is that it allows many different scanning patterns, including temporal and frequential domain OCT [59, 60] and the possibility to scan the same region through time, in a specific manner called *M-scan*. Research in the area of OCT analysis and development is bountiful [18, 60, 61] and new frontiers such as full eye OCT including the anterior and posterior segment are closer everyday.

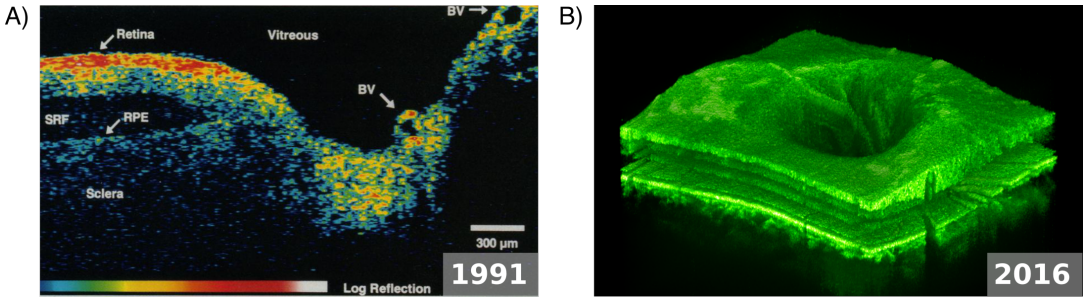

Figure 1.13 – **Evolution of OCT imaging** : Two pictures showing the evolution of OCT in the last 14 years. A) Shows the work presented by Huang et al. in 1991 [1] B) 3D C-scan acquired from a Heidelberg Spectralis ® machine.

Traditional OCT systems require patient cooperation during acquisition, thus, it is not quite adapted for the use in children with retinoblastoma [62]. The solution in the last years has been the introduction of hand-held intraoperative devices that solve this cooperation problems and allow for the screening of ocular tumors. Current protocols for screening do not rely much in OCT yet, mostly due to the nature and size of the tumor, however, further advances in the characterization of the cancer tissue would outcome in interesting studies about the pathology and the genetic factors that play a role in development of ocular tumors.

Medical Image analysis

Evolution of medical image analysis in the last forty years has been exponential. Since the explosion of general purpose computers in the 80´s, the distribution of devices for acquiring and processing medical images has grown together with computational power and its translational application a multitude of fields. The tools and knowledge that were required to compute the first complex 3D reconstruction of MRI and CT signals would not be a reality without the symbiotic link between fields, resulting in a community of researchers able to study the structure, the functions and the pathology of the human body via images. Today, medical image is composed of a complete set of pillars, including image segmentation, quantification, registration, enhancement and visualization, each of them comprising a populated field of research by itself. In this thesis we will focus specificilly on two fields, the statistical modeling field towards image segmentation and the machine learning field for image classification. For the avid reader, we would refer to the complete work in [63] for more information.

Image Segmentation

Segmentation is the process whereby we delineate a certain Region of Interest (ROI) in a medical image. This task is particularly important when it comes to characterizing regions in datasets of medical images, such as to indicate location and shape of organs, tumors or malignancies, towards further studying and analyzing the contoured region.

Research in this field has been very fruitful, and different ways to perform dataset labeling have been proposed. In the context of this work we will focus our efforts on the automatic segmentation of differents regions in the eyes, as well as the segmentation of pathological areas (see Fig. 1.14). This last contribution is important because it helps ophthalmologists and other clinicians to take decisions on treatment strategies (e.g. by looking at the size of the tumor) as well as to measure the evolution of the shape through time during follow-up. For completeness, we would direct the reader to the following works for an extensive reading in the field of image segmentation [64, 65].

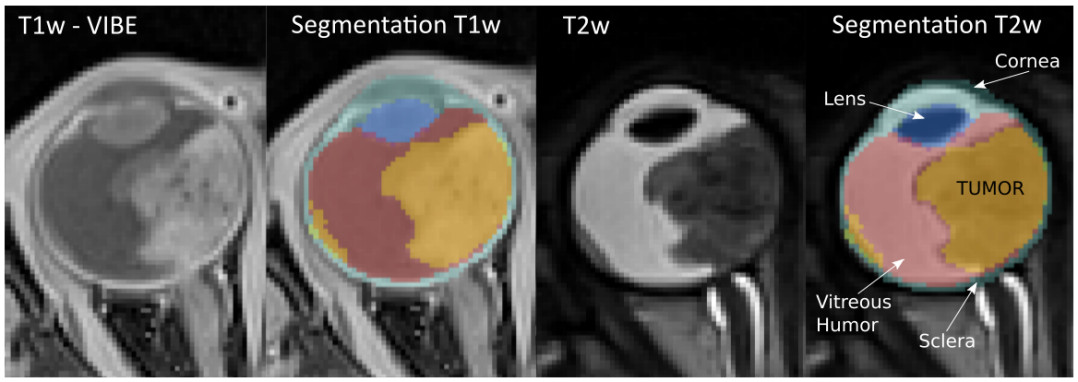

Figure 1.14 – **Segmentation of medical images in MRI** : Example of segmentation of medical images in 3D eye MRI. Manual delineation of the sclera, the cornea, the vitreous humor and the lens of a retinoblastoma patient. The process of manual delineation of these images may take between 2-3 hours.

Active Shape Models

For the first part of this thesis we will rely strongly on the theory of statistical modeling and model based methods, and more specifically, on the combination of those via ASM. Statistical models of shape are mathematical models that try to define the data-generating process out of a given population of samples, approximating a probability distribution for this data. Model based methods, on the contrary, make use of a prior model of what is expected to represent the image and attempt to find the best match from the model to this new image [66]. To focus the interest on the techniques of analysis applied in this thesis, we would like to address the reader to [67, 68] for further literature on the topic.

In this work we utilize ASM, a subset of model based methods that learn patterns of variability from a given population of annotated (*segmented*) images. These models learn the deformations inherent to the data and deforms exclusively in a way consistent to the data that was used to train them, in contrast to other free deformation methods such as Active Contour models [69]. The particularities of ASM as compared to different flexible models such as articulated models [70, 71], active contours [69] or statisticals models of shape [72, 73] is that of allowing this constrained deformation, especially tailored for human anatomy, where shapes look alike in a big variety of cases.

The working principle of ASM starts by selecting a set of points that represent the object shape, a task which is performed for every example in the dataset. This set of representative points should describe the shape as precisely as possible, and should not contain outliers. The so called *landmark points* will contain the shape of the figure, relevant anatomic points (i.e the center, details, ...) or the combination of both as to describe the shape in volume [67]. Once these point are selected, the volumes are aligned in a common NCS, the reason for aligning these is to study the statistics of the labeled point coordinates over the training set. From here, the aim is to minimize the weighted sum of squared distances between equivalent points accross shapes, thus, we iteratively modify the transformation matrix as to reach this goal [67].

Now the objective is to capture the statistics within the set of aligned shapes, for this, we need to create a Point-Based Shape Variation Model (PBSVM) using the techniques explained in [66, 67], that will encode the information representing the mean shape and the variation using Principal Component Analysis (PCA) [74]. The information representing the shape will be completely encoded into different *modes of variation*, which corresponds to the deformations representative for the independently encoded variability of the data. A more detailed explanation can be found in [66, 67] or in the Annex A of this thesis. In Fig. 1.15 we present an example of the model shape for the three first modes of variation of the statistical model of the eye we present in Chapter 2.

After the introduction of ASM, new approaches including Active Appearance Models (AAMs) [75] and Constrained Local Models (CLMs) [76, 77] appeared, however, give the small amount of data for training and the valuable results that were achieved with ASM we left the evaluation of similar techniques for future work. In Chapter 2 we further develop the use of ASM as a segmentation tool for different eye regions inside the 3D MRI.

Machine Learning in Medical Image Analysis

Machine Learning (ML) is the field of research that covers how to teach computers to perform a task wihout being explicitly programmed for it, reshaping internal decision making process based on the evaluation of data. Starting in the 50´s, after Alan Turing´s seminal work on Computing Machines [78], this field has traditionally pushed researchers to ask questions about similarities between humans and machines on how to *solve* human intelligence, however, despite the effort, a solution to replicate human intelligence is not yet close. Nevertheless, in the context of medical imaging, machine learning is key to succesfully tackle different challenges such as image segmentation, registration and modality fusion. In this section we will briefly introduce general ideas about machine learning applied to the context of classification and regression for image segmentation and registration. For the avid reader, please refer to [79] or [80, 81] for a complete revision about current machine learning theory and techniques.

The field of ML is typically divided into three categories, depending on the nature of the problem they are tailored to solve: i) supervised learning, where the goal is to learn a decision road map given an input and a solution output, ii) unsupervised learning, where the objective

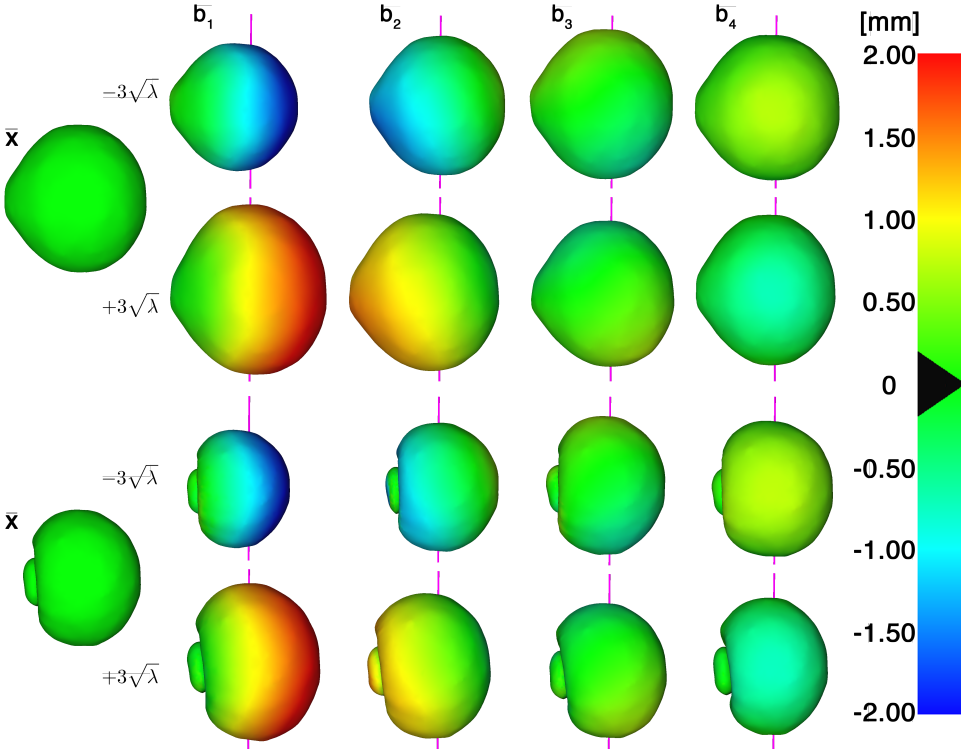

Figure 1.15 – **Active Shape Model - Modes of variation** : Model mean shape ($\bar{x}$) indicating the region of the sclera (upper left) and the vitreous humor and the lens (down left). First, second, third and fourth (b_1, b_2, b_3, b_4) mode of variation and effects in shape deformation colored in mm. wrt. the distance to the mean shape.

is to find a structure inherent to the data by analyzing solely the same input data and iii) reinforcement learning, which consists in the continuous interaction with the environment to receive an input that will allow the agent to achieve a certain goal. For the specific case of medical imaging, the research is mostly focused on the fields of supervised and unsupervised learning, and within it, we will focus on the task of classification.

Classification using ML techniques has been a very hot topic in the medical imaging community in the last years [82]. Traditionally, clinicians are interested in the early diagnosis of the pathology and in understanding the progression or severity of the disease. These two tasks can be divided into classification and regression respectively. Furthermore, for the specific case of segmentation, widely covered in this thesis in Chapters 2-3, the task can generally be modeled as a classification problem, where a ML algorithm will *learn* how to distinguish pathological from non-pathological tissue, or between different anatomical regions of interest. Among the most important classifiers in the field of ML for image classification we highlight Support Vector Machines (SVM) [83], RF [84], or Neural Networks (NNs) [85].

In the last couple of years, though, advances in computational power, the field of computer vision (from which medical imaging has always received inspiration) and applications of

Graphical Processing Unit (GPU) from video game industry have opened the door to more advanced image processing techniques using CNNs. A CNN is a type of feed-forward NN in which connections between different neurons are inspired by biological processes and Multi-layer Perceptron (MLP) [86]. The particularity of this approach is that every neuron processes a small portion of the image at a time, and tries to learn the features in their receptive field only by looking at the whole training dataset. Furthermore, the use of convolutions has the goal of reducing the number of parameters connecting every building block of the network. In this thesis we will include an accurate description of the CNN techniques we used for segmentation and classification as part of the methods in every chapter. Nevertheless, we recommend the reader to visit [87–91] for getting more familiar with the field of Deep Learning (DL) and advanced ML.

Fusion of multiple image modalities in Ophthalmology

To cover this last section of the background and literature, we will provide a short overview of the different methods for fusion of multiple image modalities in ophthalmology, more specifically, Fundus and MRI. As stated before in section 1, when it comes to imaging ocular tumors, clinicians require to evaluate independent sources of data, and to decide treatment based on multiple image modalities. For the specific case of retinoblastoma, the decision is taken by the radiologist and the ophthalmologist, who may have different perspectives and modalities of preference. Furthermore, the technique of choice comes with a series of implications, for instance, for the case of MRI, even though it enables volumetric characterization and detection of calcifications (an information that cannot be seen in Fundus) still sensitivity is not enough as to be the sole image decision driver, and other modalities are required (i.e US). Alternatively, for the case of vitreous and subretinal seeding and detachment, tumor seeding can often be seen in Fundus, but not in MRI [92, 93].

The literature in the field of fusion is not very broad and only the work by De Zanet et al. [94] attempts to combine those image modalities, paving the way for a combination of macro structural data, in the order of milimiters, with microstructural data, with a scale in micrometers. Unfortunately, in the context of ocular tumors, data is scarce, and proper multi-modal imaging of such patients is an endeavor difficult to pursue. In this thesis, we will explore what we believe is the first attempt to achieve multi-modal fusion of pathological MRI and Fundus in chapters 4 and 5.

2

Automatic Segmentation of the Eye in 3D MRI: A novel Statistical Shape Model for treatment planning of Retinoblastoma

The work presented in this chapter was originally published as C. Ciller, S. I. De Zanet, M.B. Rüegsegger, A. Pica, R. Sznitman, J-P. Thiran, P. Maeder, F. L. Munier, J. H. Kowal, M. B. Cuadra **"Automatic Segmentation of the Eye in 3D MRI: A novel Statistical Shape Model for treatment planning of Retinoblastoma", Internation Journal of Radiation Oncololgy Biology Physics 2015 (92)4 , pp. 794-802, 2015**. A 1-page peer-reviewed conference abstract and poster were originally presented at s C. Ciller, S. I. De Zanet, A. Pica, J-P. Thiran, P. Maeder, F. L. Munier, J. H. Kowal, M. B. Cuadra, **"Automatic magnetic resonance imaging segmentation of the eye based on 3D Active Shape Models", Investigative Ophthalmology & Visual Science, 2014 (55)13, pp. 5848-5848**.

2.1 Introduction

Retinoblastoma is the most common form of intraocular tumor in children and affects roughly one in every 18.000 newborns worldwide [31, 95]. With 90% of cases identified by the age of three, most retinoblastomas are curable, especially when the tumor is confined to the area between the retina and the surface of the VH [37]. For this reason, accurate and non-invasive techniques that can be used for early diagnosis assessment and the tumor extent follow-up or treatment planning are critical.

Today, Fundus image photography and 2D US are the key image modalities of choice for the diagnosis and follow-up of intraocular tumors [33]. CT is often regarded as a superior tool for the detection of intra-tumoral calcifications within the eye cavity, however, it induces ionizing

radiation, which has a more negative effect on children than adults. Furthermore, ionizing radiation has been shown to modify the patient´s radio-susceptibility (RS), thus affecting the carriers of the RB1 germline mutation that are responsible for retinoblastoma. Moreover, there is very little evidence regarding the diagnostic accuracy of CT in the context of advanced retinoblastoma [55], and thus, it is less recommended for imaging the disease [33].

Over the last decade, the ophthalmic community has become increasingly interested in Magnetic Resonance Imaging MRI [96], mainly due to the favorable tissue contrast and improved image resolution [97]. MRI sequences provide a remarkable soft tissue information source, with the resolution comparable to the information extracted from]CT [98]. Additionally, recent studies [14, 37] have provided direct evidence for the usefulness of MRI in both diagnosis and the treatment follow-up of retinoblastoma, and that the combination of both MRI and US would be sufficient to account for all calcifications found using CT. Consequently, quantitative analysis of the eye Magnetic Resonance (MR) images is needed to support the diagnosis and therapy planning with a better and faster eye anatomy delineation. In this context, the existence of a robust and accurate segmentation tool for eye MR images would offer an unprecedented opportunity for multimodal patient specific eye modeling. That is, combining modalities such as Fundus imaging, US with MRI for treatment planning of the eye[14, 98–100].

Until now, the task of segmenting the eye in medical images has been completed predominantly by using a pre-established set of parameters. **EYEPLAN** [101], a framework that estimated the shape of the lens, the cornea and the sclera, does so by combining parametric spheres. In comparison, **OCTOPUS** [49], currently widely used in modeling the eye inside CT, employs the same concept but models the eye as combinations of ellipsoids. Both these methods require an expert to pre-select visual landmarks. In addition, they have constrained modeling capabilities, as they limit the eye-growing pattern as a linear function dependent on the age of the patients. As such, they do not accommodate for a free growing pattern that is representative of a real eye population. The recent image processing techniques have opened the door to designing more complex models, which enable the segmentation of more regions of interest (ROI) within the eye. In 2006, Singh et al. [102] proposed a segmentation method for MRI based on spherical meshes that leveraged the posterior corneal pole and a sphericity modifying parameter. More recently, Bach Cuadra et al. [98] designed an algorithm combining parametric active contours with an ellipsoid model, which offered more accurate segmentations of the sclera and the lens on the CT and US images. Despite these advances, the eye treatment planning is far from being optimal.

One key element lacking in the above-mentioned parametric models is the statistical information that can be extracted from the variability of a population. This type of information is offered by Statistical Shape Model (SSM). These models use a previously trained, constrained model-based algorithm that can account for the deformation of the shape of a structure. Among the SSM, the ASM, proposed by Cootes et al. [67], are among the most successful. They have been applied to numerous medical imaging applications [68], mainly to construct

automatic segmentation frameworks by using both intensity and shape variation information [77, 103, 104]. Here, Ruegsegger et al. [99] proposed a semi-automated method, requiring minimal user interaction to segment the sclera, the cornea and the lens on CT images of adult patients [99].

With the aim of providing an accurate method for eye segmentations in MR images, we present an eye model that can capture both the shape variation and the intensity information from a set of gadolinium enhanced T1w GE VIBE MR sequences used for retinoblastoma imaging. The proposed 3D MRI ASM is, to the best of our knowledge, the first statistical model of the eye based on MRI data. Importantly, it also involves a fully automatic segmentation of the sclera, the cornea, the lens and the VH. We evaluated our model on a sample of 24 images of healthy children´s eyes and validated it quantitatively using a leave-one-out cross validation test. Our experiments show an average DSC of $91.6 \pm 2.20\%$ for the ROIs. In addition, we applied our method on two pathological patient eyes with retinoblastoma and have quantitatively highlighted the benefits of our approach with an average DSC of $93.45 \pm 0.93\%$.

2.2 Materials and Methods

Our segmentation procedure can be summarized as follows. We start by constructing an atlas of the eye regions [105]. We then extract an eye PBSVM and couple it with the intensity information to build an ASM. Then, to segment a new subject, we follow a two step process. First, we automatically find a number of landmarks within the eye to initialize the alignment of the model, and second, we fit the ASM to the volume. A visual depiction of our framework can be seen in Fig. 2.1.

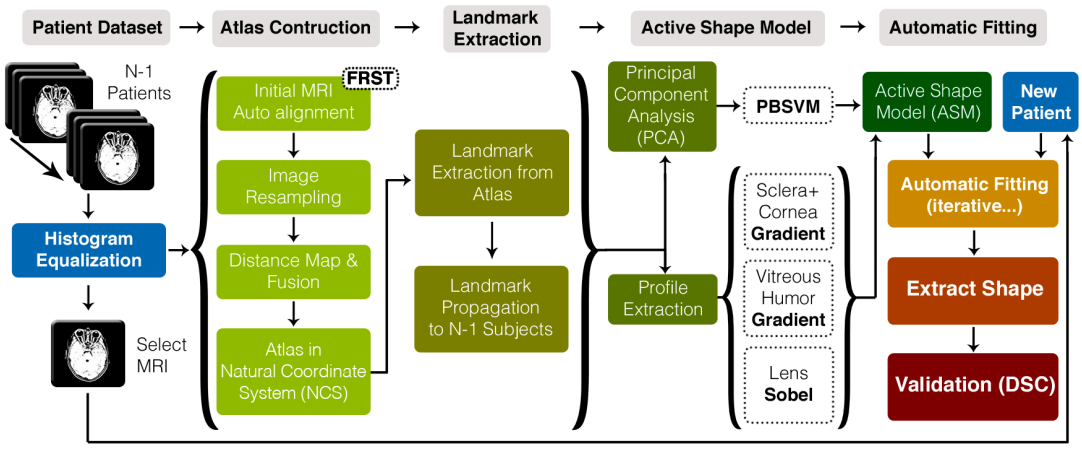

Figure 2.1 – **Framework automatic segmentation of the eye :** Block diagram representing the fully automatic segmentation framework. We create a model with N-1 Patients and test the performance on the remaining subject.

2.2.1 Training data set and manual segmentation:

The dataset used to develop our statistical model is composed of 24 healthy eyes gathered from children aged 3.29 ± 2.15 years (see Fig. 2.2, from 4m to 8y8m). All patient information in our study was anonymized and de-identified by physicians prior to our analysis and the corresponding institution approved the study. MR imaging was performed using a 3T Siemens Verio (Siemens, Erlangen, Germany), with a 32-channel surface head coil attached. The images are gadolinium enhanced T1w GE VIBE (TR/TE, $20/3.91ms$, flip angle, 12 deg) [52], and were acquired with two differing spatial resolutions: $0.416x0.416x0.399mm$ and $0.480x0.480x0.499mm$. The images include the head of the patient, both eyes and the optic nerves. Images are resampled to a common voxel spacing of $0.416x0.416x0.399mm$. During imaging, the patients were under general anesthesia [37].

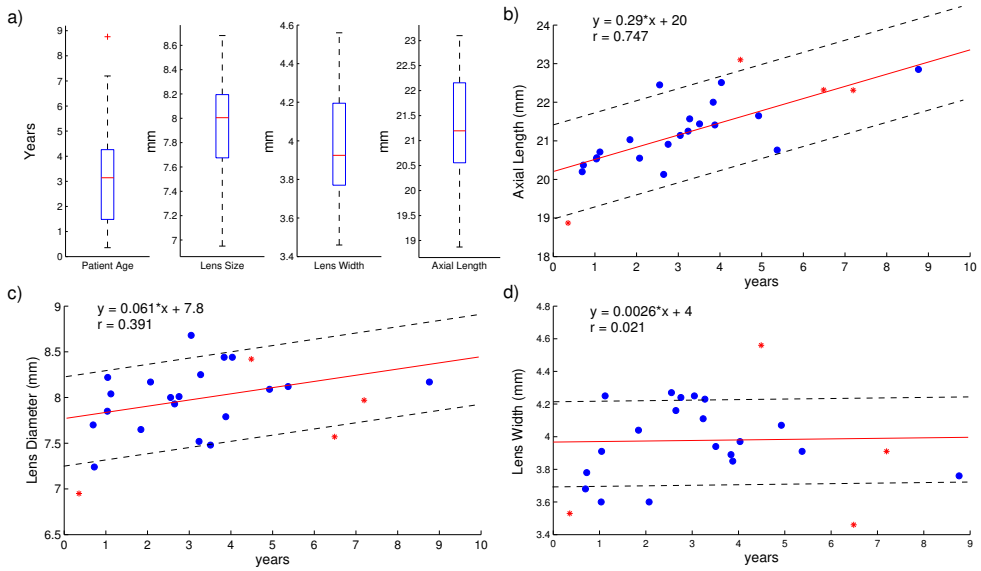

Figure 2.2 – **Patient dataset Information :** a) Dataset information distribution. b) Age vs. Axial length. c) Age vs. Lens size. d) Age vs. Lens width. Highlighted values in red are Sub03, Sub07, Sub14 and Sub15.

In order to validate our method, an expert radiologist manually segmented all volumes by labeling the following anatomical structures: sclera, cornea, lens, VH and OD. As described below, an atlas is then created based on the segmented volumes of every patient. Furthermore, axial length, lens size and width statistics were extracted and compared with the age of the patients. We observed a strong correlation between age and axial length (Fig. 2.2b), as described by Fledelius and Christensen [106], but a weak correlation between age and lens size and between age and width (Fig. 2.2c-d).

For initialization and detection of the eyes, we apply the method proposed by De Zanet et al. [94], based on the Fast Radial Symmetry Transform (FRST) algorithm. We automatically detect the center of both eyes in all patients (Fig. 2.3), even in the case of enucleation or

pathology. From the dicom file orientation information, we define whether it is the left or right eye. This information enables us to flip the volume over the transversal plane and mirror it for both eyes when required. We then crop the MRI head volume into two smaller Volumes of Interest Volume of Interests (VOIs) of size $40x40x40mm$ for both eyes. Next, we retrieve the location of the center of the lens, the optic disc, and the VH (Fig. 2.3b) [94]. These 3 points provide the initial alignment for building the atlas and for the fitting of a new patient.

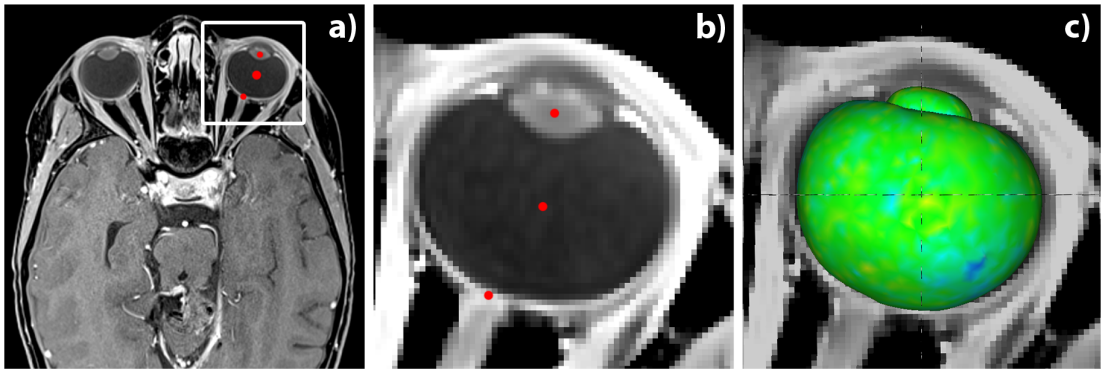

Figure 2.3 – **Detail of 3D MRI :** a) MRI volume, highlighting automatic cropping region and landmark initialization. b) Pre-processed MRI region of the eye including landmarks. c) Segmentation results for the lens and the VH.

2.2.2 Atlas construction :

We apply a rigid *(i.e. translation and rotation)* pre-registration step to the whole patient dataset. Both the center of the VH and the lens were used for the translation, and the optic disc position was used for the rotation. We then compute the distance map of the manually segmented regions, fuse them, and create a baseline atlas. Afterwards, we obtain, for each patient, the deformation field (non-rigid free diffeomorphic demons) against the baseline atlas [107]. Finally, we apply the mean deformation field to the baseline atlas to obtain the atlas in natural coordinate system NCS [105].

2.2.3 Point-Based shape variation model (PBSVM):

We represent the surface of the atlas in NCS as a point cloud by using a mesh extraction algorithm [108]. This is followed by a Gaussian smoothing and a decimation to the regions of the sclera, the cornea and the VH by 85% and by 10% for the lens. The information lost during the decimation step never induced an error over $0.01mm$ in average for all ROIs.

Once the surface is extracted, we warp the atlas back to the patient using non-rigid diffeomorphic registration [107]. The new atlas landmark positions for each subject are then transformed to a tangent space (Eq. 2.1) to preserve the linearity of the PBSVM, as expressed by Cootes et

al. [67] in

$$x_t = \frac{|\bar{x}|^2}{x * \bar{x}} \cdot x, \tag{2.1}$$

where x are the original surface points vector, $\bar{x}$ is the mean overall surface shape and x_t is the new projection of the surface points in the tangent space. The PCA [109] on the projection is done to extract the principal components of the point cloud distribution in space. The combined information is known as the shape variation model, and is stored in the form of

$$x \approx \bar{x} + \Phi b \tag{2.2}$$

where $\bar{x}$ is the mean shape, represented as a vector of t points, $\Phi = (\varphi_1|\varphi_2|...|\varphi_t)$ is a matrix which contains the eigenvectors corresponding to the variation of the model at each point, b is a t-dimensional vector representing the modes of variation. By modifying the b_i value under the constraints $\pm\sqrt{\lambda_i},\ i = 1..t$, we constrain the model to be within the range of similar shapes to the training set. For every position in b, λ is the eigenvalue corresponding to the Φ matrix. We assume the shape to be represented as a normal distribution of points along shapes $\pm 3\sigma_i$ [67, 99, 105].

2.2.4 Active Shape Model (ASM) :

We connect the PBSVM described in the previous section with the MRI intensity information and create an ASM. In contrast to CT, MRI does not provide fix intensity values across patients. Therefore, we use the standardization equalization algorithm proposed by Nyul and Udupa [110] to standardize the dataset.

Once the dataset has been equalized, we pre-process the MRI volumes with an anisotropic diffusion gradient filter, and window the image intensity to highlight the region of the eyeball and lens. We fix an arbitrary common upper and lower threshold for the windowing and extract the intensity information at each landmark position. Then, we compute the gradient and the Sobel operators along the intensity profiles normal to the surface. Subsequently, we compute the gradient for the sclera/VH and the Sobel for the lens.

We then select an even distribution of points [111] over the surface of the different regions from the landmark point cloud list (350 points from the sclera-cornea and the VH, and 300 points for the lens). We extracted the surface normal at these given points and compute the mean gradient intensities or the mean Sobel profiles, as well as the covariance matrices. The length of the extracted profiles depends on the region. We extract a normalized profile gradient along 11 pixels for the sclera, the cornea and for the VH, and 9 pixels length Sobel profile for the lens.

2.2.5 Automated segmentation :

The segmentation of a new patient is as follows. First, the VOI is pre-processed in the same way as the images were processed during the ASM construction; the VOI is not resampled and maintains its original image resolution. We then scan the profiles normal to the surface of the model. These profiles are compared to the intensity profiles provided by the ASM, and a new matched point is set for each profile along the sampled voxels. The fitting is then reduced to an optimization problem where the Mahalanobis distance to the model shape is minimized [67] by reducing the overall distance between the current shape point and the matched point, while constraining the model to be within the deformation range of the PBSVM. In contrast to other work [99], the segmentation scheme that we apply here is twofold: we first fit the sclera and the VH and then once the optimum is found, we fit the lens independently (Fig. 2.3c).

2.3 Results

We assessed our segmentation method using a leave-one-out cross-validation test of the ASM. That is, we iterated over each patient, excluding it from the ASM construction and automatically fit the generated model to the excluded patient. The quality of the segmentations were evaluated by computing the DSC, where we considered the manual segmentation as the ground truth $DSC = 2 \cdot \frac{|A \cap B|}{|A|+|B|}$.

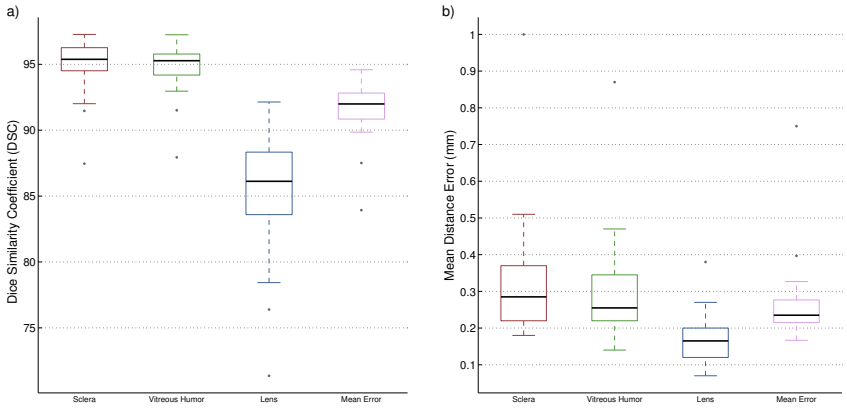

Figure 2.4 – **Leave-one-out cross validation :** a) Mean and standard deviation of DSC for independent and combined shapes. b) Mean distance error for every eye region and combined mean error.

Furthermore, for each patient and eye region, we computed the mean distance error between the patient ground truth surface and the automatic segmentation result (Fig. 2.4b). We report the distribution of mean distance error per point across all patients and regions in Fig. 2.5.

The average DSC over all subjects was $94.90 \pm 2.12\%$ for the sclera and the cornea, $94.72 \pm 1.89\%$ for the VH and $85.16 \pm 4.91\%$ for the lens. Fig. 2.4a) summarizes the mean DSC. The mean

distance error is $0.33 \pm 0.17mm$ for the sclera and cornea, 0.30 ± 0.15 mm for the VH and $0.17 \pm 0.07mm$ for the lens (Fig. 2.4b), with a mean global distribution error of $0.27 \pm 0.09mm$ per patient. The entire segmentation process takes 14s. per eye on average using a Pentium i7 3,4 GHz QuadCore 8GB RAM.

Finally, we applied our segmentation on two patients with retinoblastoma. In these cases, the model was robust in detecting the presence of tumors, even when these were large (Fig. 2.6). We obtained a DSC overlap of 94%, 93.98%, and 92.37% on average for sclera+cornea, VH and lens, respectively.

2.4 Discussion

The present work describes a method for automatic segmentation of MRI of the eyes based on a 3D ASM. Our approach is, to the best of our knowledge, the first framework for automatic extraction of the eye shape with dedicated regions of the sclera, the cornea, the VH and the lens in the MRI.

We have demonstrated that our model enables to accurately segment the eye, with an average error for all ROIs always under the minimum resolution threshold ($0.399mm$) and never reaching more than $1.2mm$ (Table 2.1). The results highlight an accurate fit for the posterior part of the VH, where the macula and the optic disc are located (Fig. 2.5a). Furthermore, we noticed a bias towards having over segmentation errors in the frontal part of the eye (Fig. 2.5b-c). This situation caused the lens to yield a lower average DSC (85.16%) than for other regions. The results can be explained due to the small size of the lens in contrast to the sclera and the VH. This limitation of the DSC index for small regions was already reported by several authors in the field [112, 113].

Within the dataset, we identified an outlier ((Table 2.1, Sub07) that presented the lowest accuracy during segmentation across all ROIs. This is due to the small size of the eye (youngest patient with 4 months) that made him not well represented by our model. In the future, a larger dataset with greater number of younger patients (< 6 months) would address this issue. Furthermore, we also observed that Sub03, Sub14 and Sub15 perform below average during the lens fitting. Nevertheless, there is a general trend towards robust segmentation of the sclera, cornea and vitreous humor, even in cases with a strong variation in eye axial length size. The final outcome is that lenses in eyes whose size are closer to the mean shape size are better segmented than extreme-size eyes (Table 2.2).

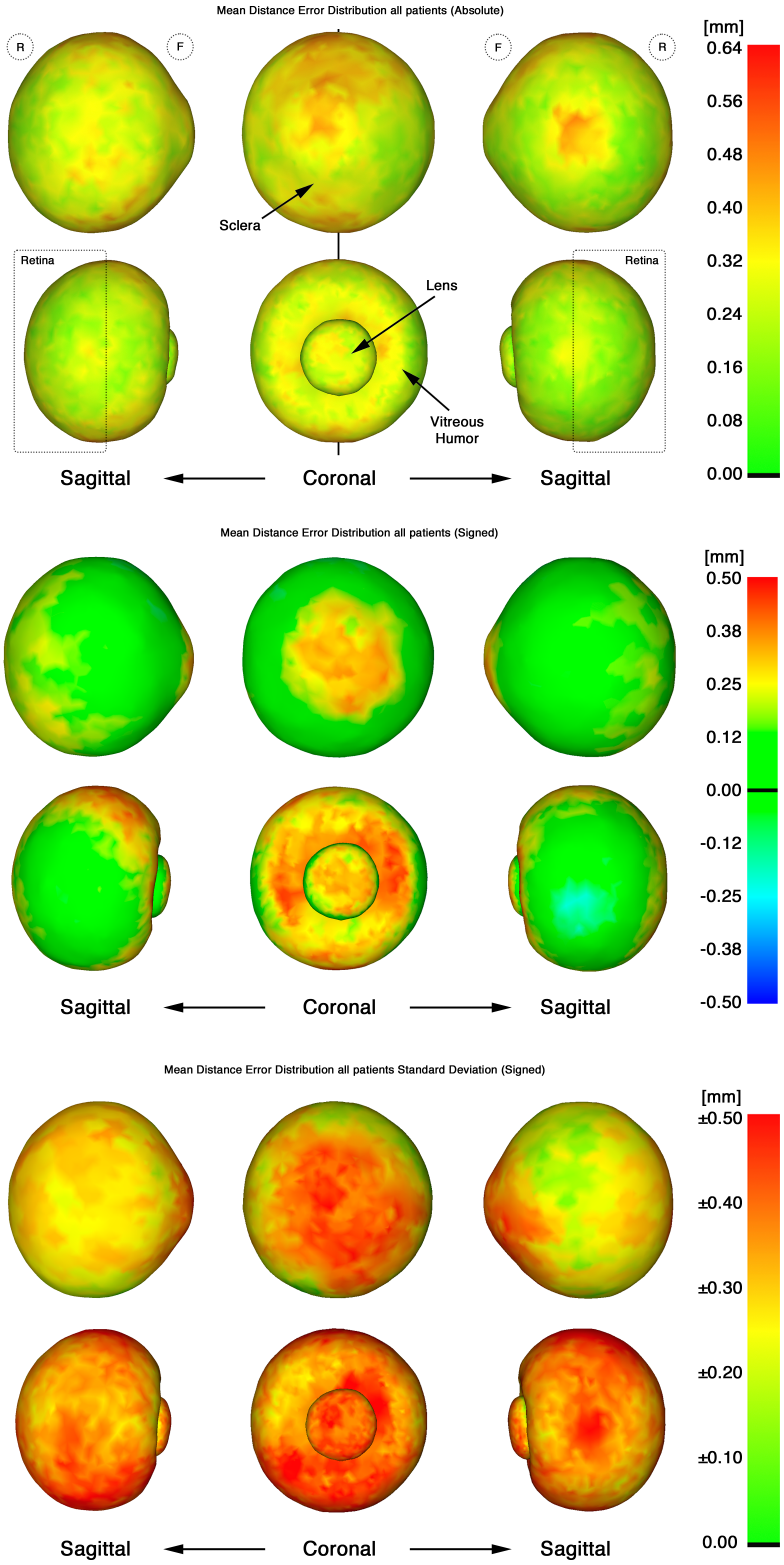

Figure 2.5 – **Mean distance error distribution :** Mean distance error distribution with respect to the manual segmentation. a) unsigned and b-c) signed distance error to display bias towards over-segmentation or under-segmentation.

Our work demonstrates a novel application of statistical modeling techniques to treatment planning and diagnosis confirmation of intraocular tumors, such as retinoblastoma. The speed, robustness and reliability of the present method are evidence that it can accommodate the variability existing in the size of eyes, as well as solving minor eye orientation issues during the fitting process. Similarly to the presented children eye model and pathological eyes, our framework can be directly applied to create a model for adults, for instance, for delineation of the uveal melanoma prior to therapy planning. Uveal melanoma presents a very similar MRI imaging conditions to retinoblastoma, therefore, leveraging the current framework to pathological adult eyes could be the next step.

2.5 Conclusions

Although previous works attempted to delineate or characterize the MRI imaged eyes using a manual qualitative evaluation, we are first to report quantitative results on the segmentation accuracy on MRI. The procedures that we used can provide the basis for objective assessment of the quality of the model fitting in the eye MRI, as it did in other image modalities such as CT. Furthermore, the robustness of the model during the segmentation of pathological MRI volumes indicates an important and promising step towards facilitated treatment planning and tumor extent follow-up. A higher MRI diagnostic accuracy for retinoblastoma, in particular for the detection of prelaminar optic nerve and choroidal invasion, is crucial for designing effective treatment strategies. Thus our future work will focus on quantitative evaluation in larger datasets.

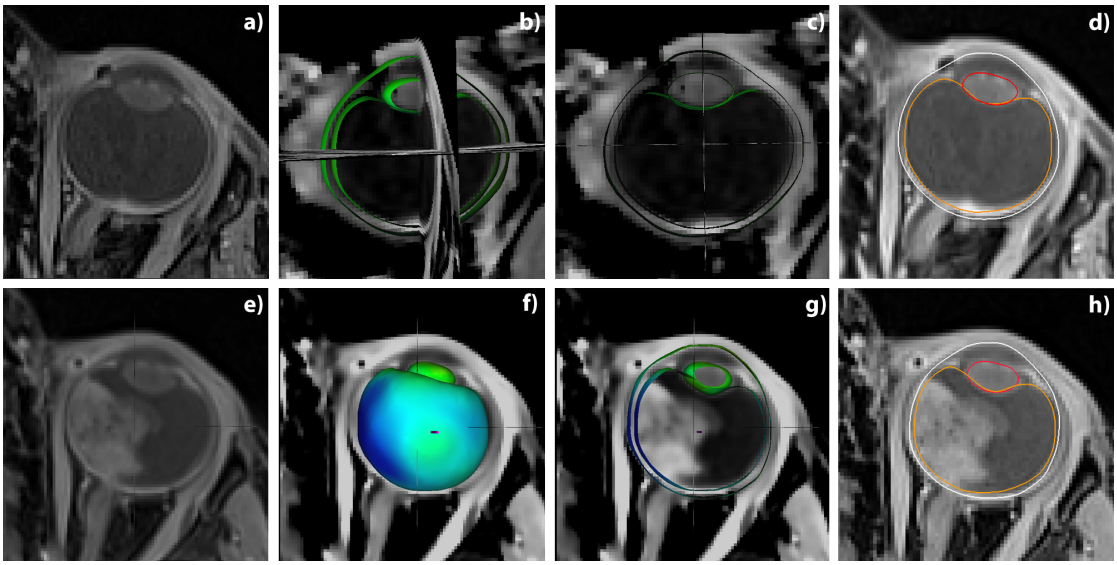

Figure 2.6 – **Pathological eye segmentation :** Patients with retinoblastoma in a) and e). Automatic eye segmentation for a small tumor present in the retina b), c), d). Robust fit of the VH and the Lens for large tumor in f), g), h).

To our knowledge, this framework is the most accurate and robust tool yet to fully and automatically segment the lens, sclera, cornea and VH regions in MRI. The presented approach provides a solution for reducing the time spent in delineating the eye shape and is likely to advance current ocular tumor treatment planning and diagnosis techniques.

Table 2.1 – Dice Similarity Coefficient (DSC) for Active Shape Model during leave-one-out cross-validation test. Mean overall error in (mm)/

	Sclera	**VH**	**Lens**	**Mean DSC**	**Sclera**	**Sclera Dev.**	**Max. Scl.**	**VH**	**VH Dev.**	**Max VH**	**Lens**	**Lens Dev.**	**Max Lens**
Sub01	96.23	95.6	86.75	92.93	0.36	0.07	1.19	0.39	0.08	1.19	0.1	0.03	0.57
Sub02	92.01	94.51	84.15	90.16	0.33	0.1	0.79	0.25	0.06	1.15	0.14	0.04	0.59
Sub03	94.89	94.8	79.85	89.34	0.28	0.09	1.59	0.23	0.06	0.99	0.16	0.04	0.57
Sub04	95.94	95.39	86.7	92.73	0.39	0.11	1.59	0.19	0.06	1.15	0.15	0.04	0.57
Sub05	96.51	95.94	81.79	91.57	0.29	0.06	0.93	0.34	0.08	1.24	0.08	0.03	0.57
Sub06	93.62	95.49	92.14	93.35	0.19	0.06	0.57	0.14	0.04	0.83	0.19	0.04	0.58
Sub07	87.46	87.94	76.39	84.2	1	0.22	2.38	0.87	0.19	2.46	0.38	0.1	1.25
Sub08	94.36	95.22	87.09	92.14	0.21	0.05	0.83	0.17	0.04	0.83	0.27	0.06	0.83
Sub09	97.27	96.69	87.46	93.37	0.25	0.05	0.9	0.3	0.06	1.19	0.07	0.02	0.41
Sub10	95.03	94.05	89.21	92.8	0.35	0.12	1.52	0.43	0.13	1.51	0.12	0.04	0.59
Sub11	96.45	97.24	90.07	94.4	0.45	0.07	1.27	0.22	0.06	0.9	0.11	0.03	0.57
Sub12	95.27	95.32	90.07	93.76	0.25	0.07	0.9	0.28	0.08	1.25	0.17	0.04	0.59
Sub13	94.66	93.67	85.6	91.35	0.38	0.16	2.03	0.43	0.17	2.04	0.17	0.04	0.83
Sub14	96.29	95.95	78.43	90.5	0.18	0.06	1.15	0.25	0.09	1.46	0.21	0.05	0.57
Sub15	96.17	95.01	71.36	87.69	0.19	0.05	0.79	0.26	0.08	1.71	0.25	0.07	0.93
Sub16	91.47	93.67	86.25	90.78	0.34	0.1	0.58	0.23	0.06	0.9	0.17	0.04	0.71
Sub17	96.54	95.13	83.6	91.7	0.19	0.05	0.92	0.15	0.04	0.83	0.23	0.07	0.93
Sub18	95.46	94.32	87.11	92.41	0.23	0.05	0.93	0.2	0.05	0.83	0.14	0.04	0.57
Sub19	93.8	91.51	91.52	92.34	0.23	0.06	0.83	0.26	0.06	0.58	0.17	0.04	0.59
Sub20	96.8	95.79	89.63	94.15	0.34	0.08	1.25	0.3	0.06	0.93	0.17	0.04	0.59
Sub21	95.71	95.77	83.58	91.6	0.2	0.06	1.19	0.22	0.08	1.27	0.08	0.03	0.42
Sub22	95.3	92.96	85.4	91.14	0.27	0.07	1.15	0.25	0.08	0.79	0.16	0.04	0.83
Sub23	94.82	95.89	85.99	92.44	0.5	0.09	1.31	0.35	0.07	1.24	0.12	0.04	0.58
Sub24	95.5	95.43	83.72	91.66	0.51	0.04	0.99	0.47	0.04	0.93	0.21	0.07	0.93
Mean	94.9	94.72	85.16	91.6	0.33	0.08	1.15	0.3	0.08	1.18	0.17	0.04	0.67
SD	2.12	1.89	4.91	2.2	0.17	0.04	0.43	0.15	0.04	0.43	0.07	0.17	0.19

Table 2.2 – **Patient Dataset Information :** Age, lens size, lens width and axial length

	Age (y.)	**Lens Size (mm)**	**Lens Width (mm)**	**Axial Length (mm)**
Sub01	3.51	7.48	3.94	21.44
Sub02	3.877	7.79	3.85	21.41
Sub03	6.488	7.57	3.46	22.32
Sub04	3.838	8.44	3.89	22
Sub05	0.696	7.7	3.68	20.2
Sub06	4.926	8.09	4.07	21.65
Sub07	0.356	6.95	3.53	18.87
Sub08	4.033	8.44	3.97	22.51
Sub09	5.373	8.12	3.91	20.76
Sub10	1.036	7.85	3.6	20.53
Sub11	2.071	8.17	3.6	20.55
Sub12	2.756	8.01	4.24	20.91
Sub13	2.649	7.93	4.16	20.13
Sub14	7.197	7.97	3.91	22.31
Sub15	4.49	8.42	4.56	23.1
Sub16	8.762	8.17	3.76	22.85
Sub17	3.236	7.52	4.11	21.25
Sub18	2.553	8	4.27	22.45
Sub19	3.274	8.25	4.23	21.57
Sub20	1.044	8.22	3.91	20.56
Sub21	1.841	7.65	4.04	21.03
Sub22	3.047	8.68	4.25	21.14
Sub23	1.121	8.04	4.25	20.71
Sub24	0.723	7.24	3.78	20.37
Mean	3.29	7.94	3.97	21.27
SD	2.15	0.4	0.27	1

3

Multi-channel MRI segmentation of eye structures and tumors using patient-specific features

This chapter continues with the work introduced in Chapter 2 and presents the first attempt to perform automatic multi-channel MRI segmentation of ocular tumors for T1w VIBE and T2w. A 10-page journal paper was submited to the **Plos One Journal** at the time of this thesis: C. Ciller, S.I. De Zanet, K. Kamnitsas, P. Maeder, B. Glocker, F.L. Munier, D. Rueckert, J-P. Thiran, M.B. Cuadra and R. Sznitman, **"Multi-channel MRI segmentation of eye structures and tumors using patient-specific features"**. A preliminary version of this work was originally submitted in the form of an 8-page conference paper to the *Medical Image Computing and Computer Assisted Intervention* conference in March 2016.

3.1 Introduction

Common forms of ocular cancer are related to high morbidity and mortality rates [33]. Imaging of these tumors has generally been performed using 2D Fundus imaging, 2D US or 3D CT. Recently, however, Magnetic Resonance Imaging (MRI) has gained increased interest within the ophthalmic community, mainly due to its remarkable soft tissue intensity contrast, comparable spatial resolution capabilities to 3D CT and non-ionizing properties [37]. Concretely, MRI is becoming a key modality for pre-treatment diagnostics of tumor extent, especially for retinoblastoma in children, and is gaining a great interest for treatment planning with external beam radiotherapy of uveal melanomas in adults.

For the case of retinoblastoma, a tumor that most often takes root and develops from the retina into the vitreous humor of children eyes [37] (Fig. 4.1), MRI is required to observe possible tumor invasion within the optic nerve, or to evaluate the appearance of recurrent tumors after treatment. Occasionally, treated tumors present second recurrent malignancies under

the calcified area, a pathology that can more easily be observed via MRI [33]. In this context, having accurate 3D segmentations of eyes with pathology would help better characterize and quantify intraocular tumors more effectively. This would not only allow for reliable large-scale longitudinal treatment-response studies but would also allow for direct imaging and targeting of tumors during treatment procedures, such as the applied in brachytherapy/cryotherapy to children with retinoblastoma [31].

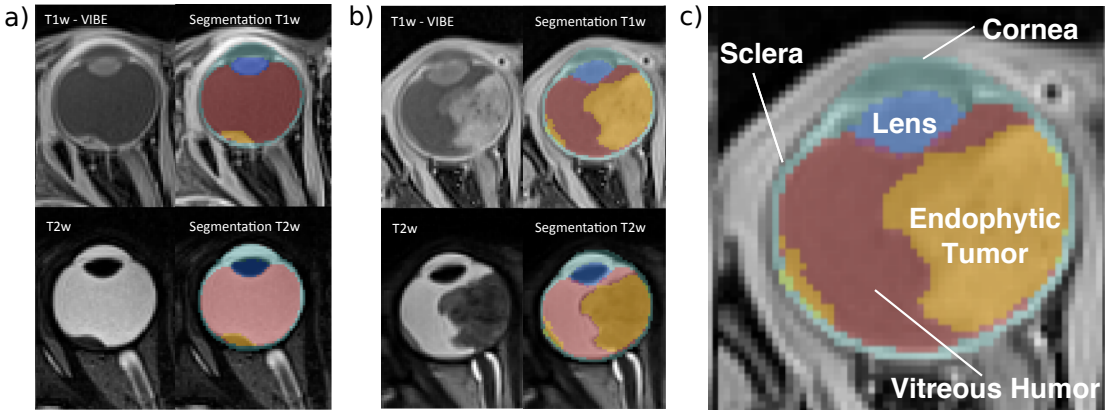

Figure 3.1 – **Patients with retinoblastoma** (a)-(b) Two example patients imaged with 3D T1w VIBE & T2w MRI (c) The eye lens (dark blue), vitreous humor (red) and sclera / cornea (light blue) are highlighted. Endophytic tumors delineated in yellow.

Unfortunately, and in contrast to neuro(-brain)imaging [114–119], the use of computer-aided techniques for 3D segmentation of the eye remains limited in ocular MRI and, to the best of our knowledge, none address the eye tumor segmentation problem. The accuracy of the existing brain tumor techniques strongly relies on many imaging sequences and on the tumor type they are tailored to (*e.g.* glioma or meningioma,). Thus, their direct application to ocular tumors is not straightforward, considering that only a few contrast images are usually available and, most importantly, they appear as extremely small structures as compared to brain tumors (Fig. 3.1-a)).

Today, existing methods for ocular segmentation of healthy structures in MR (and CT) rely on semi-automatic techniques based on parametrical models dedicated to segment the eye regions [49], thus only allowing for a coarse segmentation of different eye parts (*e.g.* eye lens or VH). Along this line, Active Shape Models (ASMs), originally introduced by Cootes et al. [67] have recently been proposed by our group to more precisely delineate eye anatomy using T1w VIBE MR and CT images [2, 99]. In that work, the main goal was to delineate healthy eye structures, but the challenge of eye tumor delineation has yet to be addressed.

In this chapter we introduce a novel segmentation framework dedicated to the ocular anatomy. We present a set of eye delineation techniques in 3D MRI, both for healthy structures and for pathological tissue. Our contributions can be summarized as follows:

- We present a new Pathological Eye Model (PM) of the eye, built out of pathological

patient eyes and compare the results with the HM presented in [2], achieving better healthy tissue segmentation performance.

- We introduce novel EPSF, derived from our pathological ASM, which help characterize pathological tissue, even when only small amounts of training data is available.
- We introduce a novel automatic segmentation framework tailored to ocular tumors. Similar to top ranking algorithms for brain tumor segmentation [120], our method makes use of a Markov Random Field (MRF) to represent the presence of healthy and pathological tissue, allowing for both local and neighborhood information to be utilized in a joint manner. Unlike existing brain tumor techniques, however, we encode prior information of the tumors by means of an active shape pathological model, contrasting the use of typical brain atlas priors or existing ASMs of healthy eyes.
- Furthermore, we validate our framework on a clinical dataset of T1w VIBE and T2w MRI from retinoblastoma patients and show that when EPSF are used, performance differences between state-of-the-art deep networks and other simpler classifiers such as RF are minor and improvements are visible across all cases.

We divide the following sections. First, the materials and methods section presents the clinical dataset, the segmentation of the healthy structures, the eye feature extraction process and our mathematical framework. Second, results comparing the classification performance between different experiments for both healthy tissue segmentation and pathological eye tissue delineation are presented. Third, we discuss about current eye treatment strategies and show the contributions of the presented approach for the future of ocular tumors in the MRI.

3.2 Materials and Methods

Our framework first makes use of an ASM [67] trained on patient data that contains tumors and which we refer to from now on as *Pathological Model (PM)*. Note that this model is trained exclusively on pathological eye MRI data, in contrast to our previous work [2, 99]. This model aims at delineating the regions of the sclera, the cornea, the lens and the vitreous humor in an automatic fashion. From this pathologically-based ASM, we propose the use of EPSF to characterize pathological tissue within healthy anatomy. We then leverage these features in a classical Markov Random Field (MRF) model to accurately segment eye tumors. Fig. 3.2 illustrates the complete framework which we now describe in detail.

3.2.1 Dataset

Our dataset is composed of 16 children eyes with endophytic retinoblastoma. The volumes represent a section of the head of the patient, both eyes and the optic nerve. MRI was performed in a 3T Siemens Verio (Siemens, Erlangen, Germany), with a surface head coil of 32 channels. Acquisition was done under general anesthesia. The images are gadolinium

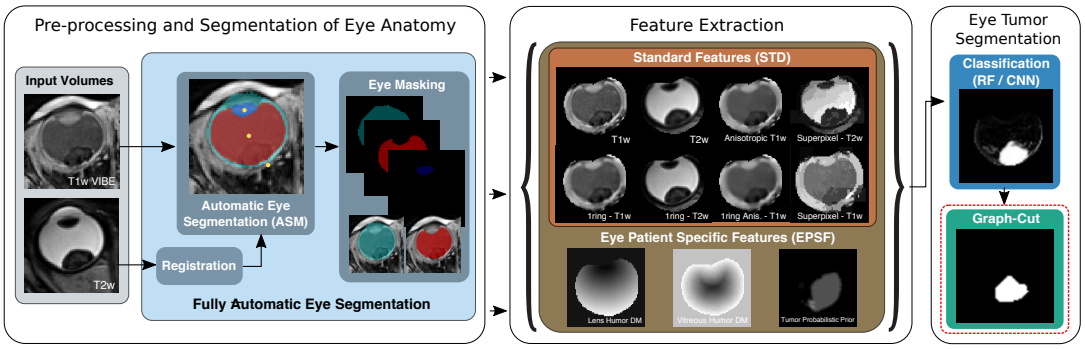

Figure 3.2 – **Proposed framework for automatic whole eye segmentation**. T1w and T2w 3D volumes are combined with EPSF features. These features are used to train a RF / CNN classifier, serving as the data term in Graph-Cut optimization.

enhanced T1w VIBE (repetition time/echo time, 20/3.91 ms; flip angle, 12°) acquired at two different spatial resolutions ($0.416 \times 0.416 \times 0.399\ mm^3$ and $0.480 \times 0.480 \times 0.499\ mm^3$, respectively) and T2w (repetition time/echo time, 1000/131 ms; flip angle, 120°) with a resolution of $0.453 \times 0.453 \times 0.459\ mm^3$. All patient information in our study was anonymized and de-identified by physicians prior to our analysis, and the study was approved by the Cantonal Research Ethics Committee of Vaud. For each eye, the sclera, the cornea, the vitreous humor, the lens and the tumor were manually segmented by an expert radiologist (see Fig. 3.1 and 3.2). We use these manual segmentations as ground truth for quantitative comparisons.

3.2.2 Pre-processing and segmentation of eye anatomy

Starting from the patient head-section MRIs containing ocular tumors, we begin by automatically locating the ROI around each eye. Following the landmark-based registration described in [2, 94], we detect the center of the VH, the center of the lens and the optic disc and use this information to align the eyes to a common coordinate system. This pre-processing allows us to form a coherent dataset representing the same anatomical regions across subjects. In particular, we let our image data X for a patient n consist of both T1w VIBE and T2w volumes which have been co-registered using a rigid registration scheme, rescaled to a common image resolution, intensity-normalized for all eye volumes [110] and cropped to the ROI.

Using manual delineations of the sclera and the cornea, the eye lens and the VH we learn an ASM [67] for these structures jointly. Note that we do not include the delineations of tumors inside the model, but implicitly encode this information from the profile intensity information for the sclera and the VH, as can be seen in Fig. 3.3. With this, we can segment such healthy structures in any subsequent eye MRI. As we will show in Sec. *Results*, learning an ASM on pathological patient data provides improved segmentation accuracy as compared to healthy-patient ASM models eye models [2].

Furthermore, in order to ease the process of learning the tumor classifier, we will only consider

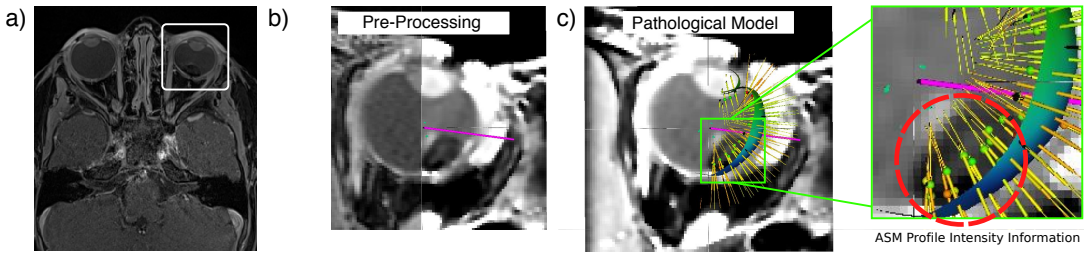

Figure 3.3 – **Learning a Pathological Eye Model (PM)**. We follow the steps in [2] to (a) automatically detect the eye in the 3D MRI, followed by a set of b) image pre-processing techniques to learn information of pathological and healthy structures jointly using c) intensity profiles containing pathological information.

voxels at a Euclidean distance of $\theta = (0,2)$ mm from the VH delineation result. That is, we only evaluate voxels that are close and within the VH, upper bounded by the maximum segmentation error of the ASM (see Fig. 3.2, brown-colored box). The main purpose at this stage is to focus exclusively on the tumor segmentation, reducing the observable region to the VH plus an additional confidence at a distance θ from the boundary.

3.2.3 Feature extraction

We let $\mathbf{f}_i^{STD}$ at voxel location i denote STD defined as the concatenation of T1w and T2w voxel intensities, the anisotropic T1-weighted (A-T1w), and the average 6-voxel von-Neumann neighbors (6 nearest neigbors) of the T1w, T2w and A-T1w. On their own such features provide standard intensity information to the appearance of both healthy and pathological tissue (see Fig. 3.2, brown-colored box).

Given a segmentation of healthy eye structures, we are interested in establishing image features that provide appearance and *contextual* information regarding pathological tissue as well. To achieve this goal, we begin by applying the learned ASM (see Sec. *Pre-processing*) to the eye MRI, thus providing a delineation boundary for the lens and VH. Then, we assign to each voxel i in the volume a rank relative to the Euclidean distance to the surface border of both the lens and the VH. More specifically, the rank at each voxel is defined as,

$$\mathbf{f}_i^l = \min_{b \in B_l} |i-b|_2^2, \qquad \text{and} \qquad \mathbf{f}_i^{vh} = \min_{b \in B_{vh}} |i-b|_2^2, \tag{3.1}$$

where B_l and B_{vh} are the boundary voxels of the eye lens and VH, respectively. These features can be interpreted as distance maps resulting from the pathological ASM segmentation.

In addition, in order to leverage prior information on the tumor locations, we also use the ground truth tumor locations within our training set, to construct a tumor location likelihood feature, $\mathbf{f}_i^t = \frac{1}{N}\sum_{n_1}^{N} Y_i$, where $Y_i = 1$ if the voxel at location i is part of the tumor and where N is the total number of volumes in the training set. Smoothing $\mathbf{f}^t$ is then performed by using a 3D Gaussian kernel ($\sigma = 3$ mm) to regularize the tumor prior. This value was arbitrarily chosen as to create a smooth yet precise representation of the tumor distribution inside the eye. In Fig.

3.2 you can find an example of these feature maps.

Our EPSF for each voxel is then constructed by concatenating the following rank-values: $\mathbf{f}_i^{EPSF} = [\mathbf{f}_i^l, \mathbf{f}_i^{vh}, \mathbf{f}_i^t]$. As illustrated in Fig. 3.2, this effectively characterizes patient-specific anatomy (via $\mathbf{f}_i^l$, $\mathbf{f}_i^{vh}$) and a location specific tumor likelihood (via $\mathbf{f}_i^t$), allowing both local and global information to be encoded in a compact feature at voxel level.

3.2.4 Eye Tumor Segmentation

General mathematical framework

Now, to segment the eye tumor tissue, we make use of a MRF to model the joint distribution of all the voxels $P(Y, X|\mathscr{M})$, where $Y = \cup_i Y_i,\ Y_i \in \{0,1\}$ represents the presence of a tumor at location i, X is the MR volume and $\mathscr{M} = \mathscr{M}_1, \ldots, \mathscr{M}_S$, represents the different healthy eye structures,

$$P(Y, X|\mathscr{M}) = \frac{1}{Z} \prod_i P(X_i|Y_i, \mathscr{M}) \prod_{j \in \mathscr{N}_i} P(Y_i, Y_j|\mathscr{M}), \tag{3.2}$$

with normalization factor Z, likelihood model $P(X_i|Y_i, \mathscr{M})$ and smoothness prior $P(Y_i, Y_j|\mathscr{M})$. From this, we can simplify this expression to,

$$P(Y, X|\mathscr{M}) = \frac{1}{Z} \prod_i P(\mathbf{f}_i|Y_i) \prod_{j \in \mathscr{N}_i} P(Y_i, Y_j), \tag{3.3}$$

by assuming that (1) the prior is independent of the underlying eye structure and that a single model accurately describes the neighborhood interactions and (2) instead of modeling the likelihoods as a function of a given structure, we approximate it by leveraging our patient-specific features that are implicitly indexed on $\mathscr{M}$. Using this model, we can then use a standard Graph-cut optimization [121, 122] to infer the tumor segmentation. The presented approach is particularly powerful because the topology of our segmentation is not restricted to a single structure and allows refining segmentation on multiple isolated parts.

Likelihood prior

The likelihood prior, defined as $P(\mathbf{f}_i|Y_i)$, provides the probability for every voxel i within the 3D volume to represent either tumor or healthy tissue $Y_i = \{0,1\}$. In this work we conduct a set of experiments with two scenarios, a) a rather simplistic voxel-based RF classifier and b) a state-of-the-art CNN [119], which leverages the power of 3D convolutions to perform the same classification task.

RF classification: We train a RF classifier [123] with 200 trees, using all positive voxels ($Y_i = 1$) in the training set and 20% of the negative voxels ($Y_i = 0$) to balance the number of samples. As in [124], SLIC superpixels [125] are computed on each 2D-MR slice (*i.e.* region size of 10 voxels and a regularization factor $r = 0.1$), from which mean superpixel intensity at position i was aggregated for both T1w and T2w. SLIC features support the voxel-wise classification by

providing intensity context based on the surrounding area.

The number of trees was selected by reaching convergence with Out-of-Bag estimation, testing RF performance with a varying number of trees from 50 to 1000 and choosing the minimum number of trees to reach convergence.

CNN classification: We train a modified version of the 3D CNN presented in [119], known as *DeepMedic*. The model we employ consists of 8 convolutional layers followed by a classification layer. All hidden layers use 3^3-sized kernels, which leads to a model with a 17^3-sized receptive field. In this task, where the ROI is smaller than for brain cases ($80x80x83$ voxels), processing around each voxel is deemed enough for its classification and thus, the multi-resolution approach of the original work is not used. We reduced the number of Feature Maps (FM) in comparison to the original model $\{15,15,20,20,25,25,30,30\}$ at each hidden layer respectively, not only to mitigate the risk of overfitting given the small dataset, but also to the reduce the computation burden.

To enhance the generalization of the CNN, we augment the training data with reflections over the x, y and z axis. We use *dropout* [126] with 50% rate at the final layer, which counters overfitting by disallowing feature co-adaption. Finally, we utilize *Batch normalization* [127], which accelerates training's convergence and also relates the activation of neurons across a whole batch, regularizing the model's learnt representation. The rest of *DeepMedic* parameters were kept similar to the original configuration [119], as preliminary experimentation showed satisfactory behavior of the system.

Smoothness prior and refinement

Following the mathematical model in Eq. 3.3, we are interested in having a smoothness prior that favors pairs of labels that are deemed *similar* to one another. In our case, we estimate the similarity intensity values from both T1w and T2w with a parametric model of the form

$$P(Y_i, Y_j) = \alpha \cdot e^{-\frac{1}{2\sigma^2_{T_1}}(T_1^i - T_1^j)^2} + (1-\alpha) \cdot e^{-\frac{1}{2\sigma^2_{T_2}}(T_2^i - T_2^j)^2}, \tag{3.4}$$

where T_1^i is the intensity value at voxel i of the T1w VIBE volume (and similarly for T_2^i), $\alpha \in (0,1)$ is a bias term between T1w and T2w importance and where $(\sigma^2_{T_1}, \sigma^2_{T_2})$ are the voxel intensity variances of tumor locations in T_1 and T_2.

3.3 Results

3.3.1 Contribution of Pathological Eye Model

We performed a leave-one-out cross validation experiment on the presented *Pathological Model* (PM). We compare its accuracy with our previous work [2], a Healthy Model (HM) constructed of 24 healthy eyes. We furthermore tested the performance of combining both

the HM and the PM into a Combined Model (CM) built out of 40 patient eyes (24 healthy and 16 pathological). Table 3.1 reports the DSC accuracy, which measures the volume overlap between our results and the GT, for the three different models (*i.e.* PM, HM and CM) when segmenting healthy tissue on our pathological patient dataset. We observe that the PM outperforms the existing HM on average by a $\approx 4.5\%$ and the CM by a $\approx 3.5\%$ (statistical significance evaluated using a paired t-test showing a $p < 0.05$ for both cases).

	Sclera	**Vitreous Humor**	**Lens**	**Average**
PM (%)	**94.62±1.9**	**94.52±2.36**	**85.67±4.68**	**91.51±1.49***
HM - [2] (%)	92.27±4.13	91.62±4.42	76.97±20.28	86.95±9.24
CM (%)	92.45±2.99	91.85±3.07	79.22±14.08	87.84±6.38

Table 3.1 – **Eye Anatomy DSC :** Our Pathological Model (PM) shows more accurate results than the Healthy Model (HM) from [2] and the Combined Model (CM), especially for the region of the lens. $(*)$ $p < 0.05$.

3.3.2 Contribution of EPSF for tumor segmentation

We evaluated the tumor segmentation performances of our strategy when using a RF and a CNN for the MRF likelihood model. In both cases, we tested the performance of $\mathbf{f}^{\mathbf{STD}}$ features only and combined $\mathbf{f}^{\mathbf{STD},\mathbf{EPSF}}$ features as well. For each scenario we optimized θ using cross validation, giving values of $\theta = 0$ mm for RF-STD and $\theta = 2$ mm otherwise. Fig. 3.4-a) indicates the relevant contribution of EPSF, even when trained on very small amounts of data for the RF classifier. Here we see EPSF provides more robustness towards improving the classifier's ability to generalize when trained with limited amounts of data. Fig. 3.4-b) illustrates the ROC performance of the likelihood models and the different feature combinations. In particular, we see that regardless of the classifier used, EPSF provide added performance in the likelihood model. Similarly, improved segmentation performances are attained with EPSF once inference of the MRF is performed, as depicted in Fig. 3.4-c). Optimal parameters for the smoothness term are $\alpha = 0.3,\ \lambda = 0.7$ for RF and $\alpha = 0.4,\ \lambda = 0.5$ for CNN. Table 3.2 illustrates this point more precisely by showing the average DSC and Hausdorff Distance (HD) scores before and after MRF inference is performed and with different combinations of classifiers and features.

	RF+EPSF	RF+STD	CNN+EPSF	CNN+STD
DSC [%]	36.16±27.85	24.49±22.25	56.87±29.38	53.67±24.29
DSC (GC) [%]	**58.50±32.07**	46.15±34.88	**62.25±26.27**	57.64±28.35
HD (GC) [mm]	**0.641±0.884**	3.414±3.874	**0.175±0.062**	0.266±0.172
Training time [min]	**2.36** ⋄	2.21 ⋄	**150** †	150 †

Table 3.2 – **DSC performance :** DSC for different scenarios before and after graph-cut (GC) inference. Hausdorff Distance (HD) after GC inference. Experiments were computed on ⋄: Macbook Pro Intel-Core™ i7 16GB - 2,5 GHZ & †: Intel-Core™ i7 6700 32GB with Nvidia GTX Titan X®.

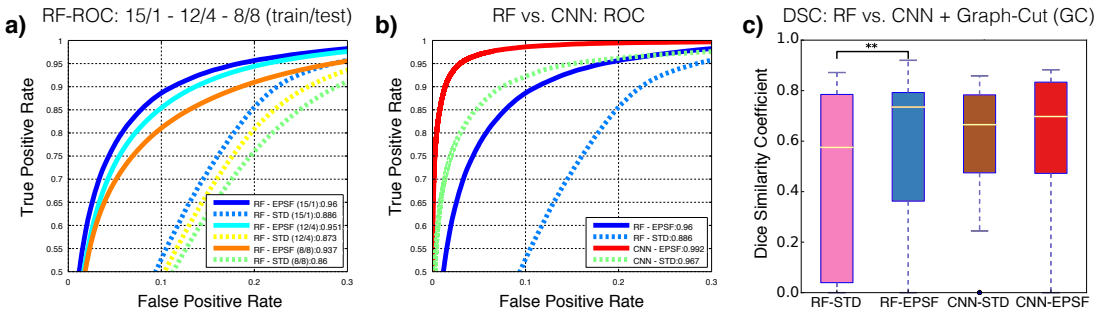

Figure 3.4 – **Classification performance**. (a) ROC curve depicting the effect of varying amounts of (training/test) data for RF classification with and without EPSF. (b) ROC curve for both experiments (CNN / RF) with STD and with EPSF. (c) DSC tumor segmentation results for STD vs. EPSF. The latter shows better results for both cases ($** = p < 0.01$).

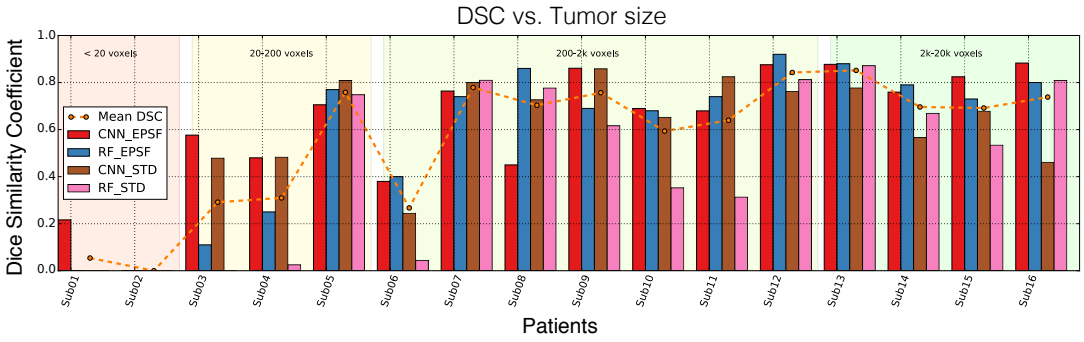

Figure 3.5 – **DSC vs. Tumor size**. Average results for different combination of classifiers and feature sets. EPSF improves overall classification results over STD features consistently.

In Fig. 3.5, we show the DSC performance of the different features and classifiers as a function of tumor size for each patient in the dataset. Note that despite ocular tumors being smaller than brain tumors, DSC values are in line with those obtained for brain tumor segmentation tasks [120]. This illustrates the good performance of our strategy even though DSC is negatively biased for small structures. Except for the two smallest tumors in our dataset (< 20 voxels), DSC scores attained are good, with a HD under the MRI volume's resolution threshold for CNNs. Our quantitative assessment is supported by the visual inspection of the results (see Fig 3.6).

3.4 Discussion

This work introduces a multi-sequence MRI-based eye and tumor segmentation framework. To the best of our knowledge, this is the first attempt towards performing qualitative eye tumor delineation in 3D MRI. We have presented a PM of the eye that encodes information of tumor occurrence as part of the ASM for various eye regions. Introducing pathological information results in a more robust model (with a significantly lower standard deviation), able to improve segmentation for the regions of the sclera, the cornea, the vitreous humor

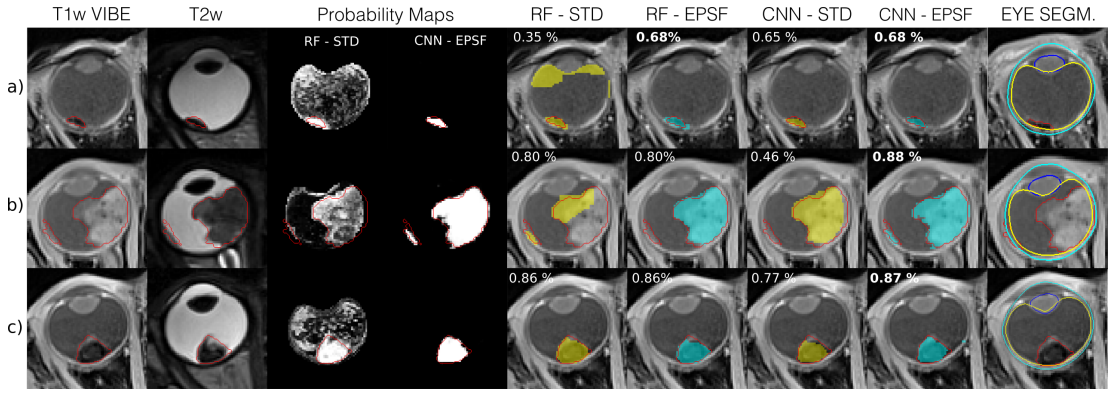

Figure 3.6 – **Example segmentation results**. The tumor ground truth is delineated in red. Probability Maps, $P(\mathbf{f}_i|Y_i)$, for worst (RF-STD) and best (CNN-EPSF) scenarios. Final column shows the pathological model (PM) eye segmentation results.

and the lens. The delineation is followed by a binary masking θ, where the complexity of the tumor segmentation problem is reduced to the eyeball region, and is upper bounded by the maximum euclidean distance error during segmentation. Despite the simplicity of the masking, the gain in performance is significant for all the tested classifiers.

From a clinical perspective, we have presented a new tool for a) measuring the eye tumor size, a task which is now only performed qualitatively in 3D MRI, b) ocular tumor follow-ups, by providing a qualitative estimation of cancer volume variations to enable tracking of the effectiveness of treatment (*e.g* tumor shrinking over time, ...) as well as c) a new approach to study cancer recurrence. Note that recurrence appears often for calcified retinoblastoma tumors [37], developing under the visible area a clinician would observe during Fundus and US, thus making MRI the sole option to detect recurrent tumors under calcified tissue inside the eye.

Moreover, when it comes to evaluating the quality of the segmentation, there is a remarkable difference between the delineation of small (< 20 voxels) and big ($> 2k$ voxels) pathologies. Compact retinoblastomas can be up to four orders of magnitude smaller than such cases. This variation poses a challenge for the presented framework and highly influences the final volume overlap, measured in the form of DSC. To provide a more reasonable measure of the quality of the delineation, we opted for the Hausdorff Distance (HD), a widely spread method in medical imaging to measure segmentation based on distance to the surface GT. Having a look at both DSC and HD, we clearly notice that despite the DSC of the RF with EPSF being larger than the CNN with STD features, the latter offers a more robust segmentation[1]. In the future, the presented work should be evaluated with a larger dataset where more samples with tumors from varying sizes are investigated. Also, tumors with similar imaging conditions, such as uveal melanoma, would be good candidates for performing the evaluation. Furthermore, and in order to potentiate the use of the presented tool, we will offer a functional copy of

[1] Supplementary material includes extended results for DSC.

the pipeline alongside a minimal dataset for segmenting ocular tumors in the eye in 3D MRI online[2] .

One of the most important constraints of current eye MR imaging in ophthalmology are the limitation in terms of resolution, the scanning time, and the difficulty to disentangle small tumors from the choroid, towards both the inside (endophytic) and the outside of the eyes (exopythic). To compensate for this, multiple image modalities (*e.g.* US, CT, Fundus) are evaluated in order to decide about the best treatment strategy. Among the current challenges to improve this decisive step, one of the most relevant is to find a way to connect multiple image modalities in a robust manner. That is, connecting image modalities at different scales (MRI, Fundus, OCT or US) and use common anatomical landmarks to validate the multi-modal fusion. This contribution would not only imply refining the quality of the delineation and treatment based on MRI (such as the framework presented in this manuscript) and other medical image sequences, but it would also support clinicians during the process of decision making, evaluation of tumor extent and patient follow-up, enabling co-working clinical specialists from various backgrounds and modality preferences into the same common perspective.

3.5 Conclusion

We introduced a framework for multi-sequence whole eye segmentation and tumor delineation in MRI. We leveraged the use of pathological priors by means of an ASM and introduced a new set of features (EPSF) that characterize shape, position and tumor likelihood. When combined with traditional features, EPSF are robust and effective at segmenting pathological tissue, particularly when tumors are small. Our approach shows comparable DSC and HD performances to state-of-the-art brain tumor segmentation even when limited amounts of data are available. Both RF and CNN show improved results with our features, while the former performs almost as equally as the latter and is trained in a fraction of the time.

[2]Available at http://www.unil.ch/mial/home/menuguid/software.html

4

Improving multimodal eye tumor analysis by fusion of MRI and Fundus Image Photography

This chapter presents a novel registration method in order to tackle the fusion of pathological MRI and Fundus Image Photography, towards providing clinicians with a simultaneous evaluation tool for ocular tumors accross modalities. We first provide an overview of the related work in the field [94], and continue with a deeper coverage of the techniques required to achieve multi-modal fusion of MRI and Fundus [2, 22].

The work developed in this chapter is in preparation to be submitted as: C. Ciller, S. I. De Zanet, P. Maeder, A. Pica, F. L. Munier, J-P. Thiran, R. Sznitman and M. B. Cuadra **"Topographic Fundus Mapping: Improving multimodal eye tumor analysis by fusion of MRI and Fundus Image Photography"**, to the journal **IEEE Transactions on Medical Imaging**.

4.1 Introduction

Retinoblastoma and uveal melanoma are typically diagnosed with 2D Fundus and 2D US [33], occasionally showing an intra-ocular tumor invasion of the eye. However, confirmation of tumor extent and diagnosis before treatment often requires patients to undergo structural imaging modalities to look for calcifications and second recurrent malignancies (CT or MRI), being the former more invasive than the latter due to ionizing radiation and less recommended for such a task [14, 37], and the evaluation of all these information sources simultaneously by multiple experts (e.g. ophthalmologist, oncologist and radiologist).

General methods for deciding the treatment strategy are based on the evaluation of the tumor size and location. Big tumors occupying most of the VH cavity may suggest more aggressive

procedures, such as enucleation. However, smaller tumors ($< 6mm$) may allow for more conservative approaches where the eye can be treated with minimally invasive techniques. In this category we would find brachytherapy, intra-arterial chemotherapy or intravenous chemoreduction [33, 36, 43]. For the particular case of retinoblastoma, a high percentage is initially treated with intra-arterial chemotherapy, moving towards other techniques in case the first treatment strategies do not evolve as desired. In this context, characterizing the tumor with accurate measures of the size would pose a significant step towards better decision making before treatment. Current techniques based on Fundus and US show good results as first screening of the disease, and they continue to be relevant for consecutive follow ups, however, they may fail to offer a broader picture about second recurrent malignancies, or even to evaluate the extent of the pathology at 3-dimensional level, a field where 3D MRI is salient [37].

In the past years, 3D MRI has gained interest for imaging of eye tumors due to its remarkable soft tissue intensity contrast and its resolution [39], to the point of being the image modality of preference for intravenous chemoreduction (intravitreal needles) or proton beam therapy planning [33]. Nonetheless, Fundus exploration and evaluation remains the key step during treatment, as it provides micrometric information of the tumor extent. Small structures, such as the optic disc, the macula and the location of small tumors, can sometimes only be detected via Fundus and are critical for proper patient treatment planning and follow-up. Needless to say, having a reliable way to fuse multiple image modalities (e.g. MRI and Fundus) would provide clinicians with the missing part of information in the same evaluating context, easing collaboration between experts before eye treatment and thus, supporting therapy [94].

4.2 Related work

4.2.1 Fundus Photography and Fusion

In Fundus imaging, detection and segmentation of retinal anatomical regions are key for evaluating eye diseases (e.g. Glaucoma, Diabetic Retinopathy or AMD) [11]. In the last decade, an intense effort has been devoted towards automatizing the process of segmentation, showing a great success in early detection of eye diseases. However, these techniques for optic disc and fovea segmentation rely on the analysis of Fundus images where both landmarks are still visible [128, 129]. In pathological Fundus images it is often the case that landmarks are occluded by the growing tumor inside the eye, thus preventing their detection (see Fig. 4.1-D).

In a different narrow category within the field of eye imaging we would find fusion of Fundus and MRI. The first attempt to ever connect them was presented by De Zanet et al. [94], with whom we proposed a method to combine healthy MRI and Fundus by using common anatomical landmarks. His approach introduced a new method for landmark detection based on FRST and landmark circularity to combine both modalities. Despite the success of the fusion at a qualitative level, we were unable to fully validate the proposed technique, and

only assessed the fusion in a small subset of healthy patients, leaving the door open to more sophisticated fusion schemes where additional landmarks (such as the tumor itself) could be used to extract quantitative results.

4.2.2 Eye structure segmentation in 3D MRI

To date, efforts for manual delineation of the eye tumor and structures in MRI would require hours of tedious labeling by experts, regardless of the tumor shape and size (Fig. 4.1 A-C). As such, there exists a particular interest for automating this process and to provide a consistent and accurate tumor segmentation specific to the patient.

Current techniques for eye segmentation in the MRI consider the use of parametric models to segment eye structures (e.g. eye lens and vitreous humor) but assume the eyeball to be close to spherical. Among the most extended methods we have OCTOPUS [49], which relies on CT imaging to semi-automatically segment ocular regions with an elliptical model. Most of these techniques allow a coarse segmentation of different eye parts and play an important role in tumor treatment for uveal melanoma [42], however, they are tedious and prone to user-specific errors. More recently, ASM [66, 67] have been used to more precisely delineate these same eye regions using T1w VIBE MR images [2] and CT [99]. Unfortunately, these techniques only address the eye segmentation problem in volumetric image data, and none explicitly tackles the segmentation of malignant tissue. Only the recent work in [22] seeks eye tumor segmentation with a reduced 16-patient dataset.

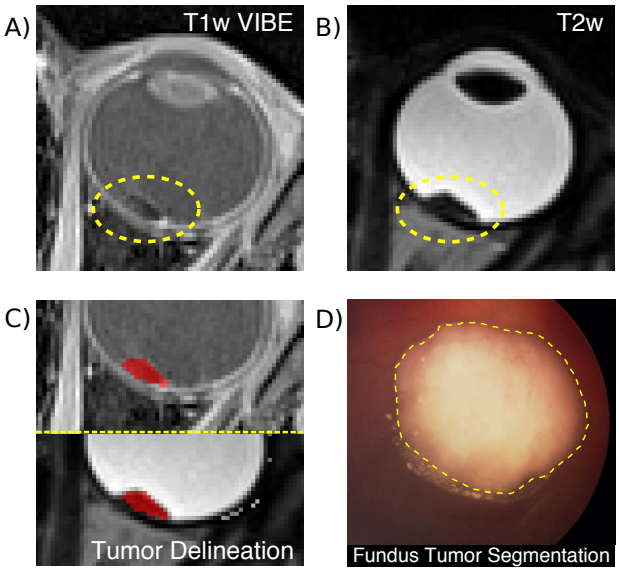

Figure 4.1 – **Multi-modal Imaging of Retinoblastomas** (A)-(B) Detail of 3D T1w VIBE & T2w MRI (C) Delineation of eye tumor in both MRI sequences (D) Fundus of the eye and retinoblastoma manual segmentation (dotted line).

In this chapter, we introduce a method to combine the automatic eye tumor segmentation framework presented in Chapter 3, capable of delineating healthy and pathological structures in the MRI and manually segmented Fundus images, and use common anatomical landmarks and regions to fuse the two image modalities. The method is described as a combination of a PEM, that enables the automatic segmentation of different regions of the eyes (e.g. lens, sclera, cornea, vitreous humor), followed by a classification step where pathological areas inside the eye in the 3D MRI are identified. To carry out the tumor segmentation in the MRI, we utilize the EPSF presented in [22], derived from the PEM, that provide a rich characterization of the pathological tissue, even when small training data is available.

4.3 Methods

Here we describe the method to delineate ocular tumors and structures using a PEM for multi-sequence 3D MRI segmentation, then the automatic segmentation of retinoblastoma in Fundus. Finally, the last part explains the fusion of both image modalities and the benefits of the landmark-based registration to combine Fundus and MRI.

4.3.1 Segmentation of Eye structures and tumor in MRI

The MRI volumes are first pre-processed in the same fashion as in Chapter 3. That is, by automatically aligning both the T1w VIBE and T2w using a rigid translation and rotation, followed by a cropping of the VOI corresponding to the pathological eye [94]. In this process, the center of the VH, the center of the lens and the optic nerve location are found. We then equalize all images for both sequences using the techniques explained in [110] and prepare the volumes for the automatic segmentation of eye structures and tumor [22]. A complete overview of the pipeline presented in this section can be seen in Fig. 4.2.

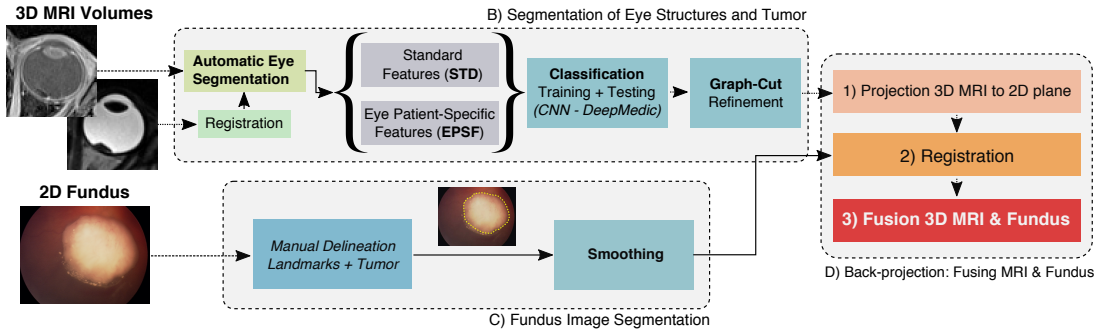

Figure 4.2 – **Multi-modal fusion framework:** Image features extracted from T1w and T2w MRI volumes are combined with EPSF and STD features that integrate Vitreous Humor (VH), eye lens shape and position information, as well as likelihood of tumor locations. These features are used to train a classifier (CNN *DeepMedic*) and are later refined, in a similar fashion as the Fundus classifier. A-C) summarizes the steps to perform the fusion.

CNN Classification: the likelihood prior provides the probability P for every voxel i within the VOI to belong to either healthy or pathological tissue $Y_i = \{0,1\}$. In this work, we leverage a 3D CNN presented in [119], known as *DeepMedic*, to train an 11-layer deep network for performing classification. The input considers 9 different channels, including the two acquired sequences T1w VIBE and T2w, the A-T1w, the average 6 nearest neighbors of the T1w, T2w and A-T1w, and the EPSF, namely, the lens distance map and the VH distance map, which were obtained during the automatic segmentation of the eye, and the pathological patient likelihood prior, in the form of $\mathbf{f}_i^t = \frac{1}{N}\sum_{n_1}^{N} Y_i$, where N is the total number of volumes in the training set (in this case, 32). The configuration is a state-of-the art CNN consisting on a combination of eight 3^3-sized kernels, with three fully connected layers at the end, leveraging training data augmentations with reflections over the x, y and z axis. It uses *dropout* [126] with 50% rate at the final layer, *Batch normalization* [127], which accelerates training's convergence and is also related to the activation of neurons across a whole batch. The rest of the parameters were kept equal to the original configuration [119].

Refinement: we want to support similarity between neighboring pixels for the T1w and T2w, therefore we model the smoothness prior as

$$P(Y_i, Y_j) = \alpha \cdot e^{-\frac{1}{2\sigma_{T_1}^2}(T_1^i - T_1^j)^2} + (1-\alpha)\cdot e^{-\frac{1}{2\sigma_{T_2}^2}(T_2^i - T_2^j)^2}, \tag{4.1}$$

where T_1^i is the intensity value at voxel i of the T1w VIBE volume (and similarly for T_2^i), $\alpha \in (0,1)$ is a bias term to model balance between T1w and T2w and $(\sigma_{T_1}^2, \sigma_{T_2}^2)$ are the voxel intensity variances of tumor locations in T_1 and T_2.

4.3.2 Fundus Image Segmentation

The manual segmentation of Fundus contains the delineation of the retinoblastoma tumor shape as well as the the position of the optic disc, a bright circular shape of approximately $2mm$ that indicates the connection of the retina with the optic nerve towards the brain. This information is required for fusing both images image modalities, as will be shown in section 4.3.3.

In this work we will rely on the manual delineation of the retinoblastoma and the center of the optic disc, a task that can be achieved in a few seconds when performed by an expert ophthalmologist.

4.3.3 Back-projection: Fusing MRI and Fundus

The automatic multi-modal fusion of the Fundus image and the MRI is performed once tumor segmentation is finished for all image modalities. From the MRI we obtain the CNN automatic segmentation of the retinoblastoma as $\cup \hat{Y}_{i,k} = 1 \in X_k$, as well as the position of the optic disc (p_{OD-MRI_k}), the lens center (p_{LC-MRI_k}) and the cornea peak (p_{CP-MRI_k}). A set of landmarks that were obtained by combining the process described in section 4.3.1 using the FRST, and

the prior knowledge about the 3D eye anatomy for all $k = \{1, .., N\}$ patients.

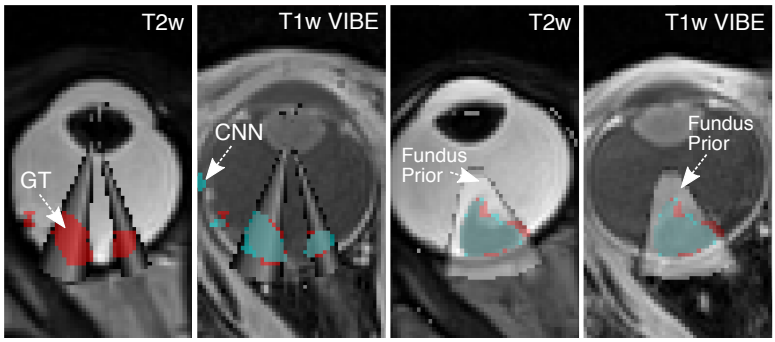

Figure 4.3 – **Fundus Probability Prior Map:** Two examples of the *Fundus Prior* probability map obtained in section 5.2. The light blue areas are the result of the automatic segmentation in the 3D MRI. The cones do not always represent the whole tumor area as the Fundus camera field of view is rather limited.

From the Fundus image F_k, we obtain the location of the optic disc ($p_{OD-Fundus_k}$), whenever the tumor is not covering the area of interest, and the retinoblastoma tumor shape, either manual or automatically segmented as $\cup \hat{Y}_{j,k} = 1 \in F_k$, at every particular pixel j. At this point, registration of the Fundus to the tumor and retina surface in the MRI is performed in three consecutive steps: First, we project the 3D tumor MRI shape obtained as described in section 4.3.1 into a 2D plane, second, we use the location of the optic disc and the tumor shape to register both images using ICP and finally we connect the information across modalities, exporting the benefits of 3D MRI to the Fundus and vice versa. An overview of the whole process can be observed in Fig. 4.4.

Projection of 3D MRI into a 2D plane

Let X_k represent the MRI volume for patient k, we then compute the normalized optical axis vector,

$$\hat{v}_{n-OA_k} = \frac{p_{CP-MRI_k} - p_{LC-MRI_k}}{\left\| p_{CP-MRI_k} - p_{LC-MRI_k} \right\|}, \tag{4.2}$$

from there, we define the camera position,

$$p_{cam_k} = p_{LC-MRI_k} + \hat{v}_{n-OA_k} * d_{L-MRI_k}, \tag{4.3}$$

as the central point from where the 2D plane, Q_k, is to be constructed, and $d_{L-MRI} = 70mm$ is an arbitrary distance from the cornea peak equal to all patients. From here, we extract n_{x_k} and n_{y_k} as the cross product of $\hat{v}_{n-OA_k}$, providing the angles to define the 2D camera plane. Now, let F_{MRI_k} define a 2D virtual projection with size $x_{F_{MRI_k}} = [-120, 120]$ and $y_{F_{MRI_k}} = [-120, 120]$ and map its coordinates in the 2D camera plane,

$$Q_{cam_k} = F_{MRI_k} * [n_{x_k}, n_{y_k}] + p_{cam_k}, \tag{4.4}$$

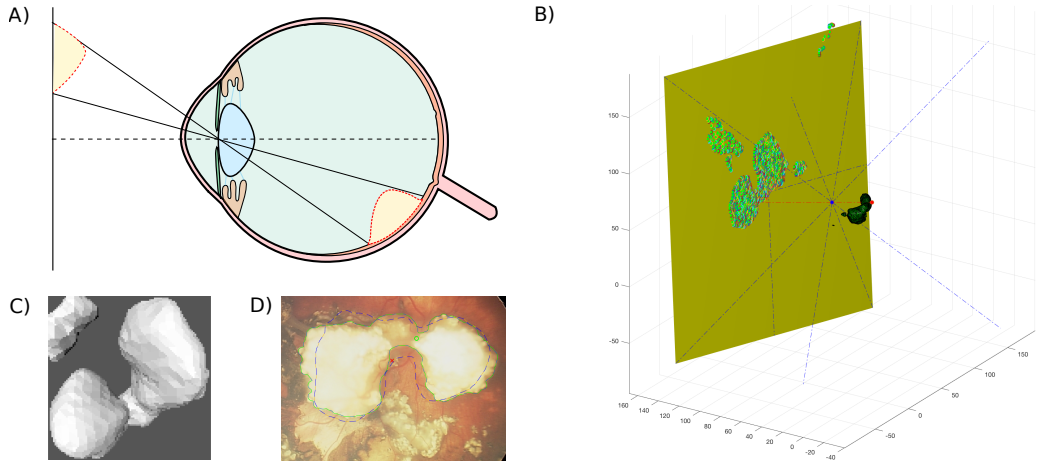

Figure 4.4 – **Back-projection pipeline:** A) Projection of the segmented tumor on the virtual plane F_{MRI}. B) 3D representation of the projection for every voxel i onto the surface represented by the plane F_{MRI}. The red-stripped line represents the projection of the OD. The green points represent the projection of the remaining voxels. C) Reconstruction of the tumor shape prior to back-projection. Every vertex is mapped onto the plane represented in B). D) Results after rigid ICP registration. Green-dashed line: Retinoblastoma Fundus Segmentation GT, blue-dashed line: MRI CNN segmentation results after applying scaling factor g_k.

Furthermore, we extract the 3D surface representing the tumor that we segmented in section 4.3.1 using the marching cubes algorithm [108], and obtain the vertex that conform the tumor shape. At this point, we project each of the vertices $p_{i,k}$ into Q_{cam_k}, by first obtaining the vector that maps the vertex into the plane (Eq. 4.5) and the point $p_{Q_{i,k}}$ (Eq. 4.6),

$$v_{p_{i,k}} = p_{i,k} - p_{LC-MRI_k}, \tag{4.5}$$

$$p_{Q_{i,k}} = \frac{p_{cam_k} - (p_{LC-MRI_k} \times \hat{v}_{n-OA_k})}{v_{p_{i,k}} \times \hat{v}_{n-OA_k}} * v_{p_{i,k}} + p_{LC-MRI_k} \tag{4.6}$$

Once the projection is achieved for all $p_{Q_{i,k}}$ and volumes, we connect them by using a Delaunay triangulation [130] and extract the external perimeter of the shape, thus outlining the final tumor shape in the projected F_{MRI_k}. This shape is to be registered to the original Fundus in the next section 4.3.3 and is represented in Fig. 4.4-C).

Registration with ICP

We process the two different shapes. The original Fundus, F_k, and the F_{MRI_k}. To this goal, we first flip over the x and y axis the F_{MRI_k}, as to compensate for the pin-hole back-projection effect we induced in the previous Section 4.3.3. Furthermore, we smooth the curvature of the tumor shape, applying a gaussian smoothing of $\sigma = 3$, and compensate for the difference in area applying a multiplication factor $g_k = \sqrt{\frac{a_{F_k}}{a_{F_{MRI_k}}}}$, where a_{F_k} and $a_{F_{MRI_k}}$ correspond to the

area covered by the tumor region in both image modalities. We wish to simplify the problem based on the assumption that the two shapes should be deemed similar to one another. Then, we use ICP, as presented in [131] in order to co-register both image modalities and we store the matrix transformation M_{MRI} as well as the translation T_{MRI},

$$F_k \approx ICP(g_k * F_{MRI_k}), \tag{4.7}$$

$$F_k \approx M_{MRI_k} * (g_k * F_{MRI_k}) + T_{MRI_k}, \tag{4.8}$$

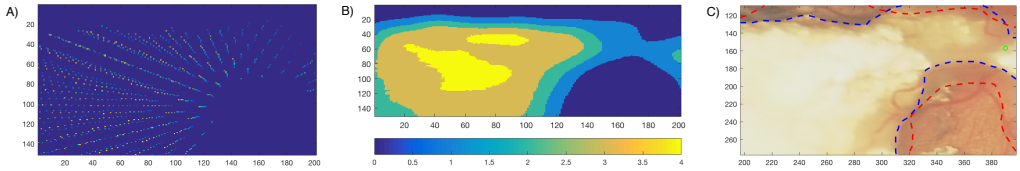

Figure 4.5 – **MRI projection into Fundus:** A) Back-projection of a voxel subset from the MRI volume X. These points follow the projection and registration process and are mapped within the area delineated by the Fundus segmentation. B) Gaussian smoothing and f_i rounding for easier representation of the tumor shape. C) Detail of the superposition of the Fundusretinoblastoma GT (blue dashed) and the projection of the automatic MRI tumor segmentation.

Connecting MRI and Fundus segmentation

Once the mapping that connects a voxel $i \in Y_i = \{1\}$ in the volume X_k with its location in $F_{i,k}$ is defined, we can now write the transformation as

$$F_k = M_{MRI_k} * (g_k * \sum_i p_{Q_{i,k}}) + T_{MRI_k}, \quad i = \{1, ..., s\} \tag{4.9}$$

and use it to evaluate whether $\cup \hat{Y}_i = 1$ is present inside the tumor shape in the Fundus image F_k, or, else, it is outside the shape. That is, we use this information to evaluate whether a voxel j would be mapped inside the 2D Fundus and was, indeed, labeled as $Y_j = 0$ during the CNN segmentation in the MRI. This offers a new method for evaluating the performance of the segmentation based on the alternate connected image modality.

4.4 Results

4.4.1 Evaluating the fusion of MRI and Fundus Image Photography

For validating the fusion between Fundus and MRI we use the DSC between the segmented retinoblastoma on the Fundus as compared to the adjusted projection from the MRI, for both the 3D MRI CNN and the GT.

The results of the DSC for the projection of the 3D MRI CNN segmentation as compared to the manual segmentation performed by an expert reached $87.95 \pm 6.98\%$. When compared to the GT, we reached a total $89.56 \pm 4.98\%$. These results indicate that even for the best possible fitting, offered by the manual segmentation of both images modalities, the results would not surpass $\approx 90\%$ DSC.

4.5 Conclusion

We have presented a method for the multimodal fusion of MRI and Fundus for images from pathological patients. Our method considers using common anatomical landmarks present in both image modalities (such as the optic disc and the tumor itself) in order to perform this task. The fusion relies on the accurate segmentation of MRI and Fundus prior to the presented landmark-based registration using ICP.

Unlike other methods, such as intensity-based techniques for image registration using mutual information [132, 133], we focus on fitting the two groups of landmarks not only because the tumor intensity would be very similar to that of the surrounding voxels representing the sclera and the choroid, but also because MRI may contain artefacts and/or noise that could affect the final registration results. Furthermore, the difference in scale due to the optics of the Fundus camera would also pose an added level of complexity to the problem. In the next chapter we propose two different applications for the fusion and evaluate the quality of the method, toward improving multimodal eye tumor analysis.

5

Fusion of MRI and Fundus Image Photography : Applications for treatment of ocular tumors

The previous chapter established the foundations for the multimodal fusion of MRI and Fundus. In this chapter we will focus our efforts on retinoblastoma, the most common ocular tumor in children [37]. Here, we present two different applications for the fusion and evaluate the quality of the results. First, we introduce a (i) method for improving the quality of the delineation of the 3D MRI based on the back-projection of 2D Fundus, in a process that we call *Fundus Prior* and second, (ii) we propose a method for transfering the 3D rich information from the MRI tumor segmentation to the 2D Fundus image in the form *Topographic Fundus Maps*.

5.1 Dataset

The dataset used in this work includes two different image modalities, 3D MRI and Fundus retinal photography. The MRI dataset is formed by 32 pathological 3D volumes of patients with endophytic retinoblastoma. The volumes represent a section of the head of the patient, including both eyes and the optic nerve. MRI was performed in a 3T Siemens Verio (Siemens, Erlangen, Germany), with a surface head coil of 32 channels. The images are gadolinium enhanced T1w VIBE (repetition time/echo time, 20/3.91 ms; flip angle, 12°) acquired at three different spatial resolutions:$0.416 \times 0.416 \times 0.399 mm^3$, $0.480 \times 0.480 \times 0.499 mm^3$ and $0.30 \times 0.30 \times 0.31 mm^3$ and T2w (repetition time/echo time, 1000/131 ms; flip angle, 120°) with a resolution of $0.453 \times 0.453 \times 0.459 mm^3$ of and $0.27 \times 0.27 \times 0.31 mm^3$. Acquisition of the MRI volumes was done under general anesthesia.

Fundus sequences have been acquired using a RetCam (Clarity Medical Systems, Pleasanton (CA), United States), a camera with interchangeable frontal lens that is applied directly on the cornea of the anesthetized patients and is specific for pediatric retina.

All patient information in our study was anonymized and de-identified by physicians prior to our analysis, and the study was approved by the Cantonal Research Ethics Committee of Vaud. For each eye, the tumors were manually delineated by an expert radiologist. We use these manual segmentations as ground truth for quantitative comparisons. The corresponding Fundus image were selected following the criteria of the clinical institution. That is, the Fundus was acquired within 3-7 days before or after the date of the MRI scan, thus ensuring minor to non-existing variations in the size of the tumor. The retinoblastoma and the most relevant landmarks in the Fundus were delineated by an expert ophthalmologist.

5.2 Improving 3D MRI delineation via Fundus Prior

5.2.1 Motivation

Automatic segmentation of ocular tumors on the MRI has been already covered in this thesis in chapters 2 and 3, however, the results of the segmentation often regarded artifacts and healthy areas of the eyes as tumors, both due to MRI noise and to the uncertainty while doing classification. Furthermore, the amount of patients that were used in these experiments was rather low ($\approx$ 32 MRI volumes), eventually reducing the quality of the classification scheme. In a sense, there is a clear room for improvement given a bigger dataset and additional retinoblastoma patient segmentations.

In here, we propose a technique to improve the segmentation results beyond the fine-tuning offered by the graph-cut optimization refinement from section 4.3.1. The use of Fundus images in order to improve the quality of the segmentation results in the MRI. Our hypothesis is that the local accuracy of the submilimetric tissue information from the Fundus tumor segmentation will benefit the delineation on the MRI, removing potential spureous false positives outside the tumor area for small cancers. Section 5.2.2 covers the methods required in order to obtain this *Fundus Prior* information.

5.2.2 Methods

We start once the fusion scheme proposed in chapter 4 is completed. From there, we use the MRI segmentation after the *DeepMedic* CNN classification and the Graph-Cut refinement to generate a probability map, $FP_{i,k}$ from the 3D volume X_k which takes into consideration every voxel i in the volume and is constructed as,

$$FP_{i,k}\begin{cases} HD(F(X_{i,k})), & FP_{i,k} = \in F \cup Y_i \\ 0, & otherwise \end{cases} \tag{5.1}$$

where HD and $F(X_{i,k})$ is the projection of the MRI voxel into the Fundus. Whenever voxel i is mapped inside the Fundus retinoblastoma segmentation, a value of equal to the HD will be assigned to this specific voxel, a value of 0 will be assigned otherwise, as shown in the previous equation 5.1. The final outcome of this process is a 3D map of the tumor, with a rather conic shape, that could be utilized for improving delineation of the cancer in the MRI, removing external misclassified regions within the eyeball. A more detailed graphical explanation can be found in Fig. 4.3. In the section 5.2.3 we further develop a set of experiments to compare delineation results.

5.2.3 Results and conclusion

This section introduces the MRI tumor segmentation results, evaluating the CNN network with and without the contribution of the Fundus Prior.

Contribution of Fundus Prior to the Segmentation of Eye tumors in 3D MRI

We start by evaluating the method presented in section 4.3.1 for 3D MRI tumor segmentation. We use the PEM proposed in [22], trained on 16 pathological eyes, in order to automatically segment the eye ball, including the regions of the sclera, the cornea, the VH and the lens. We then use the EPSF to improve the quality of the tumor classification, as they provide rich spatial and intensity information for the different eye regions in the MRI volume. To conclude, we set up the minimum number of iterations as to reach convergence to 35 epochs. A qualitative evaluation of the results can be seen in Fig. 5.1.

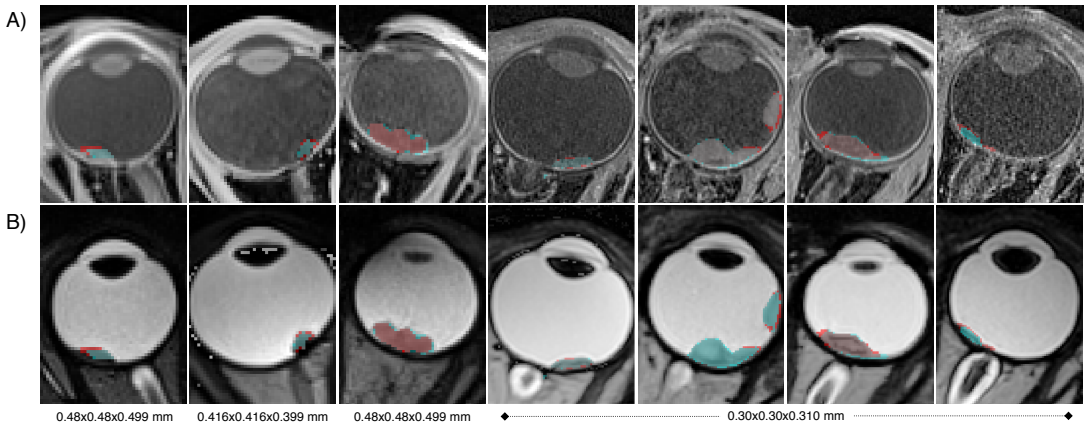

Figure 5.1 – **3D MRI Tumor Segmentation :** A) T1w VIBE and B) T2w segmentation examples for patients with different image resolution, ranging from $\approx 0.5mm$ almost isotropic resolution to $\approx 0.4mm$ and $\approx 0.3mm$. Segmentation results for smaller tumor structures are consistently worse. Minor variations in the segmentation cause a high impact in the DSC.

Once this task is finished, we measure the overlap between the manual delineation and the results of the classification by computing the DSC in a 16-fold cross-validation on the

32 endopythic retinoblastoma MRI volumes (Table 5.1). That is, we train our CNN on 30 patients and test on the remaining 2. Furthermore, we evaluate the contribution of using the back-projection technique from section 5.2, represented in Fig. 4.3.

We post-process the resulting 3D MRI tumor segmentation after GC utilizing the FP as a mask for improving the segmentation of small tumors ($< 1k$ voxels), reducing the misclassification outside the tumor region. The goal is to use the fusion to leverage the micrometric information provided by the Fundus, and to improve the final segmentation results in the MRI (with a resolution in the order of the milimeters). The parameters we defined in order to achieve these results are $\alpha = 0.3$ and $\beta = 0.7$ for the automatic refinement of the 3D MRI classification. Moreover, we test two different setups, *Hard* and *Soft* FP, corresponding to binary or smoothed masking of the tumor region respectively. The Gaussian smoothing for the *Soft* FP is set to $\sigma = 8 voxels$. Table 5.1 contains information from the different configurations and the DSC for every step. The complete list of results can be seen in Fig. 5.2.

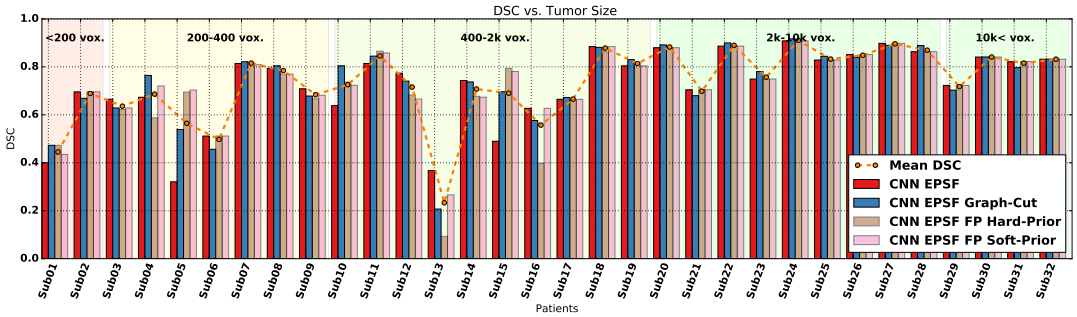

Figure 5.2 – **DSC vs. tumor size :** results for the different techniques applied to the classification output, including: The baseline CNN EPSF, CNN EPSF after GC, CNN EPSF+GC + *Hard* Fundus Prior and CNN EPSF + GC + *Soft* Fundus Prior.

To conclude, we compute an additional experiment. We re-train the *DeepMedic* 3D CNN implementation including the FP as an additional feature map. The goal here is to evaluate the contribution of the FP information during the 3D MRI CNN training. Given that the FP is not always contributing to improve the quality of the segmentation due to the Fundus field of view, we use a uniform probability map as the channel for cases where tumors are $< 1k$ voxels. The results of this experiment can be seen in Table 5.1 [1].

The results show a slight average contribution of the Fundus towards improving the quality of the segmentation results in the MRI. However, the contribution is marginal.

[1] The hardware requiered to achieve these results can be seen in Experiments were computed on ⋄: Macbook Pro Intel-Core™ i7 16GB - 2,5 GHZ & †: Intel-Core™ i7 6700 32GB with Nvidia GTX Titan X®

	MRI CNN	MRI CNN + FP
DSC [%]	72.42±15.82%	70.54±18.51%
DSC (GC) [%]	**73.85±15.64%**	N.A.
DSC (GC) + FP (Hard) [%]	72.54±17.19%	N.A.
DSC (GC) + FP (Soft) [%]	**74.05±14.15%**	N.A.
Training time [min]	621.39±18.48	681.7±4.54

Table 5.1 – **Tumor segmentation before and after FP :** DSC performance for MRI tumor segmentation before and after graph-cut (GC) combining both *Hard* and *Soft* FP. The Hausdorff Distance (HD) after GC and *Soft* FP is also presented.

5.3 Tumor characterization and Topographic Fundus Mapping

5.3.1 Motivation

In addition to the minimal improvements to the automatic segmentation of ocular tumors in either Fundus or MRI, the fusion can be utilized to represent both image modalities in a common reference shape. The goal of *Topographic Fundus Mapping* is to be able to connect and transfer 3D milimetric and 2D micrometric information and knowledge accross modalities and clinical specialists (*e.g.* radiologist, ophthalmologist, ...).

Every clinician has a preferred image modality of choice to evaluate ocular tumors and to decide on the treatment to follow, nevertheless, the information of the *non-preferred* image modalities may bring interesting discussions to the table, such as variations on the final treatment strategy and a better tracking of evolution of the disease during follow-up. Furthermore, the possibility of transferring information from 2D to 3D may allow for new unprecedented ways to confirm the tumor extent faster and better than during single modality evaluation techniques.

5.3.2 Methods

The second application presented in this chapter is to introduce rich 3D tumor shape information into the 2D Fundus after registration. Back-projection, presented in chapter 4, allows MRI to Fundus support during evaluation, with an estimation of the tumor size (in mm^3) as well as a new volumetric characterization of the tumor, overlapped over the Fundus tumor shape, and identified as *Topographic Fundus Mapping (TFM)*. TFM are constructed by leveraging the VH distance map computed during the automatic segmentation of the eye in the MRI (in Section 4.3.1) with the registration scheme proposed in Section 4.3.3.

For every voxel $i \in \cup Y_i$ in the volume X we perform the back-projection $F(X_i)$ and evaluate the presence of the projected voxel within the area delineated by $\cup F_j = 1$, where $\cup F_j = 1$ represents the location of the tumor in the retinal image, a region which is either manually segmented or delineated using the method presented in section 4.3.2. $\cup F(X_i) \in \cup F_j, Y_j = 1$ represents

the sparse distribution of points on the Fundus image. An example of this point cloud can be seen in Fig. 4.5-A). Now, every projected point contains the feature value f_i corresponding to the distance to the surface of the retina, that is, the distance to the segmentation of the VH boundary. From here, we simplify the problem by computing $[\cup F(X_i)]$ and perform a Gaussian smoothing $G(x)$ of $\sigma = 10$, to regularize the region of the tumor (see Fig 4.5-B). We also store the $F_{99.8\%}$ percentile representing the maximum f_i, corresponding to the highest distance, and use these values to restore the original height, H_{orig}, where we define $g_{TFM} = \frac{F_{99.8}\%}{max(G(f_i))}$ to compensate for the difference in scale after the gaussian smoothing.

Finally, in order to be able to retrieve the MRI scaling factor for the TFM, we compute the distance between two points separated 20 voxels in the 3D MRI sagittal plane. The Euclidean distance between both projections on the Fundus image allows for the estimation of the physical scaling factor that connects pixels to measures in mm.

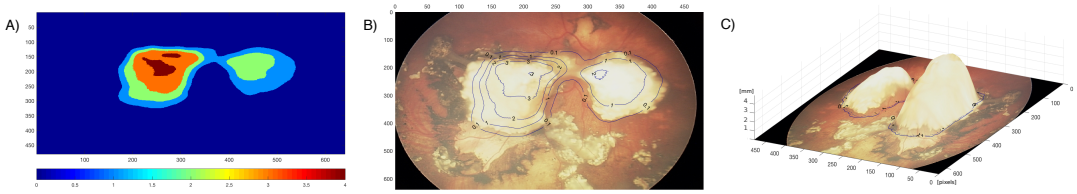

Figure 5.3 – **Topographic Fundus Mapping:** A) Gaussian smoothing of the back-projected point cloud with compensated VH distance information. B) Overlapping TFM curves over Fundus image. The different numbers indicate distance (in mm) from the retinal wall. C) 3D representation by means of texture mapping of the Fundus over the surface defined by the tumor shape.

At this point, we are able to provide topographic and volumetric information of the Fundus image F_k by means of the landmark-based registration proposed in the Section 4.3.3. In Fig. 5.3 we have an example of the resulting TFM and the projection of the Fundus photography over the artificially generated surface.

5.3.3 Results and conclusion

Here we demonstrate that the presented registration technique allows for 3D MRI rich tumor information to be transferred to the Fundus image, opening the door to more complex multi-modal characterization of the tumor in 2D and 3D.

Topographic Fundus Mapping (TFM)

For validating the fusion between Fundus and MRI we use two different techniques. The first one was presented in the previous chapter and consisted on the quantitative DSC evaluation between the segmented retinoblastoma on the Fundus as compared to the adjusted projection

Table 5.2 – **Tumor apex in MRI measured by clinician vs. Distance Map (ASM Segmentation) and Fundus projection apex :** This table indicates the difference between the distance measured by an expert clinician to indicate the tumor apex (required for brachytherapy) and the estimated apex obtained via the ASM and the Fundus back-projection.

	Distance Map (Error) [mm]	**Fundus Projection (Error) [mm]**
Manual Measure -Clinician-	0.523 ± 0.431	0.690 ± 0.547
p-value	1.35e-5	3.53e-3

from the MRI, for both the 3D MRI CNN and the GT, see Section 4.4.1. The second part of the evaluation consists on measuring the quality of the surface representation given by the TFM. To do so, we a) compute the distance between the apex of the tumor to the normal of the retinal wall as compared to the results in the 3D projection and b) perform a qualitative evaluation of the results.

Both a qualitative and quantitative evaluation are conducted for the TFM. A subset of these can be observed in Fig. 5.4. The remainder of this article focuses on the comparison between the i) GT distance measured by a clinician, ii) the *apex* distance manually extracted from the MRI segmentation (VH Distance Map), the and Fundus fusion reconstruction at the 99.8% percentile. Table 5.2 shows the results between all three measures. We can observe that the difference between the two errors is comparable, and statistically significant for both cases, being a little over the resolution threshold.

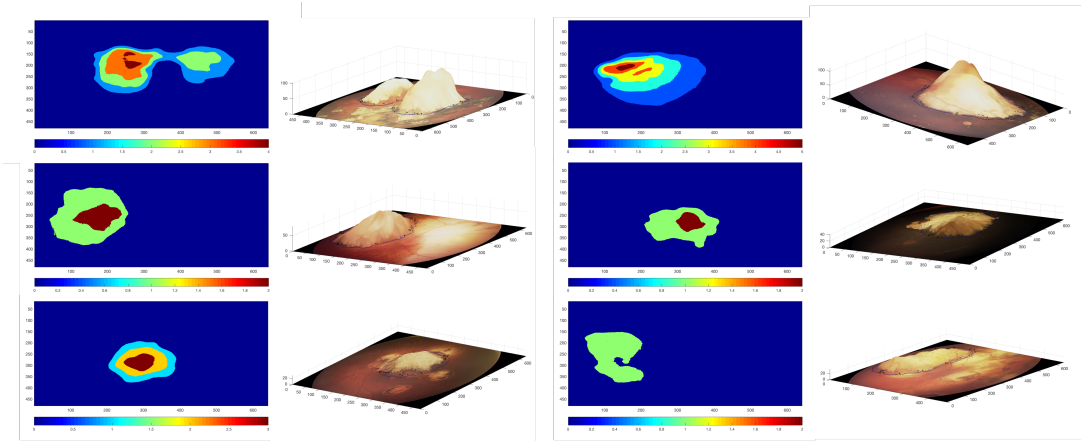

Figure 5.4 – **Evaluation of Topographic Fundus mapping :** A few examples of the multi-modal fusion of Fundus and MRI. We leverage the 3-dimensional information from the MRI in order to give a 3D context to the Fundus. TFMs maps are generated from the point projection on the left side and connected to the Fundus image on the right for 6 patients. These new images have a 3-dimensional shape and navigation allows a better understanding of the disease.

5.4 Discussion

In here, we have introduced a new method for the registration and fusion of 3D MRI and 2D Fundus. The technique leverages the segmentation of retinoblastoma in Fundus by manual means, as well as the automatic segmentation of the eye tumor in the 3D MRI for achieving this goal. This is, to the best of our knowledge, the first attempt to ever fuse such pathological image modalities succesfully. The whole pipeline attempts to segment both image modalities independently to later use common anatomical landmarks, such as the optic disc and the tumor itself, to properly connect the microscopic world representation, obtained via Fundus imaging, with the macroscopic MRI representation.

The clinical implications of this work are unique in its proposition to combine one of the most useful image modality for radiologists (MRI) and the requirements for ophthalmologists (Fundus), towards confirmation of diagnosis and treatment for patients with retinoblastoma. This fusion will pave the way for clinicians to share their evaluation tools in a simultaneous way, contributing to the discussion of results in a common multi-modal ground, where new angles and evidences can be considered. Furthermore, the connection between image modalities will allow for a better follow-up of the disease, where succesive Fundus acquisition could be used to evaluate the impact of a certain treatment on the size of the tumor, without the need of continuous MRI scanning and, thus, reducing operational costs.

From an analysis point of view, interesting are the comparison between the fusion of both image modalities and the difference in tumor shapes. This situation is driven mainly by two factors. The first one is the geometric distortion that appears whenever we evaluate voxels between the AS and the center of the eye whose trajectory differs $< 30°$ to that of the optical axis (as expressed in section 4.3.3). These projections tend to be more distorted than points closer to the posterior part of the eye, where both the optic nerve and OD are located. Furthermore, the difference in scale and resolution between Fundus and MRI also affects negatively to the shape. It is often the case that clinicians may commit delineation mistakes when it comes to evaluate tumors in the MRI, not only because the tumor intensity is very similar to that of the surrounding voxels representing the sclera and the choroid, but also because MRI may contain artefacts and noise. One of the main purposes of the presented work is to *clean* these artifacts and to be able to obtain an accurate representation of the disease, reinforcing its accuracy at local level. Albeit the limitations of geometric distortion during the MRI projection, the fusion represents a clear support for clinicians during the diagnosis evaluation and follow-up of the tumor and, even if there exists minor geometric deformations, longitudinal studies of the same patient would be able to cope with the temporal variation in tumor size and monitor their variation. Moreover, we highlight the contribution of simplifying the image registration process with common anatomical landmarks instead of the usual intensity-based methods combined with mutual information. By doing so, we reduce the computational burden and rely on the quality of the tumor shape rather than on confusing retinal intensities for fitting the new model. The additive problem of a varying scaling factor connecting the MRI and Fundus, combined with a difficulty to distinguish the mussels behind the sclera discouraged

us from performing these experiments. In future work it would be desirable to get a wider representation of the retina region by using Fundus mosaicking, as the combination of images would provide a more complete representation of the eye and the pathologies therein.

With regards to the limitations we encountered while working with the fusion, we may highlight the problems for properly representing massive tumors ($10k <$ voxels) using Fundus imaging. In these cases, tumors grow inside/outside the eyeball and they become a natural barrier to capture the interior part of the eye with retinal cameras, leaving 3D MRI scans as the best option to represent the tumor in its completion. In these particular cases, the treatment tends to be a bit more aggressive and enucleation is often required. The presented work would be more relevant to those small-sized tumors where decision for treatment falls in a grey area between side effects and patient prognosis.

Multi-modal fusion is one of the biggest challenges in ophthalmology and the presented work introduces a key connection for combining Fundus and MRI. The common anatomical landmarks that we find in these modalities will pave the way towards having not only Fundus and MRI data, but also including OCT information during the evaluation of retinoblastoma before treatment. Current devices for acquiring OCT images already incorporate the acquisition of Fundus images, thus, it would be a composition very much in line with the future ocular tumor research. One of the key problems in pediatric oncology research for ocular tumors is the low amount of dataset for proper evaluation of the disease when different treatments are considered. Multi-modality is a solution to leverage the knowledge obtained from multiple information sources, and to better understand the evolution of the disease, towards precision and patient-specific medicine.

6

Conclusion

Summary

In this thesis I have presented an ensemble of image processing techniques to improve current methods for multimodal imaging in ophthalmology, focusing on MRI and later on Fundus imaging to support clinicians during treatment planning and follow-up of ocular tumors.

The first part of the manuscript covered the analysis and representation of the eye at a macro-structural level with the evaluation of the 3D MRI, a technique that was routinely used to investigate the spread of tumor in the optic nerve and/or through the eye wall [3] has slowly transitioned towards the evaluation of the tumor extent via multi-sequence MRI analysis (T1w VIBE and T2w) [39]. Our efforts have focused on the analysis of eye populations and the use of statistical modeling techniques to ease the process of characterizing the eye. To this end, we used *Active Shape Models (ASM)* to model the regions of the sclera, the cornea, the vitreous humor and the lens, and created a framework for the fully automatic segmentation of the eye in the T1w VIBE MRI in children. The accuracy and robustness of the presented scheme for delineating healthy eyes in T1w VIBE allowed for the segmentation, not only of such regions in healthy children eyes, but also the healthy eye structures in pathological patients with retinoblastoma. The complete method and results are introduced in chapter 2.

The results of automatic eye segmentation alone were not sufficient for the proper characterization of ocular tumors in multi-sequence MRI, a long sought goal prior to treatment planning for evaluating the malignancy. The previous work in Chapter 2 served as a method for segmenting healthy regions in pathological MRI, and defined an advantageous starting point for using general purpose machine learning techniques to classify the tumor inside

the eyeball. In Chapter 3, we considered the use of a dataset of pathological patients with tumors to build a new ASM to segment the eye in 3D T1w VIBE. Unlike other methods for brain segmentation, this method utilized pathological patients instead for training the statistical model, achieving better segmentation results (see section 3.3.1). This particular result could be justified by De Graaf et al. [96], who demonstrated that, on average, retinoblastoma eyes were smaller than normal eyes and that there was a negative correlation between tumor growth and eye volume size. Then, we registered the T1w VIBE to the T2w MRI and introduced a set of specific features called Eye Patient-Specific Features (EPSF) to characterize the shape, location and likelihood of the tumor. The outcome of this approach was the improvement of the segmentation of small ocular tumors and the simplification of the classification problem thanks to the rich spatial and intensity information. Furthermore, again we put special attention to the automatization of the whole process, always looking for easy methods to support clinicians in the field of ocular tumor research.

Finally, I would like to close this summary with a contribution that we started in collaboration with De Zanet et al. in [94], a method for the multimodal fusion of MRI and Fundus image photography. At first glance, the reader may notice the significant difference in scale and resolution between both image modalities, and thinking of a proper multimodal fusion is an idea surrounded by numerous challenges. In [94], we estimated the location of the fovea, the optic disc and the optic axis in the Fundus, as well as the automatic segmentation of the vitreous humor of the eye to achieve a multimodal fusion of healthy patient eyes. However, we could not validate the results and we were still far from our goal of using fusion to support the clinician, especially during evalution of the tumor extent and multi-modal confirmation of the malignancy. To this end, this work introduces a new fusion method using common anatomical landmarks and the tumor itself to register both MRI and Fundus in a precise landmark-based fashion with ICP. Chapters 4 and 5 cover the proposed multimodal fusion of Fundus and MRI scheme where a robust regristration is proporsed, able to cope with difference in scale, variations in intensity and orientation between modalities. We furthermore used this new fusion method for (i) improving the MRI segmentation results proposed in Chapter 3 and (ii) provide Fundus image photography with 3D rich information from the MRI, creating a method to transport 3D curvature to the image representing the 2D Fundus. The results presented in Chapter 5 do support the hypothesis that the multimodal patient-specific representation of the tumors will benefit clinicians from different backgrounds with this multimodal tool to evaluate tumors simulatenously in MRI and Fundus during treatment planning and follow-up.

Perspectives and Future developments

In this work we demonstrated that we were able to provide clinicians with a set of image processing tools to support their study and understanding of the pathology, its follow-up and to support the decision treatment process, an asset specially useful when confronted with agressive ocular tumors such as retinoblastoma. The applications that we presented to automatically segment the eye structures and retinoblastoma in the MRI and its fusion with

Fundus Image Photography will pave the way for similar approaches to other tumors such as *uveal melanoma*, the most common eye tumor in adults [45]. Following these lines, we received a project grant for the continuation of this thesis, towards translating these findings to support adults patients with tumors in the uveal region.

Clinical Applications of the presented work. The navigation systems that we proposed with the *EyeModeler software* in Annex B for exploring eye pathologies, and the possibility to use these 3D computerized models for simulating and evaluating the disease will not only support the clinician decision before treatment, but also allows sharing perspectives and thoughts with fellow clinicians simultaneously. Moreover, the techniques that we applied to segment the tumor at subresolution precission in chapter 3 will set the basis to further monitor the evolution of such diseases in the form of longitudinal studies. In this direction, the analysis of such data will shed some light towards refining the treatment strategies based on precise indicators, such as the tumor location, size and even genetic factors. Last but not least, the ability to model the disease combined with the organs wherein it is located would allow for an easy transition towards the field of 3D printing eye patient-specific models for their analysis (specially useful for brachytherapy treatment planning), bringing high precision medicine for retinoblastoma one step closer to the clinician.

Towards alternative image modalities: OCT and US. The ever rising field of OCT imaging has opened the door to deep analysis and detection of ocular pathologies such as DR and AMD in the past [18, 19]. In the field of ocular tumors, though, its use remained limited, and only a few articles in literature partially covered the use OCT as a screening protocol [134, 135]. Possibly, one of the most promising continuations of this work would be the adaptation of the multimodal patient-specific eye model to include OCT image information in the pipeline. This could be easily done via registration of the Fundus acquired during the OCT scanning to the Fundus obtained with the pediatric Retcam. This contribution would finally connect the macrostructural level of information given by the MRI with the microstructural level of detail offered by OCT. Simultaneously, early diagnosis of retinoblastoma and blood flow monitoring would open the door to real-time evaluation of chemotheraphy throughout the eye, or even allow extremely precissed targeted cryotherapy, among many other different challenges that would appear. Also, from a less ambitious point of view, the missing part of this work covering the analysis of 2D and 3D US would also be beneficial for the clinicians, and a very strong contribution to the multimodal patient-specific eye tool presented here. US would bring a reliable non-invasive image modality between Fundus and MRI, not affected by any magnetic field geometric distortion, presenting a trade-off between area of representation and resolution quality. Other techniques presented in literature for 2D/3D US to MRI such as the one presented by Cuadra et al. [98] would be an interesting continuation for this work, and would contribute to better represent the eye accross different image modalities.

Improving current models for delineation of the disease. Another of the limitations that appeared during this thesis was the lack of big amounts of medical data for testing and training, and the scarce annotations for the few we possesed. Retinoblastoma is a rare disease and as such, it requires a strong collaboration with clinical institutions to obtain enough samples as to claim generalization, regardless of the methodological contribution. In this context, future collaborations with other centers or simply by releasing the developed techniques to the scientific community would be an elegant move towards validating further discoveries.

EyeModeler Software. The presented techniques are based on medical imaging methods on a constant evolution, thus, we designed our software in a modular fashion, enabling easy interchangeable methods to be replaced whenever required. Among the future development lines that we would consider as new modules for the EyeModeler software, we would have:

- The use of versatile machine learning techniques, similar to the ones employed in chapters 3 and 4 with deep CNNs to improve the quality of the delineation at multiple stages of the framework (e.g. the ASM building process, the delineation of ocular tumors in both Fundus and MRI, ...).
- The contribution of multiple image modalities, such as stated before with US and OCT for further improving the delineation and characterization of the disease.
- The longitudinal monitoring of the disease, evaluating differences between time points, a especially interesting field of research towards deciding best treatment strategies based on predictions and estimation of the cancer evolution.
- The use of multi-scale multi-sequence MRI for improving the final delineation of ocular tumors in multiple image modalities. The current protocol for ocular tumor imaging tries to account for the difference in resolution by taking multiple images of the same ROI (the eye). In this particular context where multiple volume sequences representing the same area would be available, we could investigate new method for the fusion of multiple sequences towards super-resolution. This would not only improve the quality of the images, but help to better delineate tumors and structures within the eyes.

In summary, the number of possible development lines is diverse and research can be continued in a variety of fields, either at clinical or methodological level. The objective though will remain: to improve the quality of the work developed by clinicians and professionals in healthcare, who will consciously drive this research towards new horizons, sharing their needs and ideas and hopefully, taking benefit from the lines and contributions that came out of this work.

7

List of Publications

7.1 Journals

- **2016 (Pend.)** - **C. Ciller**, S.I. De Zanet, P. Maeder, A. Pica, F.L. Munier, J-P. Thiran, R. Sznitman and M.B. Cuadra *"Topographic Fundus Mapping: Improving multimodal eye tumor analysis by fusion of MRI and Fundus Image Photography"*, IEEE Transactions on Medical Imaging - **Under Preparation**

- **2016 (Pend.)** - **C. Ciller**, S.I. De Zanet, K. Kamnitsas, P. Maeder, B. Glocker, F.L. Munier, D. Rueckert, J-P. Thiran, M.B. Cuadra and R. Sznitman *"Multi-channel MRI segmentation of eye structures and tumors using patient-specific features"*, Plos One Journal - **Under Review**

- **2015** - **C. Ciller**, S.I. De Zanet, M. Rüegsegger, A. Pica, R. Sznitman, J.P. Thiran, P. Maeder, F. L. Munier, J. H. Kowal, M. Bach Cuadra, *"Automatic Segmentation of the Eye in 3D Magnetic Resonance Imaging: A novel Statistical Shape Model for treatment planning of Retinoblastoma"*, International Journal on Radiation Oncology*Biology*Physics, 2015 Jul 15; 92(4):794-802

- **2015** - S. I. De Zanet, **C. Ciller**, T. Rudolph, M. Bach Cuadra, P. Maeder, A. Balmer, F.L. Munier and J.H. Kowal, *"Landmark Detection for Fusion of Fundus and MRI Toward a Patient-Specific Multimodal Eye Model"*, IEEE Transactions on Biomedical Engineering (TBME), Volume 62, Issue 2

7.2 Conferences

- 2014 **C. Ciller**, S.I. De Zanet, A. Pica, J.P. Thiran, P. Maeder, F. L. Munier, J. H. Kowal, M. Bach Cuadra, *"Automatic magnetic resonance imaging segmentation of the eye based on 3D active shape modeling"*, ARVO 2014, Orlando, FLO, US, Submit.: Dec, 2013, Accept.: Feb, 2014 - **Accepted abstract & poster**

- 2014 **C. Ciller**, S.I. De Zanet, A. Pica, J.P. Thiran, P. Maeder, F. L. Munier, J. H. Kowal, M. Bach Cuadra, *"Active Shape Modeling techniques in Ophthalmology: Automatic Segmentation of the eye in magnetic resonance imaging of children"*, Symposium on Statistical Shape Models and Applications, 11-13 June 2014, **Accepted Abstract & Poster** Other: 2nd Best Poster Award

A

Atlas construction – Point-Based Shape Variation Model – Active Shape Model

This annex represents an addendum to the methods developed in chapter 2, further contributing with an extended overview of the Atlas constructions, the PBSVM and the ASM generation.

A.1 Atlas construction

The process to construct the atlas follows the lines of Frangi et al. [105]. However, we introduce several minor modifications to the original method, such as a rigid volume pre-alignment based on landmarks in the eye in the MRI [94], and a non-rigid free diffeomorphic demons registration algorithm [107] to transform the atlas into a Natural Coordinate System (NCS) [105].

We first align every MRI volume to a common reference coordinate system. We apply, to each subject, a rigid pre-alignment using the landmarks from De Zanet et al. [94] based on 3D FRST [136]. The center of the vitreous humor, the center of the lens and the position of the optic disc help us to align all patients into a common reference space. Once the complete dataset is aligned, we check evaluate whetherwe resample all MRI volumes to the image spacing is the desired ($0.416x0.416x0.399mm$) and resample it in case we encounter a different spatial resolution ($0.480x0.480x0.499mm$) Afterwards, we compute a voxel signed distance map of the different labeled regions and fuse them to create the baseline atlas.

To reduce the bias towards a certain shape, we register the baseline atlas against each manually segmented region using a non-rigid free diffeomorphic demons, and apply the transformation to the baseline atlas. This process enables us to combine all the deformation fields together and transform the current baseline atlas into an unbiased NCS atlas.

A.2 Point-Based Shape Variation Model (PBSVM)

Once the atlas in NCS has been built, we extract a surface point cloud for every eye atlas region: sclera + cornea, vitreous humor and lens. To obtain this information, we utilize a mesh extraction algorithm [108]. It is important to highlight that the binary mesh extraction step generally provides us with a non-smoothed point based surface; therefore, to have a proper smoothed point distribution, we require to apply a Gaussian smoothing filter [137]. The number of iterations that we do over each surface is 50, with a band-pass filter of 0.01.

The current point cloud represents a smoothed approximation of the original NCS atlas shape. We apply a decimation to each of the point cloud surfaces [108] and reduce the number of points to a 15% of the original amount for the sclera + cornea and the vitreous humor, and to a 90% of the original amount for the lens. These new set of points will later be used as landmarks to capture the patient variability. An important remark concerning the decimation process is that the algorithm aims at preserving the topology of the surface, therefore, it will preserve important details, such as the point curvature.

Once the surfaces are decimated, we perform a non-rigid free diffeomorphic demons registration between the original volumes and the NCS atlas, and warp the atlas landmark point cloud back to the patients [107]. This process enables us retrieve information about every landmark position in each the patient. The corresponding landmark positions are used to capture the landmark variability, which is later encoded inside the PBSVM through a Principal Component Analysis (PCA)[109]. To perform this process, we start by transforming the point cloud into a tangent space (Eq. A.1), thus preserving the linearity of the shape (Eq. A.1)

$$x_t = \frac{|x|^2}{x * x} \cdot x, \tag{A.1}$$

This approach follows the lines of Cootes et al. [67], where $\bar{x}$ is the original surface points vector, is the mean surface shape and x_t is the new projection of the surface points in the tangent space. We then compute the PCA of the projection, and extract the principal components of the landmark point cloud distribution in the space. This extracted information is stored in the form of

$$x \approx \bar{x} + \Phi b_i \tag{A.2}$$

where $\bar{x}$ is the mean shape, represented as a vector of t points, $\Phi = (\varphi_1|\varphi_2|...|\varphi_t)$ is a matrix which contains the eigenvectors corresponding to the variation of the model at each point and b is a t-dimensional vector representing the modes of variation, and is widely know as point based shape variation model (PBSVM). This PBSVM is normally constrained between the values $\pm 3\sqrt{\lambda_i}, i = 1..t$, to be within the range of similar shapes to the ones used during the model construction.

To apply these constraints, we assume that the shapes are represented as a normal distribution of points across subjects. We could arbitrarily relax the region constraints and increase the maximum allowed deformation, however, we opted to limit it and to create a robust model, able to cope with potential pathologies or abnormalities inside the eye.

A.3 Active Shape Models (ASM)

We combine both the PBSVM and the MRI profile intensity information from the subject dataset to create an ASM. MRI does not provide homogeneous intensity values across subjects and structures; therefore, we require a reliable standardization algorithm to equalize the dataset. The standardization algorithm proposed by Nyul et al. [110] proved to be a simple yet reliable equalization method.

Then, prior to extracting the image profile information, we perform a set of image pre-processing techniques. First, we start by applying a gradient anisotropic diffusion filter‘[138] on the standardized images, with a conductance parameter of 1 and run 15 iterations. The filter will remove existing MRI noise while preserving important anatomical region edges. Second, we fix an arbitrary lower and upper threshold and filter the image to remove low and high intensity information. The objective is to achieve a good contrast between the anterior chamber and the lens, while preserving a good contrast of the vitreous humor and sclera region. Finally, we compute both the gradient (with a 1 voxel size kernel) and the Sobel operator of the windowed image.

The gradient gives us the profile information for the regions of the sclera + cornea and the vitreous humor. The Sobel operator provides the information about the lens region. Once processed, we retrieve the landmark point cloud information that we extracted in the previous (PBSVM) section and select an even distribution of points [111] over the surface of the different layers. We extract 350 points for the regions of the sclera + cornea and the vitreous humor and 300 points for the region of the lens.

The corresponding landmark point clouds across subjects allow us to extract the profiles normal to the surface and compute the mean profile intensity (for both Gradient and Sobel) and the covariance matrix across profiles.

The length of the profile depends on the region of interest. For the region of the sclera + cornea and the vitreous humor we select a profile length of 11 voxels. For the region of the lens we select a profile length of 9 voxels. An important remark concerning the profile extraction step is that whenever we encounter a profile whose Gradient/Sobel is not strong enough, we do not include it in the model. This profile selection process allows us to actively build the model with the strongest Gradient/Sobel profiles and increase the quality of the fitting during the automatic segmentation stage.

B

EyeModeler : A C++ Framework for Medical Image Analysis of the Eye

This annex covers the **EyeModeler**. A software that was developed during this PhD in order to support clinicians during the evaluation of ocular images, independently of the modality of use (*e.g.* MRI, Fundus, US, CT, ...), towards a multimodal navigation system for evaluating eye diseases. The tool is based on a framework called **Marvin** [139], a C++ library developed in collaboration with the University of Bern, and a combination of widely know software libraries in medical imaging and computer vision (ITK [1], VTK[2], QT Creator[3], Coin 3D[4] and OpenCV[5]). The code was written in C++ to increase acceptance in the medical community thanks to its efficiency and reliability.

B.1 Software notes

The software is ready to be installed in multiple platforms, including:

- *Linux - Ubuntu 12.04, 14.04* or superior,
- *Mac OS X 10.8* or superior and
- *Windows 7 ®*.

[1] **Insight Segmentation and Registration Toolkit (ITK)** - http://itk.org/
[2] **The Visualization Toolkit (VTK)** - http://www.vtk.org/
[3] **QT Creator** is a cross-platform C++, JavaScript and QML integrated development environment for QT - https://www.qt.io/
[4] **Coin3D** is a retained-mode toolkit for effective 3D graphics development Coin3D
[5] **OpenCV** is a library for high-performance computer vision and mathematical processing - http://opencv.org/

It is divided into several modules that enable the user to **load imaging data** (MRI, Fundus, ...), **annotate information relevant to the patient**, **build Active Shape Models (ASMs)** out of manual delineations of patient eye structures and to do the **automatic segmentation of the eye in 3D MRI** [2]. Furthermore, the software is designed as to be organ/shape independent, thus, it could be utilized for building statistical models for any shape from which 2D/3D delineations are present.

In addition, we contributed to prepare the **multimodal fusion framework** developed in De Zanet et al. [94] to be used as an additional module in **EyeModeler**. In the future this work could be easily deployed alongside the **multimodal fusion of pathological MRI and Fundus**, still under development and to be added in future releases of EyeModeler.

B.2 Modules

EyeModeler is organized into different modules, facilitating the user to work with specific tools depending on his needs. The different modules and submodules are:

Patient Manager : This module is the starting point for loading patient information into the system. It allows for the creation of patient profiles, to connect different image modalities from the file system to the patient entry and to create study groups for testing and evaluation. Once the information is loaded, handling of patients accross studies becomes easy and import/export of loaded data between multiple EyeModeler users is possible. Fig. B.1 shows a screenshot of the landing patient manager module.

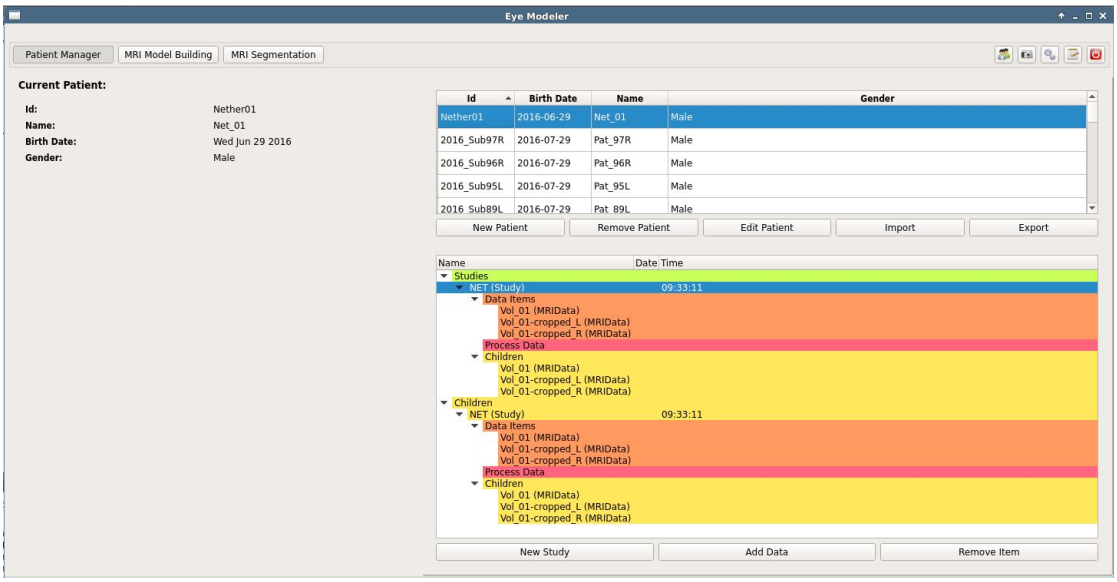

Figure B.1 – **Patient Manager** : Module for data loading and archiving. The results from different experiments are stored as part of the patient information folder.

MRI Model Building Module : The MRI model building section contains all the methods for creating a new ASM out of annotated patient information (labels and MRI volumes). It is connected to the *patient manager* module in order to load annotations from the file system. The whole processing diagram is shown in Fig.B.2, and is divided in the following consecutive steps:

- *Load MRI Volumes :* Loads the nifti/jpeg file list from the local computer path and processes the images into a format defined as **mvnImage**. This format is used within **EyeModeler** to ease the process of representation and transformation of medical sequences. The images may be composed of manual labels, for generating the shape, or MRI sequences, containing the profile intensity information.

- *Resize MRI Volumes (Optional) :* This function accounts for the resizing of the aforementioned volumes, towards a common reference resolution. As stated in chapters 2 and 3, in this PhD we worked with datasets of images with varying sizes and resolution, thus, resizing was required.

- *Calculate Distance Maps :* In here, we compute the *signed distance maps* from the labeled volumes, creating an atlas by simple averaging. All these procedures follow the structure proposed by Frangi et al. [105] and Cootes et al. [67].

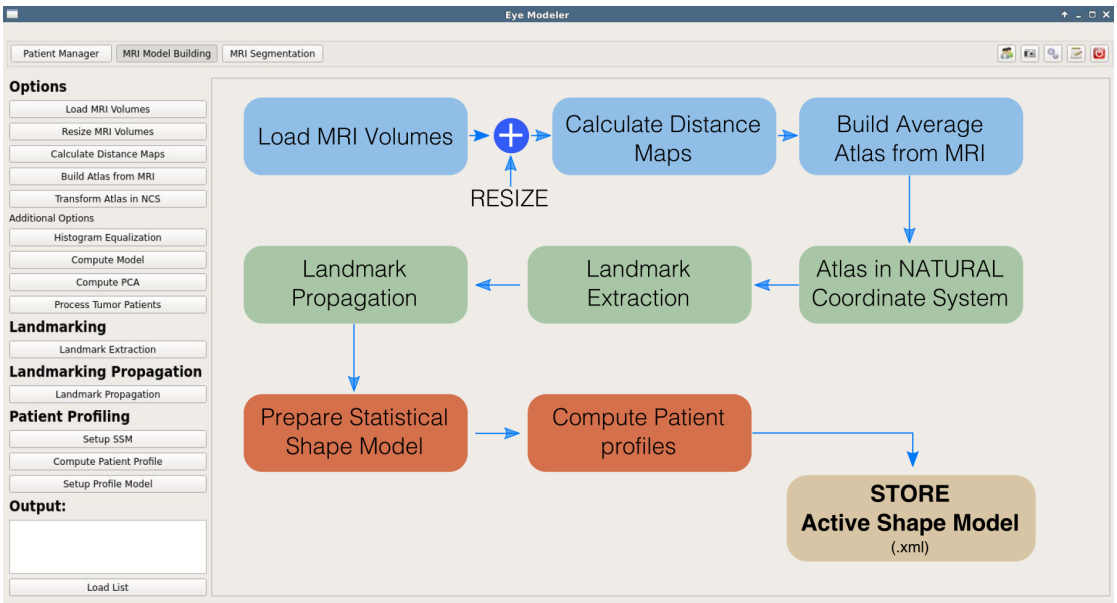

Figure B.2 – **MRI Model Building** : In this section we focus on generating the Active Shape Model that best represents the annotated data prior to the MRI segmentation. We created a set of sequential steps for storing intermediate results whenever evaluation is required.

- *Build Atlas from MRI :* This function operates once the average atlas has been created. We apply the *Diffeomorphic Demons* registration algorithm [107] in order to register

the average atlas to each patient, and store the deformation fields. The number of iterations and all the parameters specific to the registration algorithm can be fine-tuned depending on the requirements of the user. Alternatively, the default parameters are the ones used in chapters 2 and 3.

- *Transform Atlas into NCS :* This function computes the deformation field that connect each patient and the atlas, adding them together aand applying them to the average atlas. The resulting atlas becomes the new atlas in *Natural Coordinates System (NCS)* [105].
- *Landmark Extraction :* Once the process for generating the atlas in NCS is completed, we use *marching cubes* [108] to extract the landmarks representing the atlas surface. On a general basis, the landmarks will have far more point than those required to fully characterize the shape, thus, a decimation process will be conducted. All the intermediate hyperparameters can be fine-tuned to maximize the final results.
- *Landmark Propagation :* This method coregisters the *NCS atlas* against every patient using diffeomorphic demons and stores the deformation field. Afterwards, this transformation is applied to the selected group of landmarks from the NCS atlas.
- *Setup Statistical Shape Model (SSM) :* This function takes into consideration the spatial transformation from the previous steps, and allows us to compute a *Principal Component Analysis (PCA)* on the landmark points, towards encoding the *Point-Based Shape Variation Model (PBSVM)*. The implicit deformation of the point cloud will contain the shape variations present in our dataset.
- *Compute Patient Profile :* Once the model shape is modelled, we extract the intensity profiles normal to every landmark *wrt.* the shape formed by the surrounding points for all patients. The intensity information, stored as a vector of profiles accross subjects, will be encoded together with its specific landmark variability and stored inside the ASM.
- *Setup Profile Model :* Finally, after computing all the aforementioned methods, we store the model as **model.xml** file. The model is stored as an *xml* to foster easy transfer with other research groups or accross experiments.

MRI Segmentation : The present module introduces the fully automatic segmentation of the eye in 3D MRI. It contains a navigation window and a set of methods to explore the loaded volume and the different labeled regions (*e.g.* the sclera, the cornea, the vitreous humor and the lens for this project). Furthermore, it has an in-built clipping plane functionality that allows an easy transversal cut of multiple layers, creating an overlap of the model shape and the MRI cutting planes (see Fig. B.3).

- *Load Patient MRI :* This method takes care of loading the patient MRI volume and to represent it in the **navigation window**. Prior to loading a volume, the path to the file needs to be introduced in the system via the *patient manager*.

- *Crop Volume :* Once the volume is loaded, the user may decide to work exclusively with the *Region of Interest (ROI)*. To this, we allow for an automatic cropping of the eye region, as presented in [**?**, 2]. The cropping will generate one or two new volumes representing the eyes and will connect them to the specific patient entry from the *patient manager*.

- *Load Model :* This method loads the selected model from the list (generated in the **MRI Model Building Module**) into the system to prepare the automatic segmentation of the eye.

- *Initialize Model :* This function initializes the previously loaded model and prepares it for the fitting. That is, we perform all the necessary *image processing* techniques in order to prepare the volume for the automatic segmentation. The different steps are: *intensity windowing, histogram equalization* and *curvature anisotropic filtering [138]*. Furthermore, we give the user the possibility to modify the intensity scale, towards improving the final edge detection used to extract the profiles.

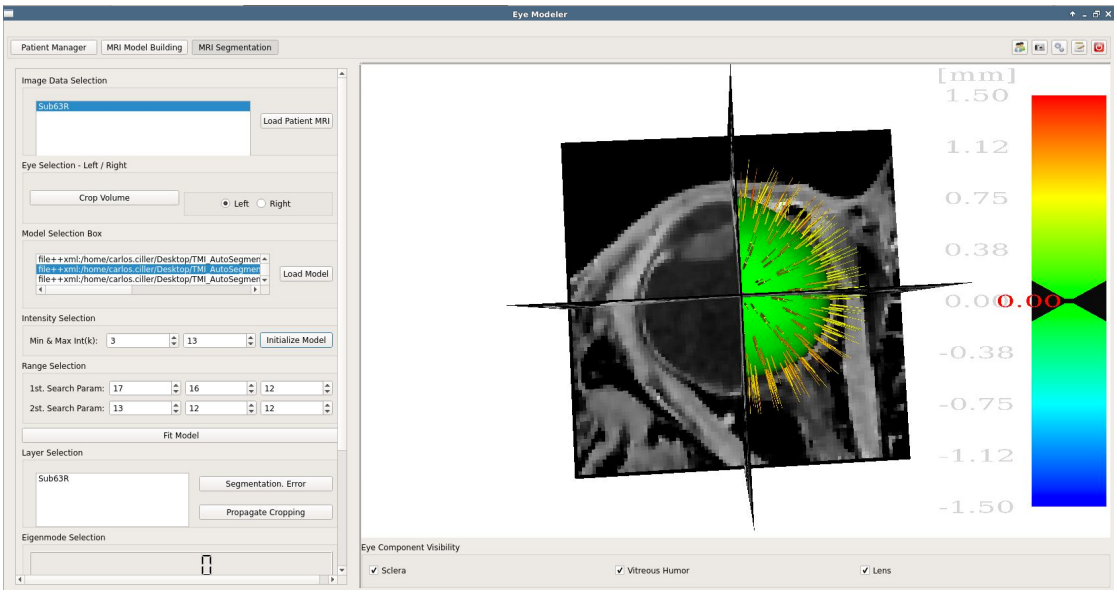

Figure B.3 – **MRI Model Segmentation** : In here we cover the automatic segmentation of 3D MRI. The software is ready to load volumes, crop them, select the region of the eyes and perform series of image processing steps before doing the automatic segmentation. The whole process takes on average 14s [2]. The green shape represents the model shape in NCS.

- *Fit Model :* This method proceeds to do the automatic segmentation by minimizing the Mahalanobis distance between the learn ASM intensity profiles and the current volume to segment. Deformations of the model follow in an iterative process until either reaching convergence or the maximum number of iterations.

- *Segmentation Error :* Segmentation errors allows to compare the current 3D MRI segmentation with the one defined by the clinician, in case that the user has the Ground Truth (GT) at disposition.

- *Propagate Cropping :* In order to perform the automatic segmentation of ocular tumors presented in chapter 3, it is desirable to have all the volumes in the same resolution, orientation and size. This method will processes the volume and store the results in a common reference spacing and size.

- *Eigenmode Selection :* This last method permits to evaluate the different modes of variation create during the PCA decomposition, while building the ASM.

The remaining information from the navigation system indicates the average distance to the mean shape in mm, and is represented as a color bar on the middle-right side of the screen. Moreover, the remaining contents of this thesis was implemented in Matlab ®and Python, and it is not still a functional part of the **EyeModeler**.

B.3 Conclusions and Future work

This software introduces a new tool for assessing the treatment planning and decision making process in ocular tumors. Our goal is to be able to provide the scientific community with a set of tools that clinicians can use in their daily work and to improve the analysis and evaluation of the disease. Previous tools allowed for the automatic delineation of eye structures on the assumption that the eye was defined as a parametric spherical shape [49], however, this is, to our knowledge, the first attempt to present a method for the segmentation of eye structure in MRI. Furthermore, the software is under constant development is being used by the research group performing Proton Theraphy for uveal melanoma, in the *Paul Scherrer Institute*, Villigen, Switzerland.

In the future we will also integrate **the automatic segmentation of ocular tumors** and the **multimodal fusion** developed in section 4 as additional modules for the **EyeModeler**. The ultimate goal of this application is to combine the techniques and the proposed registration/segmentation methods developed during this work in order to fuse multiple image modalities into a multi-modal patient specific eye model. By doing so, clinicians from a various background would be able to share visions and opinions in a simultaneous manner, towards easing the decision process during the treatment plan.

A few more screenshots of the current software can be observed in Fig. B.4. And a working video-demo of the software can be seen in this link [6].

[6] Automatic Segmentation of the eye in 3D MRI video : https://youtu.be/l_AoUTtWeo8

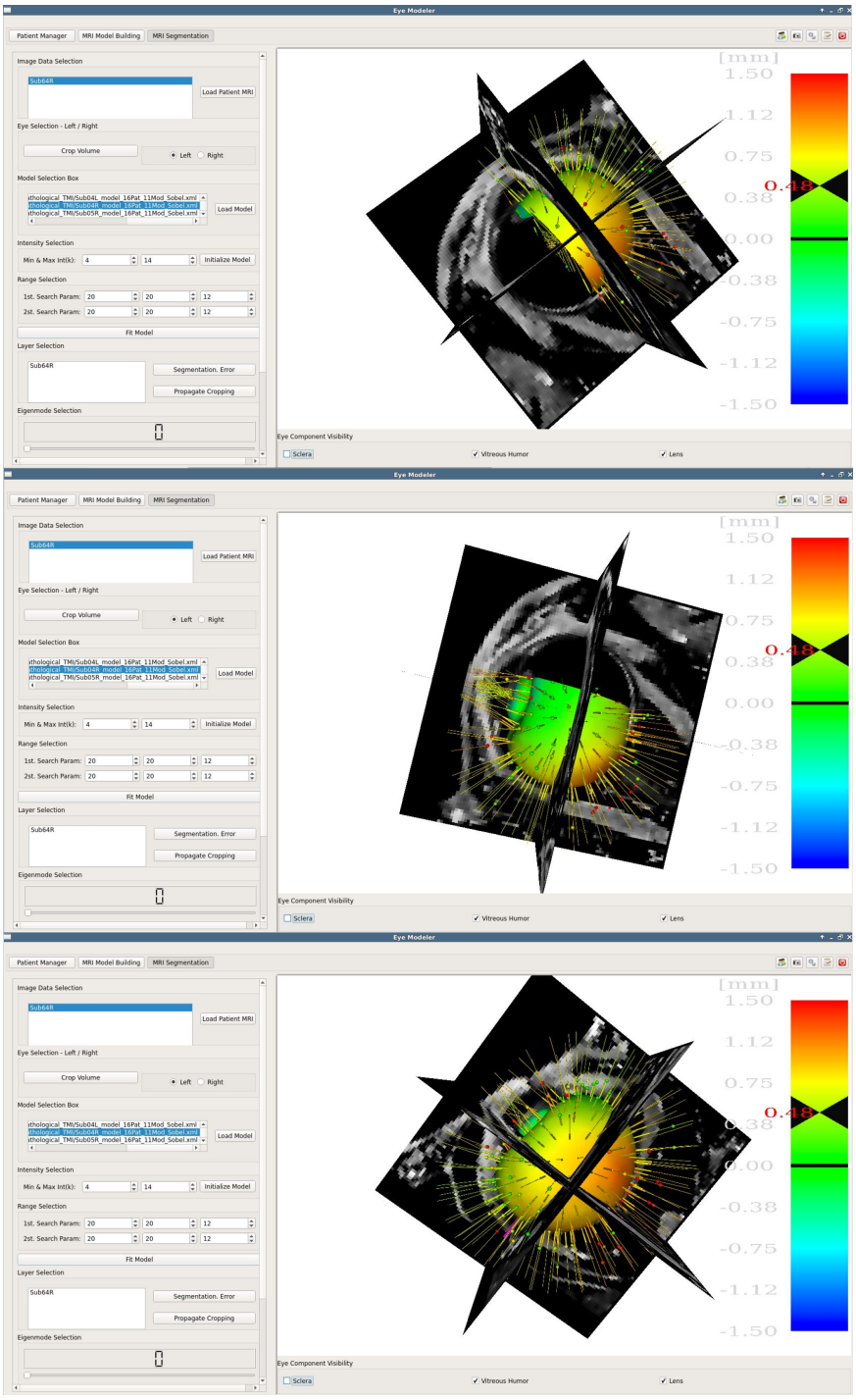

Figure B.4 – **EyeModeler** : EyeModeler navigation systems allows clinicians to explore different segmentation methods and to perform automatic segmentation of healthy and pathological eyes on the MRI.

Bibliography

[1] D. Huang, E. Swanson, C. Lin, J. Schuman, W. Stinson, W. Chang, M. Hee, T. Flotte, K. Gregory, C. Puliafito, a. et, Optical coherence tomography, Science 254 (5035) (1991) 1178–1181.

[2] C. Ciller, S. I. De Zanet, M. B. Rüegsegger, A. Pica, R. Sznitman, J.-P. Thiran, P. Maeder, F. L. Munier, J. H. Kowal, M. Bach Cuadra, Automatic Segmentation of the Eye in 3D Magnetic Resonance Imaging: A novel Statistical Shape Model for treatment planning of Retinoblastoma, International Journal of Radiation Oncology Biology Physics 92 (4) (2015) 794–802.

[3] C. L. Shields, J. A. Shields, Basic understanding of current classification and management of retinoblastoma, Current Opinion in Ophthalmology 17 (3) (2007) 228–234.

[4] H. Von Helmholtz, Beschreibung eines augen-spiegels, A Farstnerische Verlagsbuchhandlung.

[5] O. Gerloff, Uber die photographie des augenhintergrundes, Klin Monatsblätter Augenheilkunde 29 (1891) 397–403.

[6] A. Gullstrand, Neue methoden der reflexlosen ophthalmoskopie, Berichte Deutsche Ophthalmologische Gesellschaft 36.

[7] C. H. Keeler, Combined luminous ophthalmoscope and retinoscope, uS Patent 1,774,832 (1930).

[8] K. T. Dussik, Z Neurol Psychiat, Uber die moglichkeit hochfrequente mechanische schwingungen als diagnostisches hilfsmittel zu verwerten (1942) 174–153.

[9] D. Coleman, Reliability of ocular and orbital diagnosis with B-scan ultrasound. 2. Orbital diagnosis., American Journal Ophthalmology 74 (4) (1972) 704–18.

[10] N. R. Bronson, Y. L. Fisher, N. C. Pickering, E. M. Trayner, Ophthalmic Contact B-Scan Ultrasonography for the Clinician, Journal of Pediatric Ophthalmology and Strabismus 13 (1976) 365–366.

[11] L. A. Yannuzzi, M. D. Ober, J. S. Slakter, R. F. Spaide, Y. L. Fisher, R. W. Flower, R. Rosen, Ophthalmic fundus imaging: Today and beyond, American Journal of Ophthalmology 137 (3) (2004) 511–524.

[12] H. J. Brisse, L. Lumbroso, P. C. Fréneaux, P. Validire, F. P. Doz, E. J. Quintana, O. Berges, L. C. Desjardins, S. G. Neuenschwander, Sonographic, CT, and MR imaging findings in diffuse infiltrative retinoblastoma: Report of two cases with histologic comparison, American Journal of Neuroradiology 22 (3) (2001) 499–504.

[13] D. Brenner, C. Elliston, E. Hall, W. Berdon, Estimated risks of radiation-induced fatal cancer from pediatric CT., AJR. American journal of roentgenology 176 (2) (2001) 289–96.

[14] P. Galluzzi, T. Hadjistilianou, a. Cerase, S. De Francesco, P. Toti, C. Venturi, Is CT still useful in the study protocol of retinoblastoma?, AJNR. American journal of neuroradiology 30 (9) (2009) 1760–5.

[15] D. J. Brenner, E. J. Hall, Computed tomography–an increasing source of radiation exposure., The New England journal of medicine 357 (22) (2007) 2277–2284.

[16] N. M. Bressler, S. B. Bressler, S. L. Fine, Age-related macular degeneration, Survey of Ophthalmology 32 (6) (1988) 375 – 413.

[17] C. P. Wilkinson, F. L. Ferris, R. E. Klein, P. P. Lee, C. D. Agardh, M. Davis, D. Dills, A. Kampik, R. Pararajasegaram, J. T. Verdaguer, F. Lum, Proposed international clinical diabetic retinopathy and diabetic macular edema disease severity scales, Ophthalmology 110 (9) (2003) 1677–1682.

[18] H. MR, P. CA, W. C, et al, Quantitative assessment of macular edema with optical coherence tomography, Archives of Ophthalmology 113 (8) (1995) 1019–1029.

[19] R. D. Jager, W. F. Mieler, J. W. Miller, Age-Related Macular Degeneration, The New England Journal of Medicine 358 (24) (2008) 2606–2617.

[20] C. Ciller, S. I. De Zanet, A. Pica, J.-P. Thiran, P. Maeder, F. L. Munier, J. H. Kowal, M. Bach Cuadra, Automatic magnetic resonance imaging segmentation of the eye based on 3D Active Shape Models, in: ARVO 2014 Annual Meeting, 2014.

[21] C. Ciller, S. I. De Zanet, K. Kamnitsas, P. Maeder, B. Glocker, F. L. Munier, D. Rueckert, J.-P. Thiran, M. Bach Cuadra, R. Sznitman, Multi-channel MRI segmentation of eye structures and tumors using patient-specific features, Under Review - Plos One XX (X) (2016) XXX.

[22] C. Ciller, S. I. De Zanet, P. Maeder, A. Pica, F. L. Munier, J.-P. Thiran, R. Sznitman, M. Bach Cuadra, Topographic Fundus Mapping: Improving multimodal eye tumor analysis by fusion of MRI and Fundus Image Photography, Under Preparation - IEEE Transactions on Medical Imaging XX (X) (2016) XXX.

[23] W. D. Paley, Natural Theology of Evidences of the Existence and Attributes of the Deity, 1802.

[24] A. Y. Bedikian, S. S. Legha, G. Mavligit, C. H. Carrasco, S. Khorana, C. Plager, N. Papadopoulos, R. S. Benjamin, Treatment of uveal melanoma metastatic to the liver. a review of the m. d. anderson cancer center experience and prognostic factors, Cancer 76 (9) (1995) 1665–1670.

[25] M. Niemeijer, B. Van Ginneken, S. R. Russell, M. S. A. Suttorp-Schulten, M. D. Abràmoff, Automated detection and differentiation of drusen, exudates, and cotton-wool spots in digital color fundus photographs for diabetic retinopathy diagnosis, Investigative Ophthalmology and Visual Science 48 (5) (2007) 2260–2267. arXiv:NIHMS150003.

[26] M. R. Hee, C. A. Puliafito, J. S. Duker, E. Reichel, J. G. Coker, J. R. Wilkins, J. S. Schuman, E. A. Swanson, J. G. Fujimoto, Topography of diabetic macular edema with optical coherence tomography., Ophthalmology 105 (2) (1998) 360–70.

[27] J. L. Jay, D. Allan, The benefit of early trabeculectomy versus conventional management in primary open angle glaucoma relative to severity of disease, Eye 3 (5) (1989) 528–535.

[28] L. M, C. AS, W. S, H. LG, S. AP, Risk factors for open-angle glaucoma: The barbados eye study, Archives of Ophthalmology 113 (7) (1995) 918–924.

[29] D. Garway-Heath, S. Ruben, A. Viswanathan, R. Hitchings, Vertical cup/disc ratio in relation to optic disc size: its value in the assessment of the glaucoma suspect, The British Journal of Ophthalmology 82 (10) (1998) 1118–1124.

[30] R. Sihota, Lasers in primary open angle glaucoma, Indian Journal of Ophthalmology 59 (Suppl1) (2011) S114–S117.

[31] A. Balmer, L. Zografos, F. Munier, Diagnosis and current management of retinoblastoma., Oncogene 25 (38) (2006) 5341–9.

[32] E. S. Gragoudas, K. M. Egan, J. M. Seddon, R. J. Glynn, S. M. Walsh, S. M. Finn, J. E. Munzenrider, M. D. Spar, Survival of patents with metastases from uveal melanoma, Ophthalmology 98 (3) (1991) 383 – 390.

[33] F. L. Munier, J. Verwey, A. Pica, A. Balmer, L. Zografos, A. Hana, T. Beate, G. Gudrun, M. Raphaël, New developments in external beam radiotherapy for retinoblastoma: from lens to normal tissue-sparing techniques, Clinical & Experimental Ophthalmology 36 (1) (2008) 78–89.

[34] G. Alfred, J. Knudson, Mutation and cancer: statistical study of retinoblastoma., Proceedings of the National Academy of Sciences of the United States of America 68 (4) (1971) 820–823.

[35] C.-l. Yu, M. A. Tucker, D. H. Abramson, K. Furukawa, J. M. Seddon, M. Stovall, J. F. F. Jr, R. A. Kleinerman, Cause-Specific Mortality in Long-Term Survivors of Retinoblastoma 101 (8) (2009) 581–591.

[36] C. L. Shields, J. a. Shields, Retinoblastoma management: advances in enucleation, intravenous chemoreduction, and intra-arterial chemotherapy., Current opinion in ophthalmology 21 (3) (2010) 203–212.

[37] P. de Graaf, S. Göricke, F. Rodjan, P. Galluzzi, P. Maeder, J. a. Castelijns, H. J. Brisse, Guidelines for imaging retinoblastoma: imaging principles and MRI standardization., Pediatric radiology 42 (1) (2012) 2–14.

[38] K. D. Wright, I. Qaddoumi, Z. Patay, A. Gajjar, M. W. Wilson, C. Rodriguez-Galindo, Successful Treatment of Early Detected Trilateral Retinoblastoma Using Standard Infant Brain Tumor Therapy, Pediatric blood & cancer 55 (3) (2010) 570–572.

[39] M. C. de Jong, P. de Graaf, H. J. Brisse, P. Galluzzi, S. L. Göricke, A. C. Moll, F. L. Munier, M. Beck Popovic, A. P. Moulin, S. Binaghi, J. A. Castelijns, P. Maeder, The potential of 3T high-resolution magnetic resonance imaging for diagnosis, staging and follow-up of retinoblastoma, Survey of Ophthalmology 60 (4) (2015) 346–55.

[40] D. S. Gombos, J. Hungerford, D. H. Abramson, J. Kingston, G. Chantada, I. J. Dunkel, C. B. G. Antoneli, M. Greenwald, B. G. Haik, C. A. Leal, A. Medina-sanson, A. C. Schefler, G. Veerakul, R. Wieland, N. Bornfeld, M. W. Wilson, C. Bing, O. Yu, Secondary Acute Myelogenous Leukemia in Patients with Retinoblastoma, Ophthalmology 114 (7) (2007) 1378–1383.

[41] A. Balmer, F. Munier, Differential diagnosis of leukocoria and strabismus , fi rst presenting signs of retinoblastoma, Clinical Ophthalmology 1 (4) (2007) 431–439.

[42] W. D. Newhauser, N. C. Koch, J. D. Fontenot, S. J. Rosenthal, D. S Gombos, M. M. Fitzek, R. Mohan, Dosimetric impact of tantalum markers used in the treatment of uveal melanoma with proton beam therapy., Physics in medicine and biology 52 (2007) 3979–3990.

[43] M. Chintagumpala, P. Chevez-Barrios, E. a. Paysse, S. E. Plon, R. Hurwitz, Retinoblastoma: review of current management., The oncologist 12 (10) (2007) 1237–46.

[44] L. Lumbroso-Le Rouic, I. Aerts, C. Lévy-Gabriel, R. Dendale, X. Sastre, M. Esteve, B. Asselain, D. Bours, F. Doz, L. Desjardins, Conservative treatments of intraocular retinoblastoma., Ophthalmology 115 (8) (2008) 1405–10, 1410.e1–2.

[45] A. D. Singh, A. Topham, Incidence of uveal melanoma in the United States: 1973-1997, Ophthalmology 110 (03) (2003) 956–961.

[46] K. Buder, A. Gesierich, G. Gelbrich, M. Goebeler, Cancer Medicine, Cancer Medicine 2 (5) (2013) 674–686.

[47] C. L. Shields, S. Kaliki, M. Furuta, A. Mashayekhi, J. A. Shields, Clinical Spectrum and prognosis of uveal melanoma based on age at presentation in 8.033 cases, Retina 32 (7).

[48] J. A. Shields, L. C. Glazer, W. F. Mieler, C. L. Shields, M. S. Gottlieb, Comparison of xenon arc and argon laser photocoagulation in the treatment of choroidal melanomas, American Journal of Ophthalmology 109 (6) (1990) 647 – 655.

[49] B. Dobler, R. Bendl, Precise modelling of the eye for proton therapy of intra-ocular tumours., Physics in medicine and biology 47 (4) (2002) 593–613.

[50] M. D. Abramoff, M. K. Garvin, M. Sonka, Retinal Imaging and Image Analysis, ... Engineering, IEEE Reviews ... 3 (1) (2010) 169–208.

[51] R. Brown, Y.-C. N. Cheng, M. Haacke, M. R. Thompson, R. Venkatesan, Magnetic Resonance Imaging - Physical Principles and Sequence Design - Second Edition, John Wiley and Sons Ltd, 2014.

[52] S. G. Wetzel, G. Johnson, A. G. S. Tan, S. Cha, E. A. Knopp, V. S. Lee, D. Thomasson, N. M. Rofsky, Imaging of the brain with a volumetric interpolated examination, American Journal of Neuroradiology 23 (July) (2002) 995–1002.

[53] D. He, H. Yu, Y. Chen, Equity in the distribution of ct and mri in china: a panel analysis, International Journal for Equity in Health 12 (2013) 39–39.

[54] M. Naik, K. Tourani, G. Sekhar, S. Honavar, Interpretation of computed tomography imaging of the eye and orbit. A systematic approach, Indian Journal of Ophthalmology 50 (4) (2002) 339–353.

[55] M. C. de Jong, P. de Graaf, D. P. Noij, S. Göricke, P. Maeder, P. Galluzzi, H. J. Brisse, A. C. Moll, J. a. Castelijns, Diagnostic performance of magnetic resonance imaging and computed tomography for advanced retinoblastoma: a systematic review and meta-analysis., Ophthalmology 121 (5) (2014) 1109–18.

[56] H. Olivecrona, P. A. Agerberg, A. Huaman, Ct diagnosis of retinoblastoma with histopathologic correlations, European Radiology 4 (4) (1994) 307–313.

[57] C. Jacquemin, Z. A. Karcioglu, Detection of optic nerve involvement in retinoblastoma with enhanced computed tomography., Eye (Lond) 12 (Pt 2) (1998) 179–83.

[58] W. Drexler, J. G. Fujimoto, Optical coherence tomography: Technology and applications, Springer Berlin Heidelberg, 2008.

[59] J. F. de Boer, B. Cense, B. H. Park, M. C. Pierce, G. J. Tearney, B. E. Bouma, Improved signal-to-noise ratio in spectral-domain compared with time-domain optical coherence tomography, Opt. Lett. 28 (21) (2003) 2067–2069.

[60] Z. Yaqoob, J. Wu, C. Yang, Spectral domain optical coherence tomography: a better OCT imaging strategy., BioTechniques 39 (6 Suppl).

[61] C. A. Puliafito, M. R. Hee, C. P. Lin, E. Reichel, J. S. Schuman, J. S. Duker, J. A. Izatt, E. A. Swanson, J. G. Fujimoto, Imaging of macular diseases with optical coherence tomography, Ophthalmology 102 (2) (1995) 217 – 229.

[62] J. Saktanasate, J. Matz, E. Anthony T. Say, C. L. Shields, Reveals Important Retinal Features of Retinoblastoma, Retina Today (June) (2015) 48–50.

[63] A. P. Dhawan, Medical Image Analysis, John Wiley and Sons, Inc., 2011.

[64] N. Sharma, L. M. Aggarwal, Automated medical image segmentation techniques, Journal of Medical Physics / Association of Medical Physicists of India 35 (1) (2010) 3–14.

[65] D. L. Pham, C. Xu, J. L. Prince, Current Methods in Medical Image Segmentation, Annual Reviews Biomedical Engineering 02 (2000) 315–37.

[66] T. Cootes, E. Baldock, J. Graham, An introduction to active shape models, Image Processing and Analysis (2000) 223–248.

[67] T. F. Cootes, C. J. Taylor, D. H. Cooper, J. Graham, Active shape models - their training and application, Comput. Vis. Image Underst. 61 (1) (1995) 38–59.

[68] T. Heimann, H.-P. Meinzer, Statistical shape models for 3D medical image segmentation: a review., Medical image analysis 13 (4) (2009) 543–63.

[69] M. Kass, A. Witkin, D. Terzopoulos, Snakes: Active contour models, Vol. 1, 1988.

[70] W. E. L. Grimson, T. Lozano-Perez, D. P. Huttenlocher, Object recognition by computer : the role of geometric constraints, MIT Press, 1990.

[71] A. Beinglass, H. J. Wolfson, Articulated object recognition, or: how to generalize the generalized hough transform, in: Computer Vision and Pattern Recognition, 1991. Proceedings CVPR '91., IEEE Computer Society Conference on, 1991, pp. 461–466.

[72] C. Goodall, Procrustes methods in the statistical analysis of shape, Journal of the Royal Statistical Society. Series B (Methodological) 53 (2) (1991) 285–339.

[73] U. Grenander, Y. Chow, D. M. Keenan, Hands: A Pattern Theoretic Study of Biological Shapes, Springer-Verlag New York, Inc., New York, NY, USA, 1991.

[74] B. Flury, Multivariate Statistics: A Practical Approach, Chapman & Hall, Ltd., London, UK, UK, 1988.

[75] T. F. Cootes, G. J. Edwards, C. J. Taylor, Active appearance models, Springer Berlin Heidelberg, Berlin, Heidelberg, 1998, pp. 484–498.

[76] D. Cristinacce, T. F. Cootes, Feature Detection and Tracking with Constrained Local Models., Bmvc 2 (5) (2006) 6.

[77] C. Lindner, S. Thiagarajah, J. M. Wilkinson, T. arcOGEN Consortium, G. A. Wallis, T. F. Cootes, Fully automatic segmentation of the proximal femur using random forest regression voting, IEEE Transactions on Medical Imaging 32 (8) (2013) 1462–1472.

[78] A. Turing, Computing Machinery and Intelligence, Mind LIX (236) (1950) 433–460.

[79] C. M. Bishop, Pattern Recognition and Machine Learning (Information Science and Statistics), Springer-Verlag New York, Inc., Secaucus, NJ, USA, 2006.

[80] T. Hastie, R. Tibshirani, J. Friedman, The Elements of Statistical Learning, Springer Series in Statistics, Springer New York Inc., New York, NY, USA, 2001.

[81] K. P. Murphy, Machine Learning: A Probabilistic Perspective, The MIT Press, 2012.

[82] M. N. Wernick, Y. Yang, J. G. Brankov, G. Yourganov, S. C. Strother, Machine Learning in Medical Imaging, IEEE signal processing magazine 27 (4) (2010) 25–38.

[83] B. Scholkopf, A. J. Smola, Learning with Kernels: Support Vector Machines, Regularization, Optimization, and Beyond, MIT Press, Cambridge, MA, USA, 2001.

[84] L. Breiman, Random forests, Machine Learning 45 (1) (2001) 5–32.

[85] Y. Pao, Adaptive pattern recognition and neural networks, Reading, MA (US); Addison-Wesley Publishing Co., Inc., 1989.

[86] F. Rosenblatt, Principles of Neurodynamics: Perceptrons and the Theory of Brain Mechanisms, Spartan Books, Washington, 1962.

[87] Y. Lecun, L. Bottou, Y. Bengio, P. Haffner, Gradient-based learning applied to document recognition, in: Proceedings of the IEEE, 1998, pp. 2278–2324.

[88] A. Krizhevsky, I. Sutskever, G. E. Hinton, Imagenet classification with deep convolutional neural networks, in: F. Pereira, C. J. C. Burges, L. Bottou, K. Q. Weinberger (Eds.), Advances in Neural Information Processing Systems 25, Curran Associates, Inc., 2012, pp. 1097–1105.

[89] Y. Bengio, A. Courville, P. Vincent, Representation learning: A review and new perspectives, IEEE Trans. Pattern Anal. Mach. Intell. 35 (8) (2013) 1798–1828.

[90] J. Schmidhuber, Deep Learning in neural networks: An overview, Neural Networks 61 (2015) 85–117. arXiv:1404.7828.

[91] Y. LeCun, Y. Bengio, G. Hinton, Deep learning, Nature Methods 13 (1) (2015) 35–35.

[92] F. Barkhof, M. Smeets, P. van der Valk, K. E. W. P. Tan, F. Hoogenraad, J. Peeters, J. Valk, Mr imaging in retinoblastoma, European Radiology 7 (5) (1997) 726–731.

[93] A. Khurana, C. A. Eisenhut, W. Wan, K. B. Ebrahimi, C. Patel, J. M. O'Brien, K. Yeom, H. E. Daldrup-Link, Comparison of the diagnostic value of mr imaging and ophthalmoscopy for the staging of retinoblastoma, European Radiology 23 (5) (2013) 1271–1280.

[94] S. I. De Zanet, C. Ciller, T. Rudolph, P. Maeder, F. Munier, A. Balmer, M. B. Cuadra, J. H. Kowal, Landmark detection for fusion of fundus and MRI toward a patient-specific multimodal eye model., IEEE transactions on bio-medical engineering 62 (2) (2015) 532–40.

[95] S. S. Devesa, The incidence of retinoblastoma, Am J Ophthalmol. 80 (2) (1975) 263–265.

[96] P. de Graaf, D. L. Knol, A. C. Moll, S. M. Imhof, A. Y. N. S. van Meeteren, J. A. Castelijns, Eye size in retinoblastoma: Mr imaging measurements in normal and affected eyes, Radiology 244 (1) (2007) 273–280.

[97] L. Fanea, A. J. Fagan, Review: magnetic resonance imaging techniques in ophthalmology., Molecular vision 18 (November 2011) (2012) 2538–60.

[98] M. B. Cuadra, S. Gorthi, F. I. Karahanoglu, F. Salvador, Model-based Segmentation and Image Fusion of 3D Computed Tomography and 3D Ultrasound of the Eye for Radiotherapy Planning, Second ECCOMAS Thematic Conference on Computational Vision and Medical Image Processing (2009) 53–58.

[99] M. B. Rüegsegger, M. Bach Cuadra, A. Pica, C. a. Amstutz, T. Rudolph, D. Aebersold, J. H. Kowal, Statistical modeling of the eye for multimodal treatment planning for external beam radiation therapy of intraocular tumors., International journal of radiation oncology, biology, physics 84 (4) (2012) e541–7.

[100] J.-W. M. Beenakker, D. P. Shamonin, A. G. Webb, G. P. M. Luyten, B. C. Stoel, Automated retinal topographic maps measured with magnetic resonance imagingretinal topographic maps measured with mri, Investigative Ophthalmology and Visual Science 56 (2) (2015) 1033.

[101] M. Goitein, T. Miller, Planning proton therapy of the eye., Med Physics 3 (10) (1983) 275–283.

[102] K. D. Singh, N. S. Logan, B. Gilmartin, Three-dimensional modeling of the human eye based on magnetic resonance imaging., Investigative ophthalmology & visual science 47 (6) (2006) 2272–9.

[103] K. D. Fritscher, M. Peroni, P. Zaffino, M. F. Spadea, R. Schubert, G. Sharp, Automatic segmentation of head and neck ct images for radiotherapy treatment planning using multiple atlases, statistical appearance models, and geodesic active contours, Medical Physics 41 (5).

[104] B. Maan, D. F. van der Heijden, Prostate mr image segmentation using 3d active appearance models, PRostate MR Image SEgmentation, PROMISE 2012 (2012) 44–51.

[105] A. F. Frangi, D. Rueckert, J. a. Schnabel, W. J. Niessen, Automatic construction of multiple-object three-dimensional statistical shape models: application to cardiac modeling., IEEE transactions on medical imaging 21 (9) (2002) 1151–66.

[106] H. C. Fledelius, A. C. Christensen, Reappraisal of the human ocular growth curve in fetal life, infancy, and early childhood., The British journal of ophthalmology 80 (10) (1996) 918–21.

[107] T. Vercauteren, X. Pennec, A. Perchant, N. Ayache, Diffeomorphic demons: Efficient non-parametric image registration, NeuroImage 45 (1, Supplement 1) (2009) S61 – S72, mathematics in Brain Imaging.

[108] W. E. Lorensen, H. E. Cline, Marching cubes: A high resolution 3D surface construction algorithm, ACM SIGGRAPH Computer Graphics 21 (4) (1987) 163–169.

[109] I. T. Jolliffe, Principal Component Analysis, Springer-Verlag, Berlin; New York, 1986.

[110] L. G. Nyúl, J. K. Udupa, On standardizing the MR image intensity scale., Magnetic resonance in medicine : official journal of the Society of Magnetic Resonance in Medicine / Society of Magnetic Resonance in Medicine 42 (6) (1999) 1072–81.

[111] H. Vogel, A better way to construct the sunflower head, Mathematical Biosciences 44 (3-4) (1979) 179–189.

[112] M. Peroni, M. Spadea, M. Riboldi, S. Falcone, C. Vaccaro, G. Sharp, G. Baroni, Validation of automatic contour propagation for 4d treatment planning using multiple metrics, Technol Cancer Res Treat 12 (6) (2013) 501–510.

[113] T. Rohlfing, Image similarity and tissue overlaps as surrogates for image registration accuracy: Widely used but unreliable, IEEE Transactions on Medical Imaging 31 (2) (2012) 153–163.

[114] B. H. Menze, A. Jakab, S. Bauer, J. Kalpathy-cramer, K. Farahani, J. Kirby, Y. Burren, N. Porz, J. Slotboom, R. Wiest, L. Lanczi, E. Gerstner, M.-a. Weber, T. Arbel, B. B. Avants, N. Ayache, P. Buendia, D. L. Collins, N. Cordier, J. J. Corso, A. Criminisi, T. Das, C. R. Durst, M. Dojat, S. Doyle, J. Festa, F. Forbes, E. Geremia, B. Glocker, P. Golland, X. Guo, A. Hamamci, K. M. Iftekharuddin, R. Jena, N. M. John, R. Meier, D. Precup, S. J. Price, T. Riklin-raviv, S. M. S. Reza, M. Ryan, L. Schwartz, H.-c. Shin, J. Shotton, C. A. Silva, N. Sousa, N. K. Subbanna, G. Szekely, T. J. Taylor, O. M. Thomas, N. J. Tustison, G. Unal, F. Vasseur, M. Wintermark, D. H. Ye, L. Zhao, B. Zhao, D. Zikic, M. Prastawa, M. Reyes, K. V. Leemput, The Multimodal Brain Tumor Image Segmentation Benchmark (BRATS), Medical Imaging, IEEE Transactions on (2014) 1–32.

[115] A. Makropoulos, I. S. Gousias, C. Ledig, P. Aljabar, A. Serag, J. V. Hajnal, A. D. Edwards, S. J. Counsell, D. Rueckert, Automatic whole brain MRI segmentation of the developing neonatal brain, IEEE Transactions on Medical Imaging 33 (9) (2014) 1818–1831.

[116] V. Harati, R. Khayati, A. Farzan, Fully automated tumor segmentation based on improved fuzzy connectedness algorithm in brain MR images., Computers in biology and medicine 41 (7) (2011) 483–92.

[117] M. Salah, I. Diaz, R. Greiner, P. Boulanger, B. Hoehn, A. Murtha, Fully Automated Brain Tumor Segmentation using two MRI Modalities, in: Advances in Visual Computing: 9th International Symposium, ISVC 2013, Rethymnon, Crete, Greece, July 29-31, 2013. Proceedings, Part I, 2013, pp. 30–39.

[118] S. Bauer, L.-P. Nolte, M. Reyes, Fully automatic segmentation of brain tumor images using support vector machine classification in combination with hierarchical conditional random field regularization., Medical image computing and computer-assisted intervention : MICCAI ... International Conference on Medical Image Computing and Computer-Assisted Intervention 14 (2011) 354–61.

[119] K. Kamnitsas, C. Ledig, V. F. J. Newcombe, J. P. Simpson, A. D. Kane, D. K. Menon, D. Rueckert, B. Glocker, Efficient multi-scale 3d CNN with fully connected CRF for accurate brain lesion segmentation, arxiv:160305959.

[120] B. H. Menze, A. Jakab, S. Bauer, J. Kalpathy-Cramer, K. Farahani, J. Kirby, Y. Burren, N. Porz, J. Slotboom, R. Wiest, L. Lanczi, E. Gerstner, M. A. Weber, T. Arbel, B. B. Avants, N. Ayache, P. Buendia, D. L. Collins, N. Cordier, J. J. Corso, A. Criminisi, T. Das, H. Delingette, C. Demiralp, C. R. Durst, M. Dojat, S. Doyle, J. Festa, F. Forbes, E. Geremia, B. Glocker, P. Golland, X. Guo, A. Hamamci, K. M. Iftekharuddin, R. Jena, N. M. John, E. Konukoglu, D. Lashkari, J. A. Mariz, R. Meier, S. Pereira, D. Precup, S. J. Price, T. R. Raviv, S. M. S. Reza, M. Ryan, D. Sarikaya, L. Schwartz, H.-C. Shin, J. Shotton, C. A. Silva, N. Sousa, N. K. Subbanna, G. Szekely, T. J. Taylor, O. M. Thomas, N. J. Tustison, G. Unal, F. Vasseur, M. Wintermark, D. H. Ye, L. Zhao, B. Zhao, D. Zikic, M. Prastawa, M. Reyes, K. V. Leemput, The multimodal brain tumor image segmentation benchmark (brats), IEEE Transactions on Medical Imaging 34 (10) (2015) 1993–2024.

[121] P. Kohli, P. H. S. Torr, Dynamic graph cuts for efficient inference in markov random fields, Pattern Analysis and Machine Intelligence, IEEE Transactions on 29 (12) (2007) 2079–2088.

[122] Y. Boykov, M.-P. Jolly, Interactive graph cuts for optimal boundary & region segmentation of objects in N-D images, Proceedings Eighth IEEE International Conference on Computer Vision. ICCV 2001 1 (July) (2001) 105–112.

[123] T. Hastie, R. Tibshirani, J. Friedman, The Elements of Statistical Learning, Springer, 2001.

[124] A. Lucchi, K. Smith, R. Achanta, G. Knott, P. Fua, Supervoxel-based segmentation of mitochondria in em image stacks with learned shape features, IEEE Transactions on Medical Imaging 31 (2) (2012) 474–486.

[125] R. Achanta, A. Shaji, K. Smith, A. Lucchi, P. Fua, S. Süsstrunk, SLIC superpixels compared to state-of-the-art superpixel methods, IEEE Transactions on Pattern Analysis and Machine Intelligence 34 (11) (2012) 2274–2281.

[126] N. Srivastava, G. E. Hinton, A. Krizhevsky, I. Sutskever, R. Salakhutdinov, Dropout : A Simple Way to Prevent Neural Networks from Overfitting, Journal of Machine Learning Research (JMLR) 15 (2014) 1929–1958.

[127] S. Ioffe, C. Szegedy, Batch Normalization: Accelerating Deep Network Training by Reducing Internal Covariate Shift, arXiv:1502.03167 (2015) 1–11.

[128] J. Nayak, P. S. Bhat, R. Acharya U, C. M. Lim, M. Kagathi, Automated identification of diabetic retinopathy stages using digital fundus images, J. Med. Syst. 32 (2) (2008) 107–115.

[129] C. Sinthanayothin, J. F. Boyce, H. L. Cook, T. H. Williamson, Automated localisation of the optic disc, fovea, and retinal blood vessels from digital colour fundus images., The British journal of ophthalmology 83 (8) (1999) 902–910.

[130] B. Delaunay, Sur la sphère vide. A la mémoire de Georges Voronoï, Bulletin de l'Académie des Sciences de l'URSS (6) (1934) 793–800.

[131] P. J. Besl, H. D. McKay, A method for registration of 3-d shapes, IEEE Transactions on Pattern Analysis and Machine Intelligence 14 (2) (1992) 239–256.

[132] W. M. Wells, P. Viola, H. Atsumi, S. Nakajima, R. Kikinis, Multi-modal volume registration by maximization of mutual information., Medical image analysis 1 (1) (1996) 35–51.

[133] J. P. W. Pluim, J. B. a. Maintz, M. a. Viergever, Mutual information based registration of medical images: a survey, IEEE Transactions on medical imaging 22 (8) (2003) 1–21.

[134] A. A. Wenzel, M. N. O'Hare, M. Shadmand, T. W. Corson, Optical coherence tomography enables imaging of tumor initiation in the TAg-RB mouse model of retinoblastoma, Molecular Vision 21 (2015) 515–522.

[135] D. B. Rootman, E. Gonzalez, A. Mallipatna, C. VandenHoven, L. Hampton, H. Dimaras, H. S. L. Chan, B. L. Gallie, E. Heon, Hand-held high-resolution spectral domain optical coherence tomography in retinoblastoma: clinical and morphologic considerations, British Journal of Ophthalmology 97 (1) (2013) 59–65. arXiv:http://bjo.bmj.com/content/97/1/59.full.pdf+html.

[136] G. Loy, A. Zelinsky, A Fast Radial Symmetry Transform for Detecting Points of Interest, European Conference on Computer Vision (2002) 358–368.

[137] T. Zhang, G. Golub, Optimal Surface Smoothing as Filter Design, Research Report IBM 20404.

[138] P. Perona, J. Malik, Scale-space and edge detection using anisotropic diffusion, Pattern Analysis and Machine Intelligence, IEEE Transactions on 12 (7) (1990) 629–639.

[139] T. Rudolph, M. Puls, C. Anderegg, L. Ebert, M. Broehan, A. Rudin, J. Kowal, Marvin: A medical research application framework based on open source software, Comput. Methods Prog. Biomed. 91 (2) (2008) 165–174.

Carlos CILLER
1009 Pully (Switzerland)
Phone: (+41) 78 712 21 62
Email: carlos.cillerruiz@unil.ch

Date of birth: 14/12/1986
Nationality: Spanish
Marital status: Single
Driving License (B), Own car

Profile: ▷ *A PhD Student between the Medical Image Analysis Laboratory (MIAL) from UNIL, part of the CIBM (EPFL / UNIL) and the ARTORG Center of the University of Bern. Working on medical image processing and advanced machine learning applied to the field of eye diseases. Experience in medical image processing, bioengineering and med-tech.*

Education

2013 -> UNIVERSITÉ DE LAUSANNE - MIAL/CHUV, Switzerland.
PhD in Life Sciences - Faculté de Biologie et Médecine. Supported by the Swiss Cancer League (grant No : KFS-2937-02-2012).

2015 / 2016 IMPERIAL COLLEGE LONDON-BIOMEDICAL IMAGE ANALYSIS GROUP (BIOMEDIA), London, UK.
Guest PhD Student - Department of Computing - Under the supervision of Prof. Daniel Rueckert. Supported by the Swiss National Science Found. (SNF) - Grant No : P1LAP3-161995.

2012 ÉCOLE POLYTECHNIQUE FÉDÉRALE DE LAUSANNE - STI IEL LTS5, Switzerland.
Master project in Neuroscience image signal processing. Image Registration in Matlab, C/C++. & GPU. Supervisor : Prof. Jean-Philippe Thiran. Qualific. EPFL - 6/6.

2004 – 2012 POLYTECHNIC UNIVERSITY OF CATALONIA - ETSETB / TELECOM BCN, Barcelona, Spain.
Electrical/Telecom. Eng. (BsC-MsC) Focus : Signal/Image Processing, Bioengineering, Patenting.

Professional Experience

Since 2013 (3y. 10 m. >) MEDICAL IMAGE ANALYSIS LAB. (MIAL-CIBM) RADIOLOGY CHUV/UNIL, Switzerland.
PhD Student & Res. Assistant (UNIL/UniBe) - Guest PhD Student EPFL.
Under the supervision of Prof. Jean-Philippe Thiran (EPFL-LTS5 / UNIL-MIAL), Dr. Meritxell Bach Cuadra (UNIL/MIAL - CIBM), Dr. Jens Kowal and Prof. Dr. Raphael Sznitman (ARTORG Center, UniBe), pursuing a PhD in *Multi-modal imaging in Ophthalmology : image processing methods for improving intra-ocular tumor treatment via MRI and Fundus image photography*, shared between UNIL , University of Bern and EPFL.

2012 (3 months) EPFL - SIGNAL PROCESSING LABORATORY 5 (LTS5) , Swiss Institute of Technology, Lausanne.
Neuroscience, Image Registration, brain imaging with C/C++ & Matlab. .

2011 - 2012 (5 months) ESTEVE TEIJIN HEALTHCARE - HOME RESPIRATORY THERAPIES, Barcelona.
Project Manager R&D.
Management and development of IT projects within the home respiratory therapies field. Collaboration in *REHABILITA* project, a spanish government promoted R&D project..

2009 - 2011 (2,5 years) PUE - PROYECTO UNIVERSIDAD EMPRESA, S.L. - IT EDUCATION, Barcelona.
IT Assistance and Administration Support.
Assistance and management of marketing and strategic organization of educational IT projects : Microsoft IT Academy Program, Linux Prof. Inst. Project, Adobe Certified Assoc. Program and Cisco Networking Academy. ▷ *IT Technological Advice.*

Complimentary Education

May - 2016 Machine Learning Summer School (MLSS) 2016 .
Machine Learning, Data Analysis and Inference, Cadiz, Spain.

Dec - 2015 Hamlyn Winter School on Surgical Imaging and Vision.
Training in technical and clinical aspects of Surgical Imaging and Vision, Imperial College London, London.

Sep - 2013 7th CIMST Summer School on Multimodal Biomedical Imaging .
Zürich Center for imaging Science and Technology - **ETH Zürich**, Zürich .

Dec - 2012 CTI Entrepreneurship Training Program of Business Concept.
Formerly known as Venture Challenge Start-Up program. **VentureLab** and **EPFL "College of Management of Technology"**, Lausanne.

Languages

Mother tongue : Spanish, Catalan.

English : **Proficient User (C1)**. FCE with Merits (2002). Half University studies received in English.

French : **Indep. user (B2)**. Course 90h.(2011)-Institut Français Barcelone. Living in Lausanne since Jan-12. Centre de Langues (EPFL) - Course 45 hours Lvl. B1 & Intensive course 40h. Lvl B1 (2012).

German : **Indep. user (B2)**. Zertif. Deutsch (2003). Centre de Langues(EPFL) Course 45 h. B1-B2 (2012).

Chinese : **Basic user (A1)**. Intensive course 40h. CEO - UPC (2008).
Merit School 60h. Lvl. A1 (2008). Vidal School of Chinese Language 90h. Lvl. A1-A2 (2009).

Computer Skills

▷ Programming : C/C++, Java, Matlab, LabView, QT, ITK, VTK, Coin3D, Python, TensorFlow, Theano, Caffe.
▷ Office Tools : MS Office, MS Project, MS Visio. Graphics : HTML + CSS, AutoCAD, Photoshop & Indesign.
▷ Others : Strong background in Windows, Windows Server, Linux, Mac OS. SVN and Git. Eclipse & Netbeans.

Extra professional Activities

Organizational :
▷ **President**, Imperial College London Innovation Forum (ICLIF) - ICL Society, London, UK.
▷ **Treasurer**, Biomedical Engineering Club (BME - Club) (2014 –>).
▷ President, IEEE Barcelona Student Branch (2007-2010) also in charge of **BURAN**, magazine of the IEEE BCN Student Branch. IEEE Member since 2007.
▷ Treasurer, IEEE Barcelona Student Branch (2011).
▷ Publicist, Student Magazine "Distorsio" at UPC (2008). Columnist and collaborator .
▷ Student Representative, at ETSETB and collaborator of DAT (2006-2011).

Sports : running, rowing & skiing. Practicing Taekwondo since 1992 (Black belt 2003). Amateur violin player. Co-creator of Taipo an anonymous, geolocalized message board.

Grants

2015 **Doc.Mobility Grant - Imperial College London** .
Multimodal patient-specific eye model for delineation and treatment planning of ocular tumors *Swiss National Science Foundation (SNF)* - 2015/2016. (Grant No : P1LAP3-161995).

2014 **450éme anniversaire** Travel Grant - Fondation pour l'Université de Lausanne .

Publications

2016 (Pend.) **C. Ciller**, S.I. De Zanet, P. Maeder, A. Pica, F.L. Munier, J-P. Thiran, R. Sznitman and M.B. Cuadra *"Topographic Fundus Mapping : Improving multimodal eye tumor analysis by fusion of MRI and Fundus Image Photography"*, - **Under Preparation**.

2016 (Pend.) **C. Ciller**, S.I. De Zanet, K. Kamnitsas, P. Maeder, B. Glocker, F.L. Munier, D. Rueckert, J-P. Thiran, M.B. Cuadra and R. Sznitman *"Multi-channel MRI segmentation of eye structures and tumors using patient-specific features"*, Plos One Journal - **Under Review**.

2016 L. Bally, T. Zueger, T. Buehler, A.S. Dokumaci, C. Speck, N. Pasi, **C. Ciller**, D. Paganini, K. Feller, H. Loher, R. Rosset, M. Wilhelm, L. Tappy, C. Boesch, C. Stettler *"Metabolic and hormonal response to intermittent high-intensity and continuous moderate intensity exercise in individuals with type 1 diabetes : a randomised crossover study"*, Diabetologia, 59(4) :776-784.

2015 L. Bally, T. Zueger, N. Pasi, **C. Ciller**, D. Paganini, C. Stettler *"Accuracy of continuous glucose monitoring during differing exercise conditions"*, Diabetes Research and Clinical Practice, 112(Feb) :1-5.

2015 **C. Ciller**, S.I. De Zanet, M. Rüegsegger, A. Pica, R. Sznitman, J.P. Thiran, P. Maeder, F. L. Munier, J. H. Kowal, M. Bach Cuadra, *"Automatic Segmentation of the Eye in 3D Magnetic Resonance Imaging : A novel Statistical Shape Model for treatment planning of Retinoblastoma"*, International Journal on Radiation Oncology*Biology*Physics, 2015 Jul 15 ; 92(4) :794-802.

2015 S. I. De Zanet, **C. Ciller**, T. Rudolph, M. Bach Cuadra, P. Maeder, A. Balmer, F.L. Munier and J.H. Kowal, *"Landmark Detection for Fusion of Fundus and MRI Toward a Patient-Specific Multimodal Eye Model"*, IEEE Transactions on Biomedical Engineering (TBME), Volume 62, Issue 2.

Conferences

2014 **C. Ciller**, S.I. De Zanet, A. Pica, J.P. Thiran, P. Maeder, F. L. Munier, J. H. Kowal, M. Bach Cuadra, *"Automatic magnetic resonance imaging segmentation of the eye based on 3D active shape modeling"*, ARVO 2014, Orlando, FLO, US, Submit. : Dec, 2013, Accept. : Feb, 2014 - **Accepted abstract & poster**.

2014 **C. Ciller**, S.I. De Zanet, A. Pica, J.P. Thiran, P. Maeder, F. L. Munier, J. H. Kowal, M. Bach Cuadra, *"Active Shape Modeling techniques in Ophthalmology : Automatic Segmentation of the eye in magnetic resonance imaging of children"*, Symposium on Statistical Shape Models and Applications, 11-13 June 2014, **Accepted Abstract & Poster** Other : 2nd Best Poster Award .